Microphysics of ice particles in the polar summer mesosphere

Henrike Wilms

Dissertation
an der Fakultät für Physik
der Ludwig–Maximilians–Universität
München

vorgelegt von
Henrike Wilms
aus Friedrichshafen

München, den 10. August 2016

Erstgutachter: Prof. Dr. Markus Rapp
Zweitgutachter: Prof. Dr. Bernhard Mayer
Tag der mündlichen Prüfung: 19. Oktober 2016

Zusammenfassung

Leuchtende Nachtwolken (NLCs) sind ein Phänomen, welches im Sommer durch Eisteilchen in der polaren Mesopause verursacht wird. Man geht davon aus, dass diese Eisteilchen durch heterogene Nukleation auf Meteorstaubteilchen (MSPs) entstehen. Mehrere mikrophysikalische Parameter, welche die Nukleationsrate bestimmen, sind jedoch unzureichend bekannt. Daher untersucht die vorliegende Arbeit, in wie fern MSPs als Nukleationskerne dienen können und wie sich Unsicherheiten in der Nukleationsrate auf die Entwicklung von NLCs auswirken.

MSPs bestehen vermutlich aus Materialien, welche im sichtbaren Spektralbereich stark absorbierend sind. Aus der Bilanz der Energiequellen und -senken folgt, dass die Gleichgewichtstemperatur T_P der MSPs höher ist als die Temperatur der umgebenden Atmosphäre T_A. Der Temperaturunterschied $\Delta T = T_\mathrm{P} - T_\mathrm{A}$ hängt dabei stark von den Absorptionseigenschaften der MSPs ab. Der größte Temperaturunterschied ΔT wird von eisenhaltigen MSPs erzielt. Um diesen Temperaturunterschied zwischen Nukleationskern und der umgebenden Atmosphäre zu berücksichtigen, wurde die klassische Nukleationstheorie erweitert. Aus dieser erweiterten Theorie wurde abgeleitet, dass MSPs zu schlechten Nukleationskernen werden, wenn sie nur wenige Kelvin wärmer sind als ihre Umgebung, da der Temperaturunterschied ΔT die Nukleationsrate um mehrere Größenordnungen reduziert.

Um allgemein zu untersuchen, welchen Einfluss eine Veränderung der Nukleationsrate auf die Entwicklung von NLCs hat, wird die Nukleationsrate in mikrophysikalischen Simulationen systematisch um mehrere Größenordnungen variiert. Die resultierenden NLC Eigenschaften werden mit NLC Eigenschaften verglichen, die aus Lidar- und Satellitenbeobachtungen abgeleitet wurden. Die beste Übereinstimmung zwischen modellierten und beobachteten NLCs wird mit Nukleationsraten erzielt, die zwei bis drei Größenordnungen kleiner sind als bisher in der Literatur angenommen.

Neuste Laborergebnisse, welche Eisnukleation auf MSPs unter mesosphärischen Bedingungen (und $T_\mathrm{P} = T_\mathrm{A}$) untersucht haben, zeigen jedoch, dass die Nukleationsrate viele Größenordnungen größer ist als bisher angenommen, der Nukleationsprozess also extrem schnell abläuft. Mit derart großen Nukleationsraten können keine realistischen NLCs simuliert werden, genauso wenig wie mit Nukleationsraten die durch den Temperaturunterschied ΔT um mehrere Größenordnungen verringert werden. Die Kombination beider Effekte kann in mikrophysikalischen Simulationen allerdings wieder zu NLC Eigenschaften führen, die vergleichbar sind mit beobachteten NLC Eigenschaften. Da die Verringerung der Nukleationsrate von ΔT abhängt und damit von der Zusammensetzung der MSPs, ergeben sich nur für eisenhaltige MSP Verbindungen wie (Magnesium-)Wüstit oder Hämatit NLCs mit realistischen Eigenschaften.

Zusammengefasst lässt sich festhalten, dass MSPs gute Nukleationskerne sind, obwohl sie wärmer sind als ihre Umgebung. Tatsächlich können mikrophysikalische Simulationen, welche die neusten Laborergebnisse berücksichtigen, nur dann realistische NLCs erzeugen, wenn auch die erhöhte MSP Gleichgewichtstemperatur berücksichtigt wird.

Abstract

Noctilucent clouds (NLCs) are a summer phenomenon caused by ice particles in the polar mesosphere. The nucleation of these ice particles is thought to occur via heterogeneous nucleation on meteoric smoke particles (MSPs). However, several factors determining the nucleation rate are poorly known. Therefore, this thesis evaluates the capability of MSPs to act as ice nuclei and the effects of uncertainties in the nucleation rate.

MSPs are likely to be composed of materials which are highly absorbing for visible light. Evaluating the energy sources and sinks of MSPs, it is found that the equilibrium temperature T_P of MSPs is higher than the temperature of the surrounding atmosphere T_A. The temperature difference $\Delta T = T_\mathrm{P} - T_\mathrm{A}$ strongly depends on the absorption efficiency of the MSP material. The largest difference ΔT is obtained for iron rich MSPs. The classical nucleation theory is extended to account for the temperature difference between the ice nucleus and the surrounding atmosphere. It is found that MSPs become poor ice nuclei when they are a few Kelvin warmer than the environment, because the temperature difference ΔT drastically reduces the nucleation rate.

In order to assess the effects of changing nucleation rates on the development of NLCs, the nucleation rate is systematically varied in microphysical simulations. The resulting NLC properties are compared to NLC properties derived from lidar and satellite observations. It is found that the modeled NLCs agree best with observed NLCs when the nucleation rate is reduced by about two to three orders of magnitude compared to the current standard assumptions.

On the contrary, recent laboratory results, which examined ice nucleation on MSP analogues under mesospheric conditions, suggest that nucleation occurs rapidly, i.e. the nucleation rate is many orders of magnitude larger than currently assumed. Thus, NLCs with realistic properties cannot be modeled if the experimentally determined parameters are included in the microphysical simulations, neither can realistic NLCs be modeled if only the temperature difference ΔT is accounted for. However, if both effects are combined in the microphysical simulations, the resulting NLCs can have properties similar to observed NLCs. Since the reduction of the nucleation rate due to the temperature difference ΔT depends on the MSP compositions, it is found that only iron rich MSP materials like (magnesio-)wuestite or hematite lead to NLCs with realistic properties.

In conclusion, it is found that even though MSPs are warmer than the surrounding atmosphere, they are nevertheless good ice nuclei. Indeed, microphysical simulations which take into account the recent laboratory results, only yield realistic NLCs if the increased MSP equilibrium temperature is implemented as well.

Publications

Parts of the results presented in this thesis have been published in the following two articles:

- Asmus, H., H. Wilms, B. Strelnikov, and M. Rapp (2014), On the heterogeneous nucleation of mesospheric ice on meteoric smoke particles: Microphysical modeling, *J. Atmos. Sol. Terr. Phy., 118*, 180–189, doi: 10.1016/j.jastp.2014.03.009.

  H. Asmus performed the calculations of the equilibrium temperature and wrote the first draft of the paper. H. Wilms extended the nucleation theory to account for a temperature differences between ice nuclei and ambient atmosphere, implemented the new nucleation theory and an algorithm for calculating the equilibrium temperature into the microphysical model. B. Strelnikov and M. Rapp supervised and guided the calculations and simulations.

- Wilms, H., M. Rapp, and A. Kirsch (2016), Nucleation of mesospheric cloud particles: Sensitivities and limits, *J. Geophys. Res., 121*, doi:10.1002/2015JA021764.

  H. Wilms designed and performed the simulation, analysed and interpreted the data and wrote the paper. M. Rapp guided the analysis and interpretation. A. Kirsch integrated the dynamical background fields into the microphysical model.

Contents

1 Introduction

The polar summer mesosphere is a unique and fascinating region of the Earth's atmosphere. This region exhibits a variety of geophysical phenomena, which are related to the extreme thermal conditions of this region. The polar summer mesopause at ∼87 km altitude is characterized by mean temperatures as low as 130 K (Lübken, 1999), which makes it the coldest region of the whole atmosphere. Even though there is very little water vapor available in this altitude region (only a few ppm), the extremely low temperatures lead to highly supersaturated conditions which allow for the existence of ice particles. These ice particles can be visible as silvery clouds against the twilight sky, which gave rise to the name noctilucent clouds. Besides being a stunning optical phenomenon, these clouds are of scientific interest as they offer the possibility to study the otherwise difficult accessible mesopause region.

1.1 Noctilucent Clouds

The first reported sightings of noctilucent clouds (NLCs) date back to 1885 (Leslie, 1885; Jesse, 1885; Backhouse, 1885). It was soon realized that these clouds were no normal tropospheric clouds since they occurred at an altitude of 82 km (Jesse, 1896), which is ∼70 km above the clouds involved in our daily weather. Due to the high altitude of NLCs, the sunlight scattered by these ice particles can reach the night side of the Earth. Only there and then they are visible against the darker twilight sky, as during daylight they are optically too thin to be seen. The NLC season typically lasts from about 5 weeks before solstice to 7 weeks afterwards, with ideal viewing locations between 53° to 57° N/S (Thomas, 1991). The photograph in Fig. 1.1 shows a typical NLC when looking northwards during twilight. This photograph was taken during one of the rare occasions when NLCs were visible as far south as Munich (48°8′ N). The wave-like patterns of the NLC are typical; they are caused by passing or breaking gravity waves which lead to a modulation of NLC brightness (e.g. Witt, 1968). Although the term NLC originally refers to the twilight phenomenon, mesospheric clouds in general will be named NLCs in the following, independent of the observation technique and time.

NLCs are primarily composed of water ice (Hervig et al., 2001) and contain small fractions of meteoric smoke particles (Hervig et al., 2012). The exact ice phase is still ambiguous, with cubic ice, amorphous ice and stacked-disordered ice being

Figure 1.1: Photograph of NLCs seen from Munich on July 4, 2014 at 3:40 LT (taken from `http://www.foto-webcam.eu/webcam/freimann/#/2014/07/04/0340`).

possible candidates (Hervig and Gordley, 2010; Murray et al., 2015). In the currently accepted picture of NLC formation (Rapp and Thomas, 2006), the general life cycle of mesopheric ice particles proceeds as follows (see Fig. 1.2): Nucleation takes place at the cold mesopause where the saturation is highest. While being transported to lower altitudes (either by sedimentation, diffusion or vertical wind) the newly nucleated ice particles grow by deposition of water vapor on their surface and eventually become optically detectable. The maximum NLC brightness is reached at about 82 km altitude, just at the lower boundary of the supersaturated altitude range. Further downward progression of the ice particles leads to their rapid evaporation.

While there is broad consensus on this general picture, the detailed processes are still unclear. The microphysical process which is least quantified is the initial ice formation, i.e. the nucleation of mesospheric ice particles (Thomas, 1991; Rapp and Thomas, 2006). Several different nucleation pathways have been proposed, among these are heterogeneous nucleation (e.g., Turco et al., 1982), homogeneous nucleation (e.g., Murray and Jensen, 2010), nucleation on ionic water clusters $H^+(H_2O)_n$ (Witt, 1969), as well as nucleation on strongly bipolar molecules such as $NaHCO_3$ (Plane, 2000).

In the case of heterogeneous nucleation, ice particles form on preexisting ice nuclei, which lower the energy barrier associated with the phase change from water vapor to ice (Pruppacher and Klett, 1997). The most likely candidate for meospheric ice nuclei are meteoric smoke particles (MSPs), which are thought to form from the material of ablated meteoroids (Hunten et al., 1980). An alternative nucleation pathway involves ions (e.g., ionic water clusters) or charged MSPs (Gumbel and Megner, 2009; Megner and Gumbel, 2009). Ion-induced nucleation can be very efficient because Coulomb interaction also lowers the nucleation barrier or even removes it completely. However,

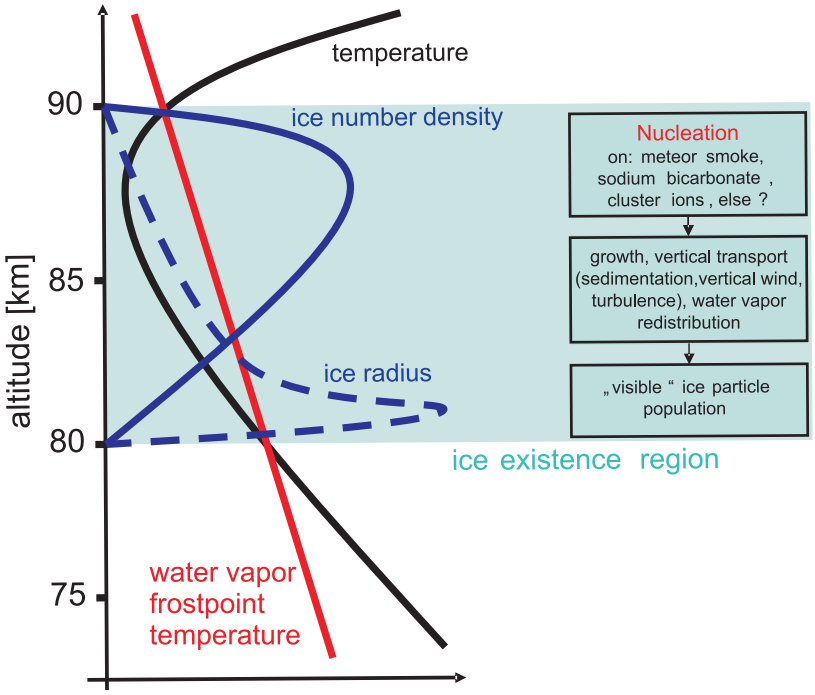

Figure 1.2: Schematic of the main processes involved in the formation and evolution of NLCs (modified from Rapp and Thomas, 2006).

the modeling results by Turco et al. (1982) indicate, that if MSPs and ions are both present, heterogeneous nucleation on the MSPs will be more likely, because it is less restrictive in terms of supersaturation. Ion-induced nucleation may become feasible under extreme atmospheric conditions when ice particles are already present, but is generally of limited importance because of dissociative recombination of the ion clusters with ambient electrons (Gumbel and Witt, 2002; Gumbel et al., 2003). Nucleation can in principle also occur without preexisting ice nuclei or ions, which is then called homogeneous nucleation. Homogeneous nucleation generally requires more extreme conditions compared to heterogeneous nucleation, i.e., lower temperatures ($<$110 K) and higher saturation ratios, which makes homogeneous nucleation unlikely (Murray and Jensen, 2010).

From these possible nucleation pathways, heterogeneous nucleation on MSPs is considered to be the most likely one (Rapp and Thomas, 2006). However, even if heterogeneous nucleation seems to be the most likely nucleation mechanism, the exact details of this nucleation mechanism are unknown, e.g. the exact composition and crystalline structure of MSPs has not yet been quantified. Furthermore, the parameters that determine the nucleation rate itself are poorly known, because laboratory measurements under mesospheric conditions are rare.

The scientific interest in NLCs is motivated by their capability to act as a visual proxy

for physical processes in the summer mesopause region. Since the conditions at the polar summer mesopause only marginally allow for the existence of ice particles, NLCs are considered to be a very sensitive indicator of long-term trends and changes in that altitude region. In particular, the effects of anthropogenic climate change are expected to be amplified by the non-linearity of NLC microphysics. Thomas et al. (1989) showed that an increase of methane, which is partly oxidized to water in the stratosphere, leads to an increase of mesospheric water vapor. As a result, NLC brightness and occurrence is expected to increase in a changing climate. Additionally, the increase of atmospheric CO_2 leads to a cooling at mesospheric heights (Roble and Dickinson, 1989), which is also expected to enhance NLC brightness and occurrence. It was therefore proposed that NLCs are the 'miner's canary' for climate change (Thomas, 1996). Whether or not NLCs truly show this predicted trend has been controversially debated (von Zahn, 2003; Thomas et al., 2003), not least because mesospheric water vapor is additionally modulated by the solar cycle (Hervig and Siskind, 2006) and by space shuttle exhaust (Stevens et al., 2003, 2005, 2012). The latest analysis of a 36 year NLC data set by Hervig et al. (2016) shows that the variability of the mesospheric ice water content is in equal parts related to variability of the solar Ly-α flux (by H_2O-photolysis) and variations of the stratospheric temperature. A cooling of the stratosphere leads to a shrinking and cooling of the atmosphere above (Lübken et al., 2009; Lübken and Berger, 2011; Lübken et al., 2013). Since stratospheric cooling is partly caused by increasing greenhouse gases, this mechanism provides an indirect link between increasing greenhouse gases and NLC brightness. However, results from chemistry climate models show that directly at the mesopause, i.e. the altitude region of NLC formation, the temperature trend is not significant (Garcia et al., 2007; Schmidt et al., 2006).

Besides long-term trends, also dynamical properties of the mesopause are commonly inferred from NLC measurements. For example, NLCs have been used to determine wave parameters and wind velocities from ground based photographs (e.g., Witt, 1962; Pautet et al., 2011; Demissie et al., 2014) and from lidar observations (e.g., Kaifler et al., 2013a) as well as from satellite observations (e.g., Chandran et al., 2009; Rong et al., 2015). Furthermore, Kelvin-Helmholtz instabilities have been identified to cause small scale structures in NLCs (Baumgarten and Fritts, 2014). The underlying assumption for all these studies is that NLCs can be treated as a passive tracer over the relevant time scales. So far, it is inconclusive under which conditions and on which time scales NLCs can be considered as passive tracers. Baumgarten et al. (2012) reported coincident lidar and satellite measurements and found that NLCs can be treated as a passive tracer for time scales of about 1 h and less. Chandran et al. (2012) found significant changes in NLC albedo between subsequent satellite overpasses which were 1.5 h apart. These changes in NLC albedo are possibly related to ice particles growing from subvisible to visible sizes (Chandran et al., 2012), indicating that NLCs cannot be considered as a passive tracer for these longer time scales.

Regardless of whether NLCs are used as an indicator of mesospheric temperature and water vapor trends or whether NLCs are used as tracer for mesospheric dynamics, it is crucial to have a rigorous understanding of the NLC formation process. Only if it is completely understood how NLCs react to changes in temperature or water vapor, the correct conclusions concerning those changes can be drawn from observed NLC properties. One major unknown in the ice microphysics is the initial ice formation process, the nucleation of mesospheric ice particles, which is assumed to occur on meteoric smoke particles.

1.2 Meteoric Smoke Particles

Meteoroids entering the Earth's atmosphere undergo rapid heating due to collisions with air molecules until they melt and vaporize (Ceplecha et al., 1998). This gives rise to global metal layers in the mesosphere, such as the Fe-layer (Clemesha et al., 1978) or the Na-layer (Slipher, 1929). These metal atoms form compounds which polymerize to meteoric smoke particles (Rosinski and Snow, 1961; Hunten et al., 1980; Plane et al., 2015). Based on laboratory experiments, Saunders and Plane (2006) concluded that MSPs are likely to consist of iron containing minerals such as hematite (Fe_2O_3), fayalite (Fe_2SiO_4) and goethite (FeOOH) together with silica.

MSPs have been detected by rocket experiments (Gelinas et al., 1998; Schulte and Arnold, 1992; Lynch et al., 2005; Rapp et al., 2005, 2010; Robertson et al., 2014), radar observations (Strelnikova et al., 2007) and satellite observations (Hervig et al., 2009a). Despite the experimental evidence of the existence of MSPs, the exact MSP number density and size distribution is still unknown and relies on MSP models (Hunten et al., 1980; Megner et al., 2008b; Bardeen et al., 2008).

In a recent analysis of satellite observations, meteoric smoke particles were identified within mesospheric ice particles (Hervig et al., 2012). The satellite extinction measurements are best compatible with the extinction of ice-MSP-mixtures, which include various volume fractions of (magnesio-)wuestite, hematite or carbon. This is a strong indication that MSPs are indeed involved in mesospheric ice microphysics. However, it is yet to be demonstrated whether the MSPs act as nucleation sites or whether they are collected by the growing ice particles after nucleation.

MSPs are considered to be the major candidate for mesospheric ice nuclei, and furthermore, MSPs are also considered to be very efficient ice nuclei. This is based on their crystalline structure, which is similar to the crystalline structure of cubic ice (Roddy, 1984). So far it has been assumed that MSPs have the same temperature as the ambient air. However, since MSPs are probably composed of materials which are highly absorbing at visible wavelengths, they might be warmer than the ambient atmosphere. It has been shown that even ice particles, which are almost transparent

in the visible wavelength range, acquire an equilibrium temperature slightly warmer than the ambient atmosphere (Espy and Jutt, 2002). It is therefore reasonable to expect MSPs to acquire even higher equilibrium temperatures, with so far unexplored implications for ice microphysics.

While the polar summer mesopause is highly supersaturated with respect to the local atmospheric temperature, it might not be supersaturated with respect to warmer MSPs. The saturation ratio 'seen' by these warmer MSPs would therefore be lower. Since nucleation relies on supersaturated conditions, warmer MSPs potentially impede nucleation. Thus, taking into account their possibly increased equilibrium temperature, the current assumption that MSPs are good and efficient ice nuclei has to be reconsidered.

1.3 Hypothesis

Based on the assumption that MSPs are composed of iron-rich materials, which effectively absorb solar radiation, the following hypothesis is formulated:

> MSPs acquire a higher equilibrium temperature compared to the ambient atmosphere, which inhibits efficient nucleation. MSPs should therefore be poor ice nuclei.

In order to assess this hypothesis, the following questions have to be answered.

Q1 What is the equilibrium temperature of meteoric smoke particles?

Q2 How is the nucleation rate affected by possibly warmer ice nuclei?

Q3 Does the nucleation rate have an influence on the observable NLC properties? Can the nucleation rate be constrained by comparing modeled NLC properties with observations?

Q4 Are these results consistent with laboratory experiments examining ice nucleation on MSPs?

The answers to these questions will be given in the following chapters, which are structured as follows.

Chapter 2 gives a detailed overview over classical nucleation theory, on which our current understanding of mesospheric ice nucleation is based. The underlying assumptions and limitations are reviewed as well as the uncertainty of the relevant parameters. Additionally, an extension to the classical nucleation theory is derived, that explicitly

accounts for a temperature difference between ice nucleus and ambient atmosphere. **(Q2)**

Chapter 3 describes the microphysical model used for the NLC simulations, including the model setup and the background profiles.

In **Chapter 4** the equilibrium temperature of MSPs is calculated, in dependence of MSP composition, size and altitude. First implications for heterogeneous ice nucleation are discussed. **(Q1)**

Chapter 5 assesses the importance of the nucleation rate for the properties of NLCs. NLCs are modeled with different nucleation rates and characteristic properties are compared to lidar and satellite observations. This comparison allows for the constraint of the nucleation rate to a range where modeled NLC best match the observations. Furthermore, the importance of mesospheric dynamics for the formation of NLCs is analyzed. **(Q3)**

In **Chapter 6**, the results gained from the previous chapters are combined with recent laboratory results obtained at the Karlsruhe Institute of Technology (KIT). By analyzing simulations which were performed with different MSP compositions, the MSP compositions yielding best agreement between modeled and observed NLCs are identified. **(Q4)**

Chapter 7 summarizes the results and evaluates the formulated hypothesis.

2 Microphysics

2.1 Classical nucleation theory

Phase transitions, especially phase transitions of water, are commonly observed in daily life. Melting of ice cubes, fogging of glasses or formation of frost on leaves are a few examples which reflect the ability of water to change its physical state. The temperature and pressure range in which the different phases are stable can be summarized in a phase diagram, as shown in Fig. 2.1 for water. The three phases are separated by the lines of equilibrium. For conditions exactly on those curves the adjacent phases can coexist.

Changing the conditions in a way that the system traverses an equilibrium line does not necessarily lead to an instantaneous phase transition. For example, it is possible to cool water vapor to the regime where solid ice is the stable phase. Water vapor is then metastable under these conditions. This supercooling is possible because the formation of the solid phase requires a process called nucleation, which does not occur instantaneously when traversing the equilibrium line. Nucleation occurs via small clusters which form in the vapor due to thermal fluctuations. The vapor phase is under these conditions metastable with respect to the bulk phase, but can be stable with respect to small clusters. This is the case for typical conditions of the polar summer mesopause, as indicated by the red dot in Fig. 2.1.

The formation of those clusters, also called germs, and how they lead to a phase transition is subject to nucleation theory. The following section will give an explanation on the involved thermodynamics and derive the nucleation rate based on classical nucleation theory. The derivation is independent of the considered gas, but as the nucleation of water vapor is of primary interest for this thesis, variable names and specific examples are chosen with respect to water vapor and mesopause conditions.

2.1.1 Equilibrium condition of phase interface

In order to understand the development of nucleation germs, it is necessary to consider equilibrium conditions first. To simplify the derivation of the thermodynamic properties, the interaction of only two pure phases, a solid and a vapor phase, is

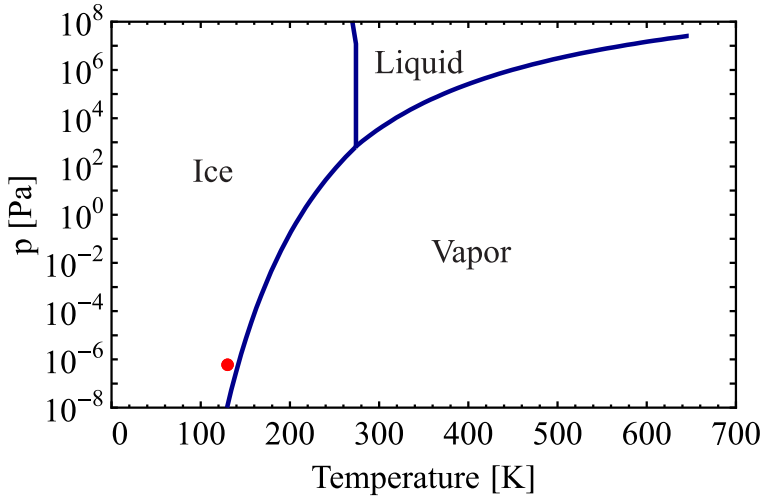

Figure 2.1: Phase diagram of water. The conditions typically found at the polar summer mesopause are indicated by the red dot. The data was taken from the National Institute of Standards and Technology (`http://webbook.nist.gov/`).

considered. Equilibrium conditions imply that the two phases coexist, i.e. there is no net transformation of molecules from one phase to another. For a given temperature T, equilibrium will emerge for the pressure $p_{\mathrm{sat}}(T)$ given by the lines of equilibrium in the phase diagram. This pressure is called the saturation vapor pressure and attains the same value in both phases if they are separated by a flat interface.

The saturation vapor pressure is determined by the energy it takes for molecules to escape the solid phase. The lower the energy is which they need to leave the solid phase, the higher is p_{sat}. The saturation vapor pressure is strongly temperature dependent, as shown in Fig. 2.2(a) for water vapor: At higher temperatures the molecules have a higher thermal energy, so that bonds to their neighboring molecules can be broken up more easily. This allows more molecules to escape to the vapor phase. Another example where this becomes specifically important is when the surface of the solid phase is curved such as during the formation of clusters or ice particles. The outermost molecules will have fewer binding partners compared to a flat surface, so that less energy is needed for these molecules to leave the condensed phase. Thus, the saturation vapor pressure over a convex surface is higher than the saturation vapor pressure over a flat surface (and lower over a concave surface). This is called the Kelvin Effect and is given by (Pruppacher and Klett, 1997)

$$p_{\mathrm{sat}}(T,R) = p_{\mathrm{sat}}(T,\infty)\exp\left(\frac{2\sigma m_{\mathrm{w}}}{\rho_{\mathrm{ice}} k_{\mathrm{b}} T R}\right). \tag{2.1}$$

The surface tension is denoted by σ, the mass of one water molecule by m_{w}, the ice

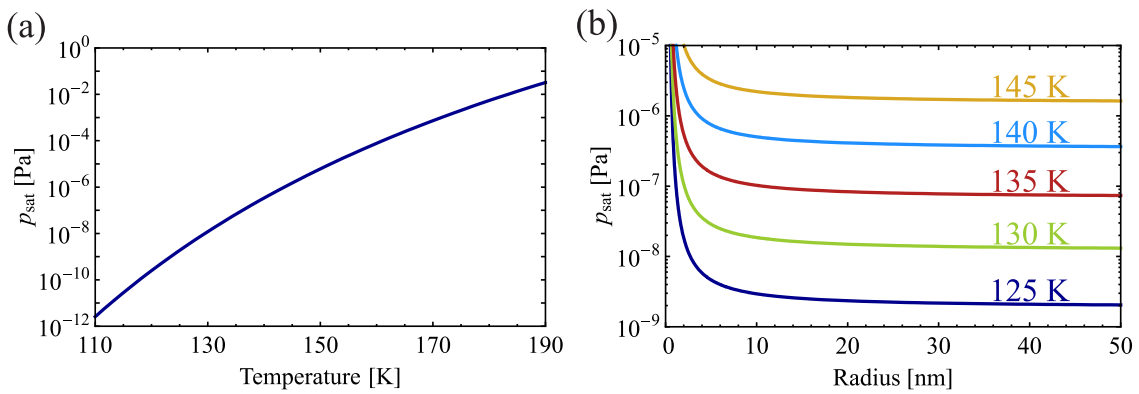

Figure 2.2: (a) Saturation vapor pressure over ice as a function of temperature. (b) Demonstration of the radius dependence of p_{sat} (Kelvin effect).

density by ρ_{ice}, the radius of curvature by R, and the Boltzmann constant by k_{b}. The Kelvin effect has a significant influence on the saturation vapor pressure if the particles are very small. As demonstrated in Fig. 2.2(b), particles with radii smaller than 10 nm are notably affected by the Kelvin effect.

The saturation ratio is defined as the ratio of current water vapor partial pressure $p_{\mathrm{H_2O}}$ to saturation vapor pressure over a flat surface

$$S = \frac{p_{\mathrm{H_2O}}}{p_{\mathrm{sat}}(T, \infty)}. \tag{2.2}$$

For every supersaturation there exist one particular radius r^* which is in equilibrium with the vapor phase, i.e. $S(T, R = r^*) = 1$. This is the so called critical radius r^* and follows from Eq. 2.1

$$\begin{aligned} \frac{p_{\mathrm{H_2O}}}{p_{\mathrm{sat}}(T, \infty) \exp\left(\frac{2\sigma m_{\mathrm{w}}}{\rho_{\mathrm{ice}} k_{\mathrm{b}} T r^*}\right)} &= 1 \\ r^* &= \frac{2\sigma m_{\mathrm{w}}}{\rho_{\mathrm{ice}} k_{\mathrm{b}} T \ln S} \end{aligned} \tag{2.3}$$

For all clusters larger than r^* the vapor is supersaturated, for all clusters smaller than r^* the vapor is sub-saturated.

2.1.2 Vapor fluxes

For the following description of the growth of clusters, it is necessary to know the flux of molecules through an arbitrarily orientated surface $w^{\downarrow}$. This flux is determined

by the molecular number density of the gas phase $n_{H_2O} = p_{H_2O}/k_b T_A$ and the mean thermal velocity $v_{therm} = \sqrt{\frac{8 k_b T_A}{\pi m_w}}$ via (Pruppacher and Klett, 1997)

$$w^{\downarrow} = \frac{n_{H_2O} v_{therm}}{4} = \frac{p_{H_2O}}{\sqrt{2\pi m_w k_b T_A}}. \tag{2.4}$$

If the system is in equilibrium, the flux towards the ice phase must be compensated by an evaporation flux which leaves the ice phase. Since in equilibrium the vapor pressure p_{H_2O} is equal to p_{sat}, this flux is given by

$$w^{\uparrow} = \frac{p_{sat}(T_P, R)}{\sqrt{2\pi m_w k_b T_P}}. \tag{2.5}$$

The two temperatures T_A and T_P refer to the temperature of the gas phase and ice phase, which are equal in thermodynamic equilibrium. However, differences between T_A and T_P will be important in Sec. 2.1.4 for describing heterogeneous nucleation on MSPs. It is assumed that the outgoing flux $w^{\uparrow}$ is solely dependent on the properties of the ice phase. This means that even under changed conditions of the surrounding gas, the outgoing flux is determined by the saturation vapor pressure.

2.1.3 Homogeneous nucleation

Considering only equilibrium conditions cannot explain the formation of a new phase. Based on the radius dependence of p_{sat} (see Fig. 2.2b) the vapor pressure which would be needed to hold a nm-sized cluster of water molecules in equilibrium would be extremely large. However, such large vapor pressures are not necessary since a phase transformation is not a continuous process in the beginning, but rather a spontaneous one. The new phase forms from thermal fluctuations in the metastable parent phase, which eventually leads to a macroscopic phase change.

Energy of cluster formation

Starting point for a phase transition is a metastable system, e.g. water vapor which is supersaturated with respect to ice. Small clusters form within the vapor by statistical agglomeration, which are called embryos or i-mers (clusters consisting of i molecules). The Helmholtz free energy ΔF_i which is needed to form a cluster containing i molecules is given by (Pruppacher and Klett, 1997)

$$\Delta F_i = A_i \sigma - i\, k_b T \ln S \tag{2.6}$$

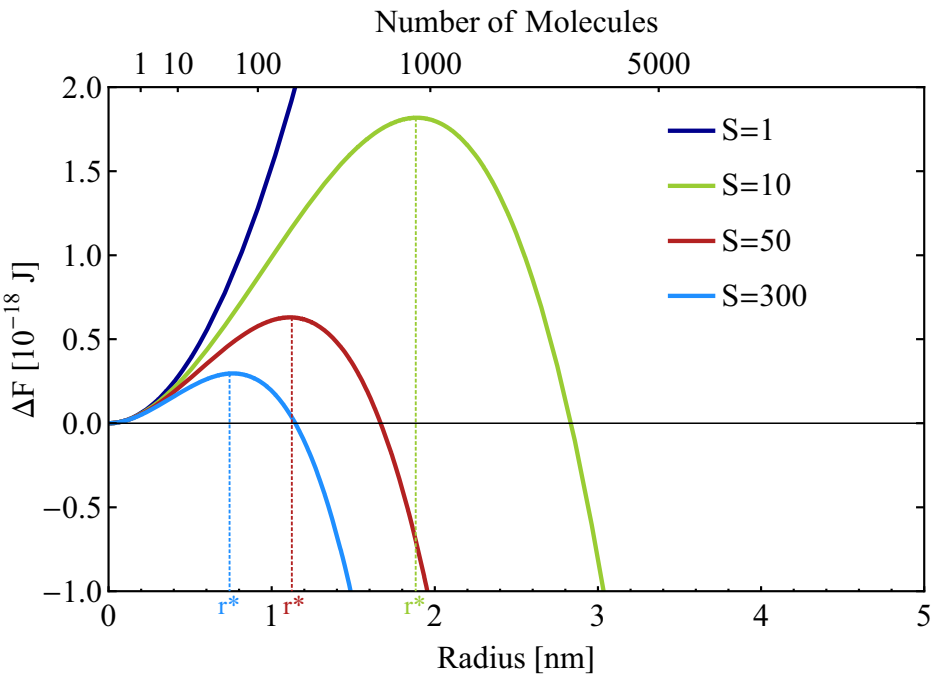

Figure 2.3: ΔF as a function of germ radius for typical summer mesopause conditions and different saturation ratios S. The corresponding number of molecules is indicated by the upper axis. Vertical lines denote the critical radius.

with $A_i = i^{2/3}(24\pi v^2)^{1/3}$ the surface area of the i-mer and v the volume of a molecule. Expressing ΔF_i as a function of cluster radius R yields

$$\Delta F(R) = 4\pi R^2 \sigma - \frac{4\pi \rho_{\text{ice}} R^3}{3 m_{\text{w}}} k_b T \ln S \tag{2.7}$$

and is shown in Figure 2.3 for ice cluster formation at $T = 130\,\text{K}$ and different saturation ratios S.

The first term in ΔF describes the energy which is needed to create the interface between the two phases. It scales with the surface area of the new cluster, i.e. with R^2 and is always positive. The second term quantifies the bulk energy which is released upon phase transition. This volume term scales with R^3 and is proportional to $\ln S$, which means it can be either positive (supersaturation) or negative (sub-saturation). At small radii the positive contribution from the surface energy term dominates, whereas at larger radii (and $S > 1$) the required surface energy is compensated by the bulk energy release. Therefore, for all values of $S > 1$ the function of ΔF exhibits a distinct maximum. The corresponding radius is called the critical radius r^*, which is found by solving $\partial \Delta F / \partial R = 0$:

$$r^* = \frac{2\sigma m_\mathrm{w}}{\rho_\mathrm{ice} k_\mathrm{b} T \ln S}. \tag{2.8}$$

The critical radius found here by differentiating ΔF is the same as the one obtained from the Kelvin law (see Eq. 2.3). The value of ΔF at r^*

$$\Delta F^* = \frac{16\pi\sigma^3 m_\mathrm{w}^2}{3(\rho_\mathrm{ice} k_b T \ln S)^2} = \frac{4\pi r^{*2}\sigma}{3} \tag{2.9}$$

acts as a barrier for nucleation. This is the amount of energy which must be supplied by thermal fluctuations in the supersaturated vapor in order for nucleation to occur. Once a cluster has reached the critical size, it will on average continue growing. The reason is that further growth is associated with release of energy ($\Delta F < 0$) in the form of latent heat and is therefore energetically favored.

Several traditional texts use the Gibbs energy ΔG instead of ΔF for describing the energy of cluster formation. Whereas ΔF is a function of the natural variables V, T and N, the natural variables of ΔG are p, T and N. As indicated by the Young-Laplace equation ($p_\mathrm{ice} - p_\mathrm{vapor} = \frac{2\sigma}{R}$), the pressure inside a cluster p_ice is strongly enhanced relative to the vapor pressure p_vapor. Thus, a phase transformation is not a constant pressure process. Instead, the volume of the complete system can be assumed to remain constant. For this reason the appropriate thermodynamic potential is $\Delta F(V, T, N)$ (see Abraham (1968) for detailed discussion). Landau and Lifshitz (1969, §142) state that it would be even more convenient to consider the grand potential (grand canonical ensemble) $\Omega = F - \mu N = \Omega(V, T, \mu)$ since T and μ are equal in both phases, whereas the pressure is generally not equal when surface effects are taken into account. This approach has been followed by Abraham and Pound (1968) for evaluating fluctuations in the vapor phase. More generally speaking, the Gibbs energy G is the appropriate thermodynamic potential if the system seeks only thermodynamic equilibrium, F is more appropriate if the system seeks thermodynamic and mechanical equilibrium.

It is assumed that i-mers (clusters of i molecules) grow by capture of single molecules (monomers) or dissociate by release of monomers. As capture and dissociation rates are assumed equal, a quasi-equilibrium (association-dissociation equilibrium) develops with an i-mer number density c_i according to the Boltzmann distribution

$$c_i = c_1 \exp\left(-\frac{\Delta F_i}{k_b T}\right). \tag{2.10}$$

The monomer concentration c_1 is directly inferred from the ideal gas law with

$$c_1 = p_{\mathrm{H_2O}}/k_b T, \tag{2.11}$$

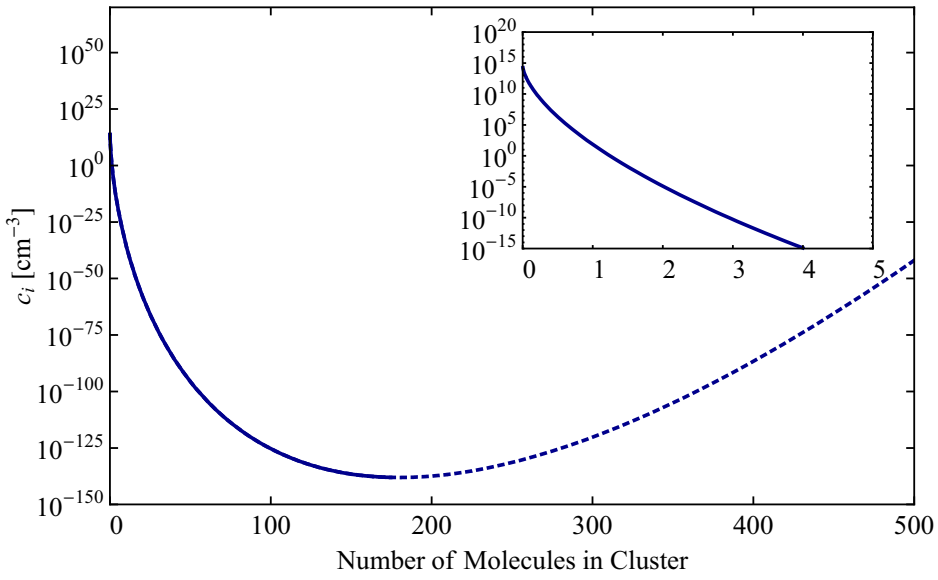

Figure 2.4: Cluster density c_i as a function cluster size (see Eq. 2.10) for typical summer mesopause conditions. The inlet shows a zoom of the function for small clusters.

neglecting that a certain number of monomers is bound in dimers, trimers, etc. This is justifiable since only an insignificant number of monomers is actually bound, as demonstrated in Figure 2.4. This figure shows c_i for typical summer mesopause conditions (130 K, water vapor mixing ratio of 2 ppm, background pressure of 0.3 Pa corresponding to 87 km, saturation ratio $S = 50$). As already argued by Byers (1965), the i-mer concentration for clusters larger than the critical radius is non-physical and therefore marked by a dashed line. One reason is that the total number of molecules in the whole system must be limited, which would not be the case if c_i continued to increase as suggested by Eq. 2.10. Also note that inconsistencies are found in c_i for low values of i: when $i = 1$, c_i should be identical to the pre-exponential factor c_1 obtained from the ideal gas law. This would require ΔF_1 to vanish, which is not given by Eq. 2.9. This aspect will be revisited in the framework of the self-consistent correction of ΔF.

In the following, the number density of critical clusters, c^*,

$$c^* = c_1 \exp\left(-\frac{\Delta F^*}{k_b T}\right) \tag{2.12}$$

will be an important quantity to determine the nucleation rate.

Homogeneous Nucleation Rate

The nucleation rate J is the rate at which critical cluster become supercritical, given in the units of germs per unit volume and unit time. This rate can be formulated as the rate at which a critical cluster is joined by an additional monomer: $J = c^*\Phi$, where Φ is the flux of monomers to the critical cluster.

This simple approach is insufficient for the following reason: Since the critical clusters are constantly removed from the size distribution, the size distribution can in general not be the equilibrium distribution given by Eq. 2.10, as no mass flux up the size spectrum is considered. Therefore, the kinetics of i-mer formation (and dissociation) need to be accounted for. The classic paper by Becker and Döring (1935) introduced a detailed balance of growth and evaporation of all intermediate i-mer states. Interestingly, the intermediate states must not be known in order to find J. They find that cluster formation can be described in analogy to electrical current flowing through a series of resistors. The electrical current thereby corresponds to clusters passing through different size ranges, which leads to a steady state cluster size distribution. In the end, they find a nucleation rate given by[1]

$$J = Zc^*\Phi \tag{2.13}$$

which differs from the simple approach given above only by Z, the so-called Zeldovich factor

$$Z = \sqrt{\frac{\Delta F^*}{3\pi k_b T n^{*2}}}. \tag{2.14}$$

The Zeldovich factor is a measure of the deviation of the steady state size distribution from the equilibrium distribution given by Eq. 2.10.

The flux of monomers to the cluster, Φ, can be expressed via the surface area $A = 4\pi r^{*2}$ times the molecular flux $w^{\downarrow}$ (see Eq. 2.4).

Combining Eqs. 2.13, 2.14, 2.12, 2.9, 2.11, and 2.4 yields the homogeneous nucleation rate in the framework of classical nucleation theory

$$J_{\mathrm{hom,CNT}} = \sqrt{\frac{2\sigma}{\pi m_{\mathrm{w}}}} v_{\mathrm{ice}} \left(\frac{p_{\mathrm{H_2O}}}{k_b T}\right)^2 \exp\left(-\frac{\Delta F^*}{k_b T}\right) \tag{2.15}$$

[1] A similar ansatz will be used in Sec 2.1.4 with slight modifications that account for temperature differences between vapor and nucleus. Therefore, this result is presented here without complete derivation, as its derivation is found in the literature (e.g., Pruppacher and Klett, 1997; Becker and Döring, 1935; Girshick and Chiu, 1990)

Extension and limitations

Improvements to the classical nucleation theory have been proposed by various authors. One of the problems of the classical nucleation theory, which is solved by the 'kinetic theory', is a conceptual problem: Although the system is in metastable equilibrium and nucleation produces supercritical clusters, a steady state distribution of clusters is assumed throughout the nucleation process. In order to keep up the continuous nucleation process, all clusters larger than a certain size would have to be dissociated to replenish the consumed monomers — this is usually assumed to be done by 'Maxwell demons'. Katz and Wiedersich (1977) and Katz and Donohue (1979) were the first to propose an alternative approach, which does not require such an 'hypothetical' steady state distribution. They find that the cluster size distribution in Eq. 2.10 is not determined by the monomer number density c_1 at supersaturation but rather by the monomer number density c_{sat} at equilibrium, i.e. saturation. Since $c_{\mathrm{sat}} = c_1/S$, the nucleation rate has to be corrected by a factor of $1/S$ (Girshick and Chiu, 1990). In order to be self-consistent (Blander and Katz, 1972), Girshick and Chiu (1990) reformulated the energy for cluster formation to $\Delta F_{i,SC} = \Delta F_i - \Delta F_1(S = 1)$ by subtracting ΔF of a monomer. The nucleation rate is therefore corrected by a factor of $\exp(\Delta F_1/k_bT)$. Combining the self-consistent and kinetic theory yields (Girshick and Chiu, 1990)

$$J_{\mathrm{hom}} = \frac{\exp\Theta}{S} J_{\mathrm{hom,CNT}} \tag{2.16}$$

with

$$\Theta = \frac{\Delta F_1(S=1)}{k_bT} = \frac{(36v\pi)^{1/3}\sigma}{k_bT}. \tag{2.17}$$

The nucleation rate, as expressed above by the classical approach, relies on several assumptions. The capillarity approximation — the fundamental assumption of classical nucleation theory — treats a cluster as a macroscopic object with the characteristics of the bulk material. The physical concepts are applied to systems containing only a few tens to hundred molecules. In this size regime, the explicit interaction of molecules is likely to become important as well as the contribution of rotational and translational energy to the total free energy of the cluster. Lothe and Pound (1962) pointed out that the classical term of ΔF only considers internal energy contributions, however no contributions from the center of mass movement of the clusters. Therefore, they included rotational and translational contributions to ΔF. The nucleation rate which they derived increased by 17 orders of magnitude for the conditions they evaluated. This aspect has been controversially discussed by Reiss and Katz (1967), Lothe (1968), and Reiss et al. (1968) with the main point of disagreement being whether the free

energy (as in Eq. 2.6) includes the free motion of the particle or not. Similar criticism came by Ford (1997) who claimed that contributions from positional entropy to ΔF are necessary in order for the nucleation rate to fulfill the nucleation theorem (Kashchiev, 1982; Bowles et al., 2001). Lee et al. (1973) concluded from model calculations that a good estimate of the total free energy can only be obtained if contributions from free translation and rotation (and other terms) are added to the total free energy. Finally, Reguera and Rubí (2001) find from kinetic considerations that the term $4k_bT \ln i$ must be added to ΔF for a cluster in motion. Rotational and translational motions of clusters are clearly seen in molecular dynamics simulations, as noted by Kashchiev (2006).

Independent of the question which terms contribute to the total free energy, the capillary approximation assumes that the concept of surface tension can be applied to clusters in the size of nanometers. In particular, no radius dependence of the surface tension is incorporated into the nucleation theory. Tolman (1949) deduced a relationship between the radius of curvature of the surface and the surface tension, where σ decreases for decreasing radii. A decrease in σ would lead to a smaller critical radius and thus to a lower energy barrier, facilitating homogeneous nucleation. However, Koga et al. (1998) concluded for vapor to liquid nucleation, that Tolman's equation is only valid for systems which hold more than 10^6 molecules or for clusters with radii larger than 20 molecular diameters. As this is not the case (see also Figure 2.4), it remains inconclusive which radius dependence of the surface tension is appropriate.

As summarized by Kashchiev (2003), the original work of Gibbs (1906) introduced the concept of a dividing surface between the parent phase and the newly formed phase, which allows the exact formulation of the energy barrier ΔF^*. Gibbs (1906) found that the only unknown quantity describing this energy barrier is the surface tension σ_T of a specific dividing surface (the so-called surface of tension, the dividing surface with minimum surface tension, Kalikmanov 2013). However, this dividing surface is only an imaginary surface which does not describe the physical boundary of the cluster. Thus, this surface tension σ_T and its dependence on temperature and pressure cannot be determined experimentally. By replacing σ_T with the surface tension σ of the interface between parent phase and nucleus at equilibrium, the exact value of ΔF^* by Gibbs (1906) is replaced by an approximation thereof. Based on the concept of the dividing surface, Kashchiev (2003) developed a thermodynamically consistent description of the energy barrier, by choosing the dividing surface in such a way that it always attains the surface energy σ of the actual phase interface.

Although the self-consistent extension (subtracting ΔF_1 from ΔF^*) is commonly accepted and improves experimental results (e.g., Iland et al., 2007), it has also been criticized. Reguera et al. (2003) note that a hypothetical particle or drop which consists of only one molecule is not the same as one vapor molecule. In particular the molecular density of one solid or liquid molecule is not the same as one vapor molecule.

Consequently, ΔF_1 should account for the energy which is needed to transform a vapor molecule to a liquid or solid particle and should not be zero.

The nucleation rate $J_{\mathrm{hom,CNT}}$, derived in the framework of classical nucleation theory, is able to predict the rough dependencies of the nucleation rate. However, comparisons with experiments still yields differences on the order of several orders of magnitude. Iland et al. (2007) compare laboratory measurements of the homogeneous nucleation of Argon droplets with the classical nucleation theory and find differences on the order of 16 - 26 orders of magnitude. When the same laboratory results are compared to the self-consistent kinetic theory by Girshick and Chiu (1990), the difference amounts to 11 - 17 orders of magnitude. The best agreement between theory and experiment is obtained for the thermodynamically consistent theory by Kashchiev (2003), but the differences are still on the order of 5 - 7 orders of magnitude. The discrepancy between the experimental data and all three theories increases towards lower temperatures. Iland et al. (2007) conclude that 'it is impressive how poorly nucleation in such a simple system such as fluid argon is described by existing theories'. On the other hand, the analysis of experimental data for the nucleation of water droplets by Kashchiev (2006) looks by far more promising. He compares the experimentally determined nucleation rate with the nucleation rate derived from an extended classical nucleation theory. This theory includes (a) the self-consistent correction by Girshick and Chiu (1990), (b) the inclusion of the translational-rotational motion of the clusters by adding $4k_bT \ln i$ to ΔF_i (Reguera and Rubí, 2001), and (c) a fit of $\Delta p = p_{\mathrm{ice}} - p_{\mathrm{vapor}}$ inferred from the experiments by Obeidat et al. (2004). The experimental data are described quite successfully by this theory. The temperature dependence and saturation dependence are very well captured. Only at large nucleation rates (low temperatures and large saturations), the slope of the theoretical $J(S)$ curve deviates from the measurements, but the difference stays below one order of magnitude. This agreement is considerably better than the comparisons presented by Iland et al. (2007).

The study of Iland et al. (2007) and Kashchiev (2006) both demonstrate that correction terms to the classical nucleation theory are necessary, in order to bring experiments and theory into agreement. However, the here applied successful corrections only apply to the homogeneous nucleation of single component systems. More complex systems, for example the heterogeneous nucleation on preexisting ice nuclei, might need different correction terms.

2.1.4 Heterogeneous nucleation

In contrast to homogeneous nucleation, heterogeneous nucleation occurs on preexisting ice nuclei. The ice nuclei lower the energy barrier for creating the new phase which facilitates nucleation. Under conditions where homogeneous nucleation is impossible, heterogeneous nucleation might be feasible if ice nuclei are available. The reason for

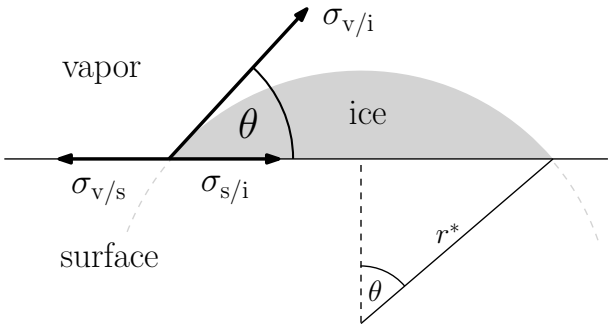

Figure 2.5: Illustration of surface tension interaction and resulting contact angle θ.

lowering the energy barrier is the following: Growth of a cluster (or in general the condensed phase) is energetically favored at a given saturation ratio if the radius of curvature is larger than the critical radius. When a nucleus is present, the molecules must only form an ice cap and not a complete sphere, which requires significantly fewer molecules for the same curvature of the surface. As shown from geometrical considerations (see below), the contribution to ΔF which arises from creating the interface is greatly reduced for an ice cap, due to the preexisting interface between the vapor phase and the nucleus. As a result, $\Delta F_{\text{het}} \leq \Delta F_{\text{hom}}$, which makes heterogeneous nucleation more likely than homogeneous.

Energy of cluster formation

For the following, it is assumed that the nucleus is wettable but non soluble and does not carry a charge. The condensed phase will then form a cap, which is generally assumed to be spherical, as depicted in Fig. 2.5. The shape of the cap will form in such a way that there are no net forces acting on the outer edge along the surface, i.e. the surface tension acting outward ($\sigma_{v,s}$) must equal the surface tensions acting inward ($\sigma_{s,i}$ and $\sigma_{v,i}\cos\theta$). This is given by Young's equation

$$\begin{aligned} \sigma_{v,s} &= \sigma_{s,i} + \sigma_{v,i}\cos\theta \\ \cos\theta &= \frac{\sigma_{v,s} - \sigma_{s,i}}{\sigma_{v,i}} \end{aligned} \tag{2.18}$$

with $\sigma_{v,s}$ being the surface tension between vapor and surface, $\sigma_{v,i}$ the surface tension between vapor and ice, and $\sigma_{s,i}$ the surface tension between surface and ice. The angle θ is therefore characteristic for the involved materials. However, it is not necessary to explicitly know the surface tensions which involve the surface ($\sigma_{v,s}$ and $\sigma_{s,i}$), it suffices to know the contact parameter $m = \cos\theta$.

The energy for forming an ice cap cluster which contains i molecules is given in analogy to Eq. 2.6 by

$$\Delta F_{\text{het}} = \Delta F^{\text{surf}} - ik_{\text{b}}T\ln S \tag{2.19}$$

with

$$\Delta F^{\mathrm{surf}} = \sigma_{\mathrm{v,i}} A_{\mathrm{v,i}} + \sigma_{\mathrm{s,i}} A_{\mathrm{s,i}} - \sigma_{\mathrm{v,s}} A_{\mathrm{s,i}} \tag{2.20}$$

$$= \sigma_{\mathrm{v,i}} A_{\mathrm{v,i}} \left(1 - m \frac{A_{\mathrm{s,i}}}{A_{\mathrm{v,i}}}\right). \tag{2.21}$$

The negative contribution to ΔF^{surf} originates from the previously existing vapor / surface interface at the position where the ice cap is then formed. Due to this fact, the surface energy is weighted by $(1 - mA_{\mathrm{s,i}}/A_{\mathrm{v,i}})$, which explains $\Delta F_{\mathrm{het}} \leq \Delta F_{\mathrm{hom}}$.

The factor by which the total free energy is reduced compared to a complete sphere depends on the exact geometry and requires the calculation of the surface areas $A_{\mathrm{v,i}}$ and $A_{\mathrm{s,i}}$ and the corresponding volume of the ice cap. Volmer (1939) found this factor to be

$$f(m) = \frac{(2+m)(1-m)^2}{4} \tag{2.22}$$

for a planar surface. For a curved surface with radius of curvature r_{N} this correction factor yields

$$2f(m,X) = 1 + \left(\frac{1-mX}{\phi}\right)^3 + X^3 \left[2 - 3\left(\frac{X-m}{\phi}\right) + \left(\frac{X-m}{\phi}\right)^3\right] + 3mX^2 \left(\frac{X-m}{\phi} - 1\right) \tag{2.23}$$

with

$$\phi = \left(1 - 2mX + X^2\right)^{1/2} \tag{2.24}$$

and

$$X = \frac{r_{\mathrm{N}}}{r^*}. \tag{2.25}$$

This factor is also known as Fletcher factor due to the original publication of Fletcher (1958). The free energy for forming an ice cap is thus $\Delta F_{\mathrm{het}} = f \Delta F_{\mathrm{hom}}$. Figure 2.6 shows $f(m,X)$ as a function of X for different values of m. The lowest values of $f(m,X)$ are obtained for large contact parameters m (small contact angles) and for large values of X, i.e. when the preexisting ice nuclei is large compared to the critical radius. Under these conditions, heterogeneous nucleation is greatly facilitated due to the reduced nucleation barrier. Since the fletcher factor only affects the 'height' of the nucleation barrier but not its position, the critical radius is unaffected by the preexisting nucleus.

Heterogeneous Nucleation Rate

The idea for the heterogeneous nucleation process is the same as for homogeneous nucleation: Clusters of different sizes exist in dynamical equilibrium, and when a

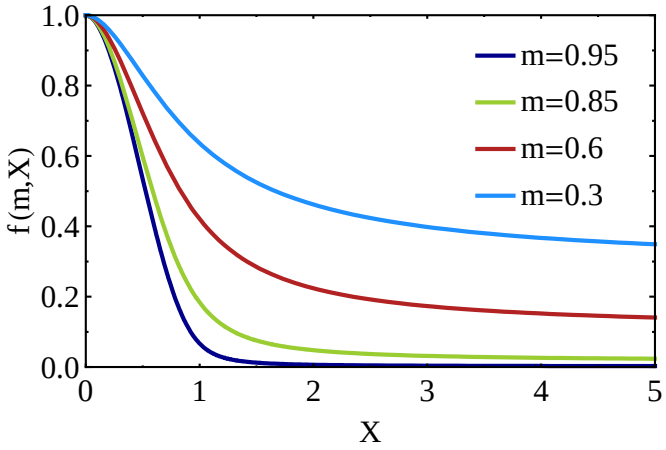

Figure 2.6: Fletcher factor $f(m, X)$ as function of X for different values of m.

cluster of critical size is joined by an additional molecule, the critical cluster becomes supercritical and starts growing. The nucleation rate per surface area can therefore be formulated as $J_{\text{het}} = Z_{\text{het}} c_{\text{s}}^* \Phi$, the surface number density of critical clusters c_{s}^* times the flux of molecules to the cluster. In analogy to homogeneous nucleation, the Zeldovich factor Z_{het} accounts for non-equilibrium effects. For a nucleation rate in the units of particles per unit volume and unit time, J_{het} has to be multiplied by the available surface area, which is the number density of ice nuclei N_{N} times $4\pi r_{\text{N}}^2$.

The surface number density of critical clusters c_{s}^* is expected to form from the surface monomer density $c_{1,\text{s}}$ according to

$$c_{\text{s}}^* = c_{1,\text{s}} \cdot \exp\left(-\frac{\Delta F_{\text{het}}^*}{k_b T}\right) \tag{2.26}$$

where $F_{\text{het}}^* = f F_{\text{hom}}^*$. The difficulty in determining the heterogeneous nucleation rate arises in the question of the monomer density $c_{1,\text{s}}$. The monomer density is commonly deduced by assuming that the flux towards the surface $w^{\downarrow}$ is equal to the flux escaping from the surface $w^{\uparrow}$

$$\begin{aligned} w^{\downarrow} &= w^{\uparrow} \\ \frac{p_{\text{H}_2\text{O}}}{\sqrt{2\pi m_{\text{w}} k_b T}} &= c_{1,\text{s}} \nu_{\text{s}} \exp\left(-\frac{\Delta F_{\text{des}}}{k_b T}\right) \\ \Longrightarrow \quad c_{1,\text{s}} &= \frac{p_{\text{H}_2\text{O}}}{\sqrt{2\pi m_{\text{w}} k_b T \nu_{\text{s}}}} \exp\left(\frac{\Delta F_{\text{des}}}{k_b T}\right) \end{aligned} \tag{2.27}$$

with the desorption energy ΔF_{des} and the vibration frequency ν_{s} of molecules situated on the surface.

The next term in the equation for the nucleation rate is the flux Φ of monomers to the critical cluster. Two different mechanisms are possible for this process: The monomers can either be already adsorbed onto the surface of the substrate and join the cluster via surface diffusion, or they can be deposited directly from the gas phase onto the critical cluster.

The joining rate for the surface diffusion process is given by the number of molecules which can reach the cluster within one diffusional step times the frequency in which surface diffusion steps occur. The adsorbed molecules, which are ready to join the cluster, are situated in an annulus around the critical cluster with width $\bar{\delta}$ (mean diffusion jump distance) and radius $r^* \sin\theta$ (see Fig. 2.5). The frequency with which an adsorbed molecule undergoes one diffusional jump is $\nu_{\mathrm{s}} \exp\left(-\frac{\Delta F_{\mathrm{sd}}}{k_b T}\right)$, where ΔF_{sd} is the activation energy for surface diffusion. In combination this yields

$$\Phi_{\mathrm{SD}} = c_{1,\mathrm{s}} \cdot \bar{\delta}\, 2\pi \sin\theta \cdot \nu_{\mathrm{s}} \exp\left(-\frac{\Delta F_{\mathrm{sd}}}{k_b T}\right). \tag{2.28}$$

The joining rate for the direct deposition process is given by the vapor flux times the cross sectional area of the ice cap, which is

$$\Phi_{\mathrm{DD}} = \frac{p_{\mathrm{H_2O}}}{\sqrt{2\pi m_{\mathrm{w}} k_b T}} \cdot \pi r^{*2}. \tag{2.29}$$

The ratio of both fluxes simplifies to $\Phi_{\mathrm{SD}}/\Phi_{\mathrm{DD}} = \exp((\Delta F_{\mathrm{des}} - \Delta F_{\mathrm{sd}})/k_b T)$, under the assumption that $r^* \sin\theta$ is of the same order as $\bar{\delta}$. Since the surface diffusion energy is expected to be smaller than the desorption energy, the ratio $\Phi_{\mathrm{SD}}/\Phi_{\mathrm{DD}} > 1$. For mesospheric conditions and the typically assumed values of ΔF_{des} and ΔF_{sd}, the ratio is 2×10^6 which means that surface diffusion is the faster and therefore dominant process. For this reason only nucleation by surface diffusion will be considered in the following.

The Zeldovich factor for heterogeneous nucleation is in analogy to Eq. 2.14

$$Z_{\mathrm{het,planar}} = \sqrt{\frac{\Delta F^*_{\mathrm{het}}}{3\pi k_b T n^{*2}_{\mathrm{het}}}} \tag{2.30}$$

$$= \frac{1}{\sqrt{f}} Z_{\mathrm{hom}} \tag{2.31}$$

since $n^*_{\mathrm{het}} = f n^*_{\mathrm{hom}}$ (Sigsbee, 1969, Eqs. 35 and 72). Vehkamäki et al. (2007) pointed out that this form of the heterogeneous Zeldovich factor is only valid for flat surfaces and introduced the correct form for spherical ice caps as

$$Z_{\mathrm{het,spherical}} = Z_{\mathrm{hom}} \sqrt{\frac{4}{2 + \frac{(1+mX)[2-4mX-(m^2-3)X^2]}{(1-2mX+X^2)^{3/2}}}}. \tag{2.32}$$

Combining Eqs. 2.26, 2.27, and 2.28 yields the rate for heterogeneous nucleation per ice nucleus

$$\begin{aligned} J_{\mathrm{het}}/N_{\mathrm{N}} &= Z_{\mathrm{het}}\, c^*_{\mathrm{s}}\, \Phi_{\mathrm{SD}} \\ &= 4\pi r^2_{\mathrm{N}} \frac{Z_{\mathrm{het}} \bar{\delta} p^2_{\mathrm{H_2O}} r^* \sin\theta}{\nu_{\mathrm{s}} m_{\mathrm{w}} k_b T} \exp\left(\frac{2\Delta F_{\mathrm{des}} - \Delta F_{\mathrm{sd}} - f\Delta F^*}{k_b T}\right). \end{aligned} \tag{2.33}$$

Figure 2.7 shows the nucleation rate per particle for typical mesospheric conditions in dependence of the nucleus radius r_{N}, of temperature T and saturation S.

Heated ice nuclei

The results presented in this section have been derived by the author of this thesis and are published in Asmus et al. (2014).

Under certain circumstances the ice nuclei can have a different temperature than the surrounding gas, as for example MSPs, the ice nuclei for mesospheric clouds (see Ch. 4). Under such conditions, the classical nucleation theory as expressed above needs to be modified to account for the two different temperatures. The basic concepts remain unchanged, only the nucleation barrier and the critical radius need to be corrected and the individual temperature dependencies in Eq. 2.33 need to be identified, i.e., whether they are determined by the nucleus temperature T_{P} or the surrounding gas temperature T_{A}.

The critical radius is in equilibrium with the surrounding gas, i.e., $w^{\downarrow} = w^{\uparrow}$. With Eqs. 2.4, 2.5, and 2.1 the critical radius with different temperatures in gas and ice phase evaluates to

$$r^*_{\mathrm{H}} = \frac{2\sigma m_{\mathrm{w}}}{\rho_{\mathrm{ice}} k_b T_{\mathrm{P}} \ln S_z} \tag{2.34}$$

with $S_z = p_{\mathrm{H_2O}}/p_{\mathrm{sat}}(T_{\mathrm{P}}) \sqrt{\frac{T_{\mathrm{P}}}{T_{\mathrm{A}}}}$ (Lazzati, 2008). The comparison with r^* (Eq. 2.3) shows that only the saturation ratio has been corrected with the ratio of the two temperatures. For $T_{\mathrm{P}} > T_{\mathrm{A}}$ the critical radius is shifted to larger values, mainly due to

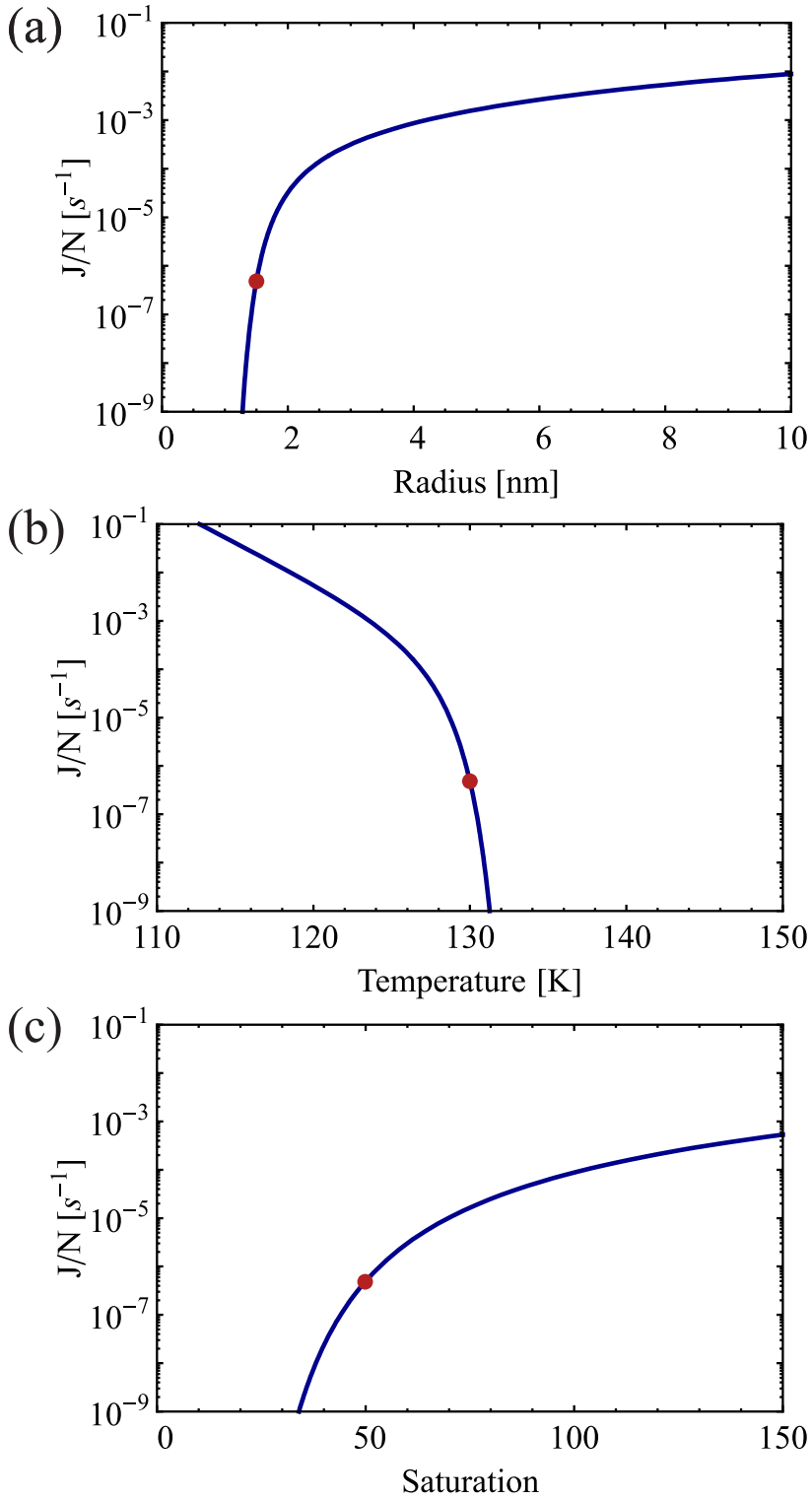

Figure 2.7: Heterogeneous nucleation rate per particle for typical mesopause conditions as function of (a) nucleus radius, (b) temperature and (c) saturation. The red dots indicate the values which are used if this variable is constant in one of the other plots of this figure.

the temperature dependence of $p_{\mathrm{sat}}(T_{\mathrm{P}})$. This is demonstrated in Fig. 2.8(a), which shows r_{H}^* as a function of $\Delta T = T_{\mathrm{P}} - T_{\mathrm{A}}$.

In order to determine the nucleation barrier, the surface effects are neglected at first. The concept of detailed balance is applied, which assumes that a steady state cluster size distribution is formed. A steady state is reached when the attachment rate of one molecule to a cluster with $n-1$ molecules is balanced by the detachment rate of a cluster with n molecules

$$w^{\downarrow} A_{n-1} c_{n-1} = w^{\uparrow} A_n c_n \tag{2.35}$$

where A is the surface area of the cluster and c_n the number density of clusters with n molecules. Using Eq. 2.4, 2.5, and 2.1 and neglecting the surface area difference ($A_{n-1}/A_n = 1$ for sufficiently large cluster), c_n can be expressed as

$$c_n = c_{n-1} S_z \exp\left(-\frac{2 m_w \sigma}{k_b T_P \rho_{\mathrm{ice}}} \left(\frac{4\pi}{3nv}\right)^{1/3}\right). \tag{2.36}$$

The number density c_{n-1} can be expressed through c_{n-2}, which in turn can be calculated from c_{n-3}, ... and c_2 eventually from the monomer concentration c_1

$$c_n = c_1 \prod_{j=2}^{n} S_z \exp\left(-\frac{2 m_w \sigma}{k_b T_P \rho_{\mathrm{ice}}} \left(\frac{4\pi}{3jv}\right)^{1/3}\right) \tag{2.37}$$

$$= c_1 \exp\left(n \ln S_z - \frac{3 m_w \sigma}{k_b T_P \rho_{\mathrm{ice}}} \left(\frac{4\pi}{3v}\right)^{1/3} n^{2/3}\right). \tag{2.38}$$

In the second equation the product has been expressed as a sum within the exponential function, which is then transformed into an integral $\sum_{j=2}^{n} \to \int_0^n \mathrm{d}j$. The lower boundary can safely be shifted from $j = 2$ to $j = 0$ as mainly the number density of critical size clusters with a few hundred molecules is of interest. For $S_z < 1$ the number density c_n is a monotonically decreasing function of n; for $S_z > 1$ the number density has a local minimum at $n = n^*$ (as in Fig. 2.4). Evaluating n^* from $\frac{\partial c_n}{\partial n} = 0$ yields

$$n_{\mathrm{H}}^* = \frac{4\pi}{3v} \left(\frac{2 m_{\mathrm{w}} \sigma}{k_b T_P \rho_{\mathrm{ice}} \ln S_z}\right)^3 = \frac{4\pi}{3v} {r_{\mathrm{H}}^*}^3 \tag{2.39}$$

The number density of clusters of critical size is therefore

$$c_{n_{\mathrm{H}}^*} = c_1 \exp\left(-\frac{\Delta F_{\mathrm{H}}^*}{k_b T_P}\right) \tag{2.40}$$

with

$$\Delta F_{\mathrm{H}}^* = \frac{16\pi\sigma^3 m_{\mathrm{w}}^2}{3(k_b T_P \rho_{\mathrm{ice}} \ln S_z)^2}. \tag{2.41}$$

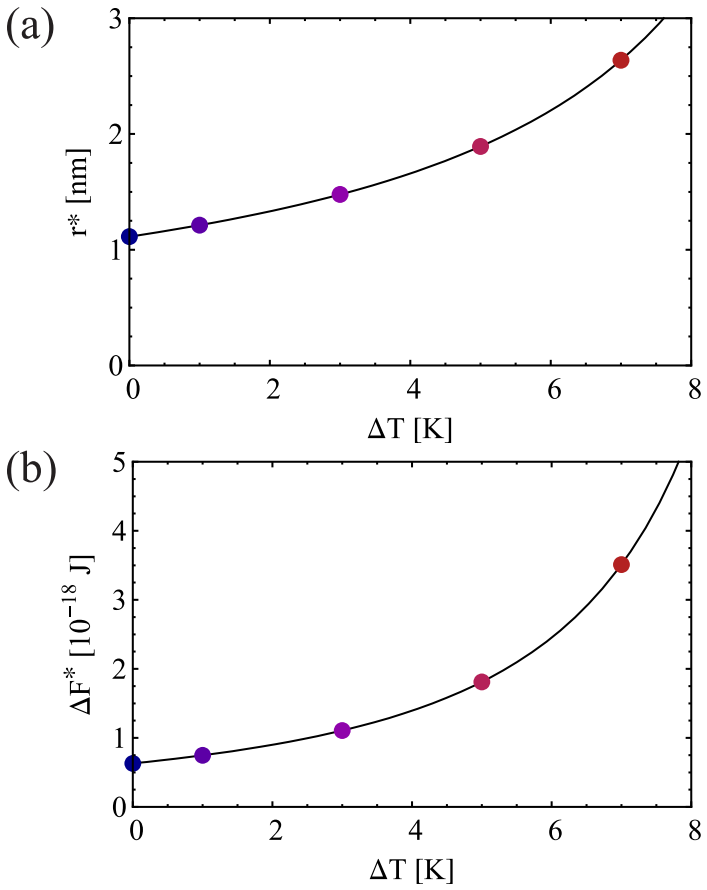

Figure 2.8: (a) Critical radius r_{H}^{*} and (b) nucleation barrier $\Delta F_{\mathrm{H}}^{*}$ as function of ΔT. The colored dots refer to the cases shown in Fig. 2.9.

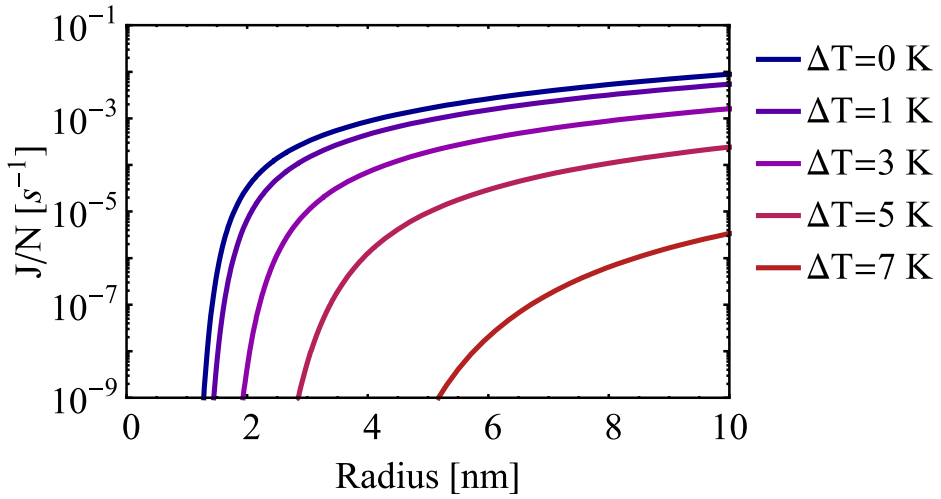

Figure 2.9: Nucleation rate per particle for different $\Delta T = T_\mathrm{P} - T_\mathrm{A}$ (adopted from Asmus et al. (2014)).

The dependence of the nucleation barrier ΔF^*_H on ΔT is demonstrated in Fig. 2.8(b).

With the modified critical radius and nucleation barrier, the heterogeneous nucleation rate can be formulated as

$$J_\mathrm{het,H}/N_\mathrm{N} = 4\pi r_\mathrm{N}^2 \frac{Z_\mathrm{het,H} \bar{\delta} p^2_{\mathrm{H_2O}} r^*_\mathrm{H} \sin\theta}{\nu_\mathrm{s} m_\mathrm{w} k_b T_\mathrm{A}} \exp\left(\frac{2\Delta F_\mathrm{des} - \Delta F_\mathrm{sd} - f\Delta F^*_\mathrm{H}}{k_b T_\mathrm{P}}\right). \tag{2.42}$$

The temperature dependence of the exponential term is determined by the nucleus temperature T_P, since desorption and surface diffusion are controlled by the surface properties. The explicit temperature dependence in the denominator of the preexponential term originates from the incoming vapor flux which determines the monomer concentration (see Eq. 2.27), thus it depends on the gas temperature T_A. This is the only term where T_A enters the equation, all other implicit temperature dependencies (e.g., the Zeldovich factor) have to be evaluated at T_P.

Figure 2.9 shows the nucleation rate for different temperature offsets between surrounding atmosphere and nucleus. It shows that already a small offset of a few Kelvin reduces the nucleation rate by several orders of magnitude.

Limitations

The nucleation rate as expressed above relies on several assumptions, where the applicability is questionable, in particular to mesospheric conditions. As mentioned above, the capillarity approximation assumes that the concept of surface tension can be applied to microscopic systems, which contain only a few hundred molecules or less.

For example, the ice cap of a critical cluster with $r^* = 1.1\,\text{nm}$ on a 1.2 nm nucleus with $m = 0.95$ contains only 30 molecules. Even if the capillarity approximation could be applied, the surface tension has not been measured in the relevant temperature range. The parametrization of the surface tension by Hale and Plummer (1974) is commonly used for microphysical calculations of NLCs (Turco et al., 1982; Berger and Zahn, 2002), however, the parametrization is based on a linear extrapolation from measurements performed above 235 K down to mesospheric temperatures around 130 K.

When applying classical nucleation theory to heterogeneous nucleation on MSPs, the ice nuclei are assumed to be perfect spheres with no surface inhomogeneities. This means there are no preferred nucleation sites and no barriers for surface diffusion. However, Saunders and Plane (2006) found in laboratory experiments of meteor smoke analogues that for example iron containing MSPs have an amorphous structure and are fractal and chain like. This is completely contrary to the assumptions in classical nucleation theory.

The contact angle, which enters the nucleation rate via m, describes how 'wettable' a surface is or how well the lattices of nucleus and ice fit to each other. Roddy (1984) systematically searched for substances that have crystal structures similar to cubic ice and thus have a small misfit parameter. For wüstite (FeO) and other meteoric materials the misfit parameter with respect to cubic ice is comparable to the misfit parameter of silver iodide with respect to hexagonal ice. Since silver iodine is a very efficient ice nucleus for hexagonal ice (Vonnegut, 1947), MSPs are assumed to be efficient ice nuclei as well and a large value of $m = 0.95$ (e.g., Rapp and Thomas, 2006; Bardeen et al., 2010) or $m = 0.97$ (Määttänen et al., 2005; Wood, 1999) has been chosen in previous modelling studies of mesospheric ice. However, Bardeen et al. (2010) have also varied m over a wide range to reflect the large uncertainty of the contact parameter. Trainer et al. (2009) deduced the temperature dependence of m based on laboratory measurements on a monocrystalline silicon wafer and the applicability of classical nucleation theory. They find contact parameters as low as 0.6 for temperatures of 150 K. In the mesopause region with temperatures around 130 K even smaller values for m would be expected based on the measurements of Trainer et al. (2009). Besides the uncertainty in the contact angle, it should also be noted that m depends on the vapor pressure $p_{\text{H}_2\text{O}}$ (i.e. the conditions of the surrounding atmosphere), m depends on whether the cluster is growing or evaporating (contact angle hysteresis) and m is influenced by the roughness of the surface and hydrophilic adsorption sites on the surface (Pruppacher and Klett, 1997, Ch. 5.5 and 5.6). Changing m from 0.95 to only 0.93 reduces the nucleation rate by three orders of magnitude. This demonstrates the high sensitivity of the nucleation rate on m and consequently also the uncertainty introduced by the contact angle.

Another critical parameter, if not the most critical parameter, is the desorption energy ΔF_{des} as it occurs in the exponential term of Eqs. 2.33 and 2.42 with a positive sign. The value of $\Delta F_{\text{des}} = 2.9 \times 10^{-20}\,\text{J}$ which is commonly used (Keesee, 1989; Määttänen

et al., 2005) is taken from Seki and Hasegawa (1983), who estimated the desorption energy from the wetting energy of water to $\alpha - SiO_2$. It is needless to say that this value might change considerably for different substrate materials and crystal modifications (crystalline or amorphous). The desorption energy even varies on a single surface, depending on the position where the water molecule is adsorbed (Stimpfl et al., 2006). Consequently, the effective desorption energy should also depend on the number density of adsorbed molecules, i.e. on $c_{1,s}$. Reducing ΔF_{des} by 30% lowers the nucleation rate by four orders of magnitude. Thus, uncertainties in ΔF_{des} cause a great uncertainty of the nucleation rate.

The desorption energy enters the equation of the nucleation rate because this energy is used to estimate the surface density of single water molecules on the ice nuclei, i.e. the monomer density $c_{1,s}$ given by Eq. 2.27. According to this equation and for typical conditions of 130 K and water vapor mixing ratio of 2 ppm at 87 km, the monomer concentration would be $c_1 = 3 \times 10^6\,cm^{-2}$. Other studies, e.g. Trainer et al. (2009), used $c_{1,s} = 1 \times 10^{15}\,cm^{-2}$, which corresponds to the surface density of an ice monolayer. As $c_{1,s}$ squared contributes to the nucleation rate (Pruppacher and Klett, 1997), uncertainties in the monomer concentration have a large contribution to the uncertainty of J_{het}.

However, besides the uncertainty in the exact value of $c_{1,s}$, it is questionable whether water molecules in general exist as monomers on the surface of MSPs, as water molecules have the ability to form hydrogen bonds with their neighbors. The absence of hydrogen bonds can have two reasons (Henderson, 2002): First, kinetic constraints may prevent water-water interactions (i.e. hydrogen bonds). Second, water-surface interactions may be dominating and thus hindering water-water interactions. However, if the water-surface interactions are too strong, the water will be dissociated. Henderson (2002) gives a detailed discussion on those different cases. He concludes that 'monomeric water is a rare state of water on most surfaces, with clustering and dissociation being the predominate forms of adsorbed water' (Henderson, 2002). If this is also valid for adsorbed water on MSPs, the currently assumed nucleation theory must be reconsidered, as it relies on the assumption that the majority of water molecules exist as monomers, which then form dimers, trimers and so forth until the critical radius is reached.

It should be mentioned here that an ice nucleus which carries a charge additionally alters several nucleation properties. As charged MSPs are not considered in the following, the reader is directed to the detailed discussion of Gumbel and Megner (2009) and Megner and Gumbel (2009).

The foregoing discussion illustrates our lack of knowledge concerning the nucleation process under mesospheric conditions. Some basic concepts are questionable and many values of crucial parameters have not yet been determined in laboratory experiments. Until these issues are resolved we have to rely on the currently used classical nucleation theory and must be aware that the nucleation rate is highly uncertain. The sensitivity

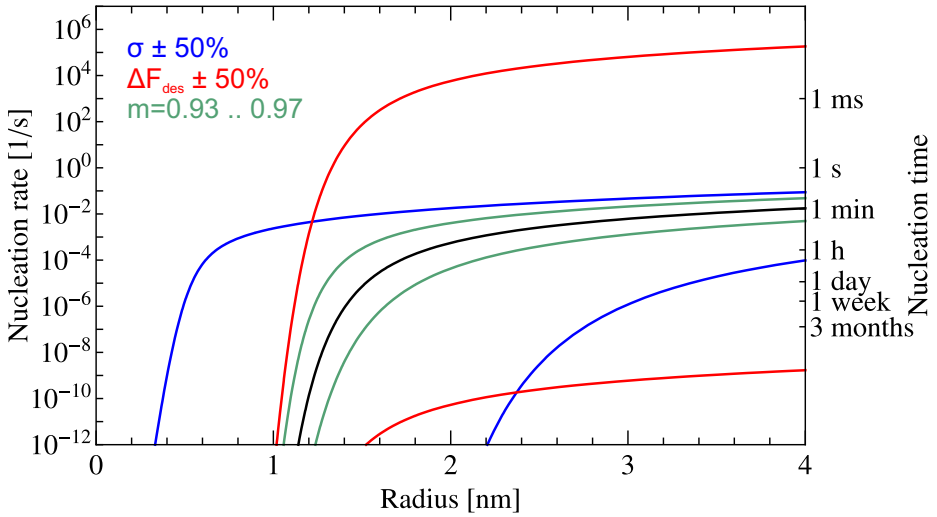

Figure 2.10: Uncertainty of the nucleation rate, demonstrated by varying the desorption energy ΔF_{des} by $\pm$ 50%, the surface tension σ by $\pm$ 50% and the contact parameter from 0.93 to 0.97. The corresponding time to nucleate one particle is shown on the right hand scale. The nucleation rates are calculated for a background temperature of 130 K and water vapor mixing ratio of 2 ppm at 0.3 Pa background pressure. This figure is reproduced from Wilms et al. (2016).

of the nucleation rate to some of the above discussed parameters is visualized in Figure 2.10.

2.2 Particle growth

A cluster continues to grow after nucleation according to the difference between the flux directed towards the particle and the evaporation flux

$$\frac{\mathrm{d}}{\mathrm{d}t} m = m_{\mathrm{w}} \left(w^{\downarrow} - w^{\uparrow} \right) 4\pi r^2 \tag{2.43}$$

$$= \frac{m_{\mathrm{w}}}{\sqrt{2\pi k_b T}} \left(p_{\mathrm{H_2O}} - p_{\mathrm{sat}} \right) 4\pi r^2. \tag{2.44}$$

In terms of radius change this can be rewritten to

$$\frac{\mathrm{d}}{\mathrm{d}t} r = \frac{1}{\rho_{\mathrm{ice}}} \sqrt{\frac{m_{\mathrm{w}}}{2\pi k_b T}} \, p_{\mathrm{sat}} \, (S - 1). \tag{2.45}$$

These equations hold as long as the ice particle is much smaller than the mean free path of the surrounding gas, i.e. the growth takes places in the kinetic regime where the Knudsen number (ratio of mean free path to typical dimension of object) is large. At 85 km altitude the mean free path is about 1 cm, compared to ice particles in the size of nanometers, so that the Knudsen number is much larger than one.

For the equation above it is assumed that every molecule hitting the ice particle sticks to its surface, i.e. the sticking coefficient is one. Brown et al. (1996) performed molecular beam experiments where water molecules were condensated on ice multilayers on Rubidium. They found a sticking coefficient of $\alpha = 0.99 \pm 0.03$ in the temperature range between 85 K and 150 K. A high sticking coefficient is expected if the energy transfer between impinging water molecule and ice surface is very efficient (i.e., when the surface is composed of molecules of an equivalent mass). In such a case the excess energy, which is released by forming the new hydrogen bond, is effectively transferred to the underlying bulk material and thus prevents the escape of the condensed molecule (Brown et al., 1996). The following microphysical simulations are therefore performed with a sticking coefficient of unity.

2.3 Summary

The phase transition from water vapor to small ice crystals is commonly described by classical nucleation theory. This theory assumes that thermal fluctuations in supersaturated water vapor lead to the spontaneous formation of water clusters of various sizes. As soon as a cluster exceeds the critical radius, further growth of that cluster is energetically favored. However, to reach the critical radius, the energy barrier ΔF^* has to be overcome. Preexisting ice nuclei lower this energy barrier, thus facilitating the nucleation process. For the formation of mesospheric ice particles, MSPs are believed to serve as ice nuclei. However, classical nucleation theory relies on several assumptions, which might not be applicable to mesospheric conditions. Additionally, critical parameters have not been experimentally determined for the extreme conditions of the polar summer mesopause. This leads to an uncertainty of the nucleation rate of several orders of magnitude.

In classical nucleation theory, it is assumed that the temperature of the ice nucleus is equal to the temperature of the surrounding gas. This assumption might not be true for MSPs at the summer polar mesopause, since these MSPs could be warmer than the ambient atmosphere. Thus, the classical nucleation theory has been extended to account for a possible temperature difference between MSPs and the ambient atmosphere. A positive temperature difference increases the critical radius r^* as well as the nucleation barrier ΔF^*. Only those MSPs which are larger than r^* can act as ice nuclei, so that an increase of r^* due to warmer MSPs reduces the number of possible ice nuclei.

The increase of the nucleation barrier ΔF^* results in generally lower nucleation rates. The overall effect of a positive temperature difference between MSPs and ambient atmosphere is that the nucleation process takes longer and that fewer MSPs can act as ice nuclei.

3 Model description

In this chapter the microphysical model CARMA is introduced. The setup for the simulations presented in this thesis is described, as well as the background fields required by the CARMA model. Additionally, the capabilities of the microphysical model are demonstrated with a set of exemplary simulations.

3.1 Community Aerosol and Radiation Model for Atmospheres

CARMA, the Community Aerosol and Radiation Model for Atmospheres, is a microphysical model with a flexible setup, which can be applied to a variety of aerosol and cloud problems. The original one-dimensional CARMA code developed by Turco et al. (1979) and Toon et al. (1979) was later extended to three dimensions (Toon et al., 1988) and adapted to mesospheric conditions (Turco et al., 1982; Jensen and Thomas, 1989) for NLC studies (e.g., Rapp et al., 2002; Merkel et al., 2009; Stevens et al., 2010; Russell III et al., 2010; Siskind et al., 2011; Chandran et al., 2012).

The CARMA model for NLC studies comprises three constituents: MSPs, ice particles and water vapor. These constituents are able to interact via the following reactions: nucleation of MSPs to form ice particles, deposition of water vapor onto ice particles for their growth, sublimation of ice particles with release of water vapor (and in the case of total evaporation with release of MSPs), and coagulation. Coagulation of MSPs is considered, coagulation of ice particles and also coagulation of MSPs with ice particles. Water vapor is additionally dissociated by Lyman-α radiation. These processes are visualized in Fig. 3.1.

Ice particles and aerosols are calculated as number densities, which are resolved in grid boxes and radius bins. The above mentioned processes are calculated individually for each gridbox and size bin. The nucleation process is calculated via the heterogeneous nucleation rate given by Eq. 2.42. The growth and evaporation of ice particles is treated via the kinetic growth rates (see Eq. 2.45). Coagulation is determined using a Brownian coagulation kernel (see Pruppacher and Klett, 1997, Ch. 15 and Jacobson et al., 1994). Photodissociation of water vapor is parametrized as described by Jensen (1989).

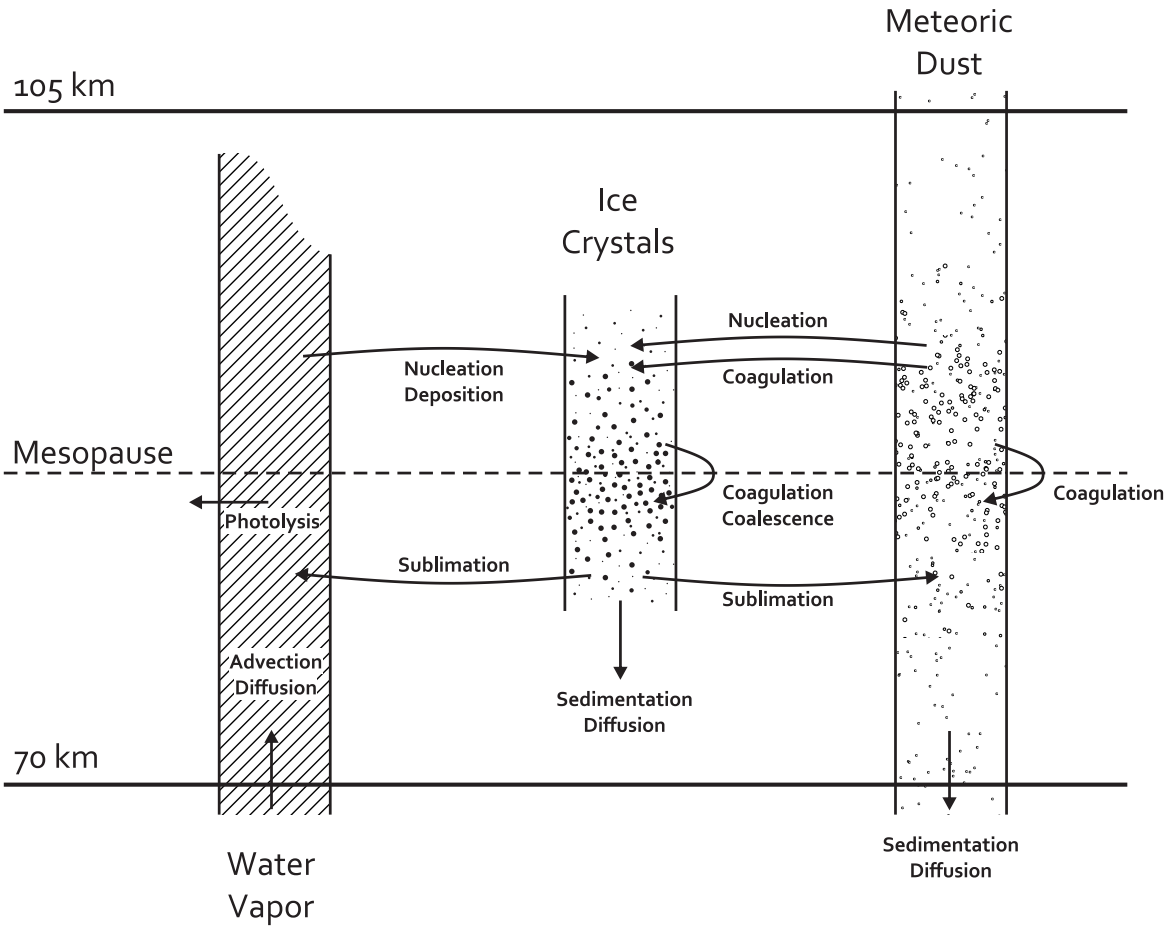

Figure 3.1: Schematic diagram of CARMA showing the basic constituents and their interactions (drawn after Jensen and Thomas, 1989).

An Eulerian transport scheme handles the transport of particles and water vapor due to background winds, eddy diffusion and sedimentation (particles only). The piecewise parabolic method by Colella and Woodward (1984) calculates advection in physical space and radius space (growth of particles). In a one-dimensional setup (as in this study), a divergence correction is applied in order to fulfill the continuity equation according to Jensen and Thomas (1989): A divergent vertical flow is thereby compensated by horizontal advection from virtual neighboring boxes with identical properties, which brings aerosol particles and water vapor into the considered gridbox (and vice versa for a convergent vertical flow).

The size distribution of aerosol particles is resolved in 40 size bins with mass doubling between adjacent bins, starting from minimal radii of 0.2 nm for MSPs and 2 nm for ice particles. The model domain covers the altitude range from 72 km to 102 km in 120 equidistant levels of 250 m thickness. The time step is set to 100 s for all slow processes

like transportation and coagulation. The fast microphysical processes nucleation and growth are calculated on shorter time scales, where the time step is adjusted according to the current microphysical conditions of each grid box. The length of each simulation was set to 48 h.

From the model output, the total number density and mean radius of the ice particles is calculated via

$$n_{\mathrm{tot}} = \int_0^\infty \frac{\mathrm{d}N}{\mathrm{d}r}\,\mathrm{d}r \tag{3.1}$$

and

$$r_{\mathrm{mean}} = \int_0^\infty r\,\frac{\mathrm{d}N}{\mathrm{d}r}\,\mathrm{d}r, \tag{3.2}$$

respectively, where $\mathrm{d}N/\mathrm{d}r$ denotes the ice particle size distribution. The backscatter coefficient β is calculated via

$$\beta = \int_0^\infty \pi r^2 Q_{\mathrm{sca}}(\lambda, r, n)\frac{\mathrm{d}N}{\mathrm{d}r}\,\mathrm{d}r \tag{3.3}$$

with the scattering efficiency Q_{sca} as a function of wavelength λ, particle radius r and refractive index n. The backscatter coefficient always refers to a wavelength of $\lambda = 532\,\mathrm{nm}$, which is a frequently used wavelength for lidar detection of NLCs (e.g., Baumgarten et al., 2008; Thayer et al., 2003). The scattering efficiency is calculated from Mie theory (Bohren and Huffman, 1983) for spherical ice particles, or from T-matrix calculations (Mishchenko and Travis, 1998) for spheroids. If not mentioned otherwise, the ice particles are assumed to be spherical.

The modeled NLCs are classified by their backscatter coefficient β into different brightness classes (Fiedler et al., 2011): Faint NLCs (in units of $10^{-10}\,\mathrm{m^{-1}\,sr^{-1}}$) refer to those with $1 < \beta < 4$, weak NLCs have $4 < \beta < 7$, medium NLCs are characterized by $7 < \beta < 13$, and strong NLCs by $\beta > 13$.

This study builds on the CARMA model used by Rapp and Thomas (2006) with several improvements:

- The background state of the mesopause region can either be described by climatological profiles as in the setup by Rapp and Thomas (2006) or with wave driven profiles taken from KMCM (Kühlungsborn Mechanistic general Circulation Model, see Sec. 3.2.2). The KMCM profiles of temperature, density, pressure and wind are updated in CARMA every 600 s. The climatological and wave driven background profiles is shown in Figs. 3.2 and 3.3, respectively.

- The updated dust profile from the global and seasonal MSP model by Megner et al. (2008b) for July conditions at 68° N has been incorporated into CARMA (see Sec. 3.2.3).

- Some minor changes in the code, providing more consistency in the microphysical calculations or the stability of the model, are listed in the Appendix A.1.

As in the setup of Rapp and Thomas (2006) CARMA is operated in a one-dimensional setup. This 1D setup is necessary in order to run the large number of sensitivity runs for this study in reasonable computation time.

3.2 Background profiles

The atmospheric background condition, in which the development of NLCs is studied, has to be prescribed in CARMA. Two different setups of the atmospheric background are chosen in this thesis, one setup with climatological background conditions and a second setup with wave driven background fields. Both setups have the identical initial water vapor profile, which is taken from the model simulations by Körner and Sonnemann (2001). This modeled water vapor profile fits fairly well to ground-based observations (Seele and Hartogh, 1999) and satellite observations (Hervig et al., 2009b). Vertical diffusion is based on an altitude profile of the eddy diffusion coefficient, which was determined by turbulence measurements performed under summer conditions at 69° N by Lübken (1997). Besides the atmospheric background profile, the MSP size distribution and altitude dependence has to be specified.

3.2.1 Climatological background

Simulations with climatological background fields use time independent profiles of temperature, vertical wind, pressure and density. The temperature and density profile is adopted from Lübken (1999), who derived a climatology of the thermal structure of the polar mesosphere (70° N) from falling sphere measurements. Following the suggestion of Merkel et al. (2009) and Chandran et al. (2012), the model is initialized in a warmer state to prevent unrealistic nucleation bursts in the first time step. Starting with a temperature offset of 12 K, the atmosphere is then subsequently cooled by $1\,\mathrm{K\,h^{-1}}$. The final temperature profile is reached after 12 h and the model is run for another 48 h. The vertical wind is taken from the 3D modeling results presented by Berger and Zahn (2002) for 69° N. These are the profiles which were used in previous modeling studies by Rapp and Thomas (2006). Fig. 3.2 shows the climatological profile of temperature and vertical wind.

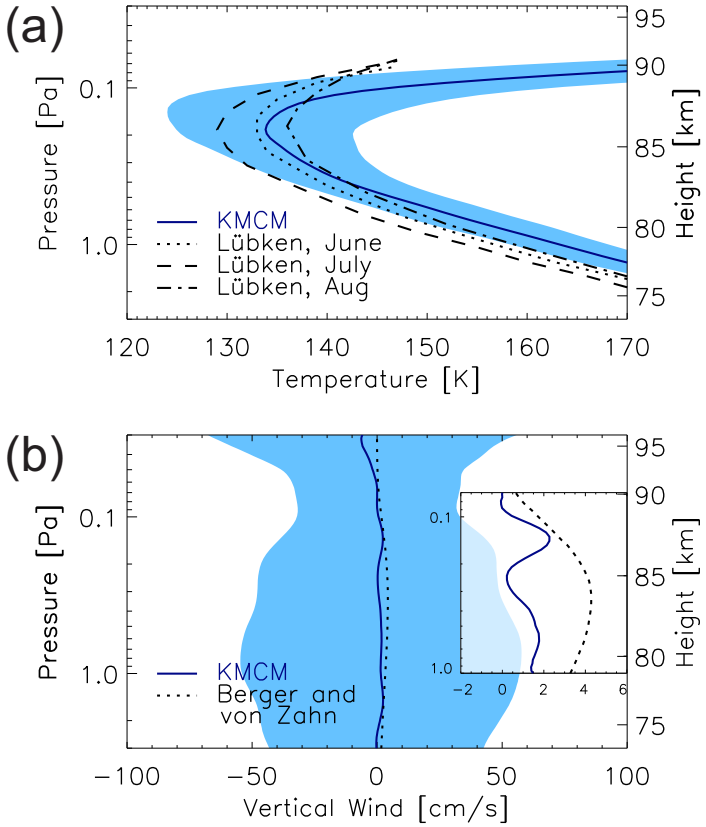

Figure 3.2: Climatological and mean KMCM profiles of (a) temperature and (b) vertical wind. The climatological temperature profiles from falling sphere measurements in June, July, and August (Lübken, 1999) are shown in panel a (dashed, dotted, and dash-dotted lines). Modeled mean vertical winds from the model of Berger and Zahn (2002) are shown in panel b (dotted line). Black solid lines show the mean profile from KMCM and the shaded area corresponds to ± one standard deviation of the mean. The smaller figure within panel b shows the same data, but with a different scale, to demonstrate the small mean values. The pressure to altitude conversion is based on the KMCM data, which differs slightly for the Lübken (1999) profiles. This figure is reproduced from Wilms et al. (2016).

3.2.2 Wave driven background

Waves can induce large deviations from the climatological state. To include their effects on the ice microphysics, the second setup incorporates the background profiles generated with the Kühlungsborn Mechanistic general Circulation Model (KMCM). The KMCM is designed to explicitly model the gravity wave drag in the extratropical upper mesosphere. The turbulent diffusive damping of resolved waves (particularly gravity waves in the mesosphere/lower thermosphere) is self-consistently induced via vertical and horizontal diffusion coefficients, which depend on the Richardson number (Becker and Burkhardt, 2007). The model is based on a dynamical core of standard spectral general circulation models (Simmons and Burridge, 1981) with truncation at total wavenumber 120, corresponding to a minimum horizontal wavelength resolved in the model of 330 km. The model comprises 190 hybrid levels from the surface to about 125 km altitude with a vertical spacing of about 600 m up to 105 km altitude. The complete model description can be found in Becker (2009). Note that tides are not included in the KMCM data.

Two weeks of KMCM data under July conditions at 69° N are used in the following. An overview over this data set is given in Figure 3.3, which shows the temperature and vertical wind fields. From the two week KMCM data set, six different starting times are chosen, such that the simulation starts in the warm phase of the dominant wave. This inhibits nucleation bursts at the beginning of the simulations. The six starting times are indicated by the vertical lines in Fig. 3.3. The mean profiles of the KMCM data set are shown in Figure 3.2 with the RMS values of the fluctuations indicated by the shaded area: Typical temperature fluctuations are on the order of 9 K and typical wind fluctuations are on the order of 0.45 m/s with maximum amplitudes of up to 1.5 m/s. Note that the climatological temperature profile for July, which is also used in this study (see Section 5.3.1) and which has been used in previous studies (e.g., Rapp et al., 2002; Rapp and Thomas, 2006), is colder than the mean KMCM profile by about 5 K. The KMCM temperature cannot simply be shifted by this offset, because the consistency with the wind, pressure and density field would then be lost. However, the mean KMCM profile lies well within the range of expected temperature profiles during the NLC season (cf. with temperature profiles for June and August). The mean vertical wind from KMCM is directed upward with a mean velocity of only a few cm/s which is similar to the values of the climatological setup.

3.2.3 MSP profiles

Two different MSP profiles are used in the CARMA simulations. The first one is based on the size distribution of the MSP model by Hunten et al. (1980), the second one is adopted from the MSP model of Megner et al. (2008b). The MSPs are initialized in

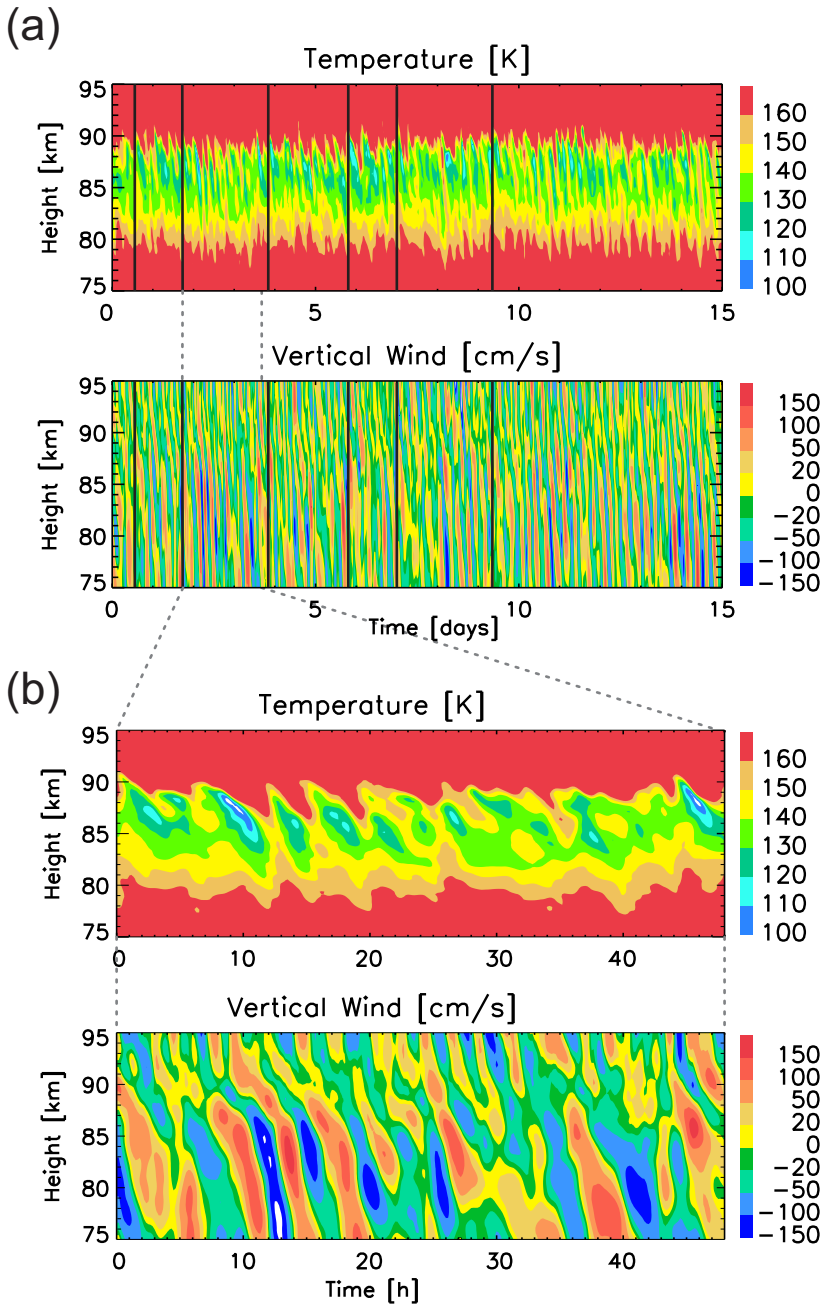

Figure 3.3: (a) KMCM time series of temperature and vertical wind velocity. Vertical lines indicate starting times of CARMA simulations. (b) One of the six background profiles used in this study. This figure is reproduced from Wilms et al. (2016).

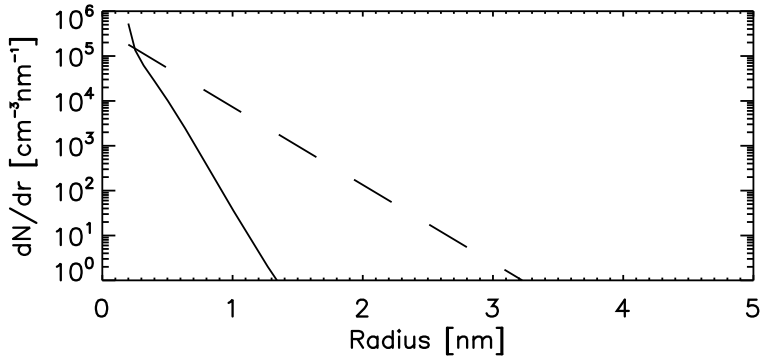

Figure 3.4: MSP size distribution of Hunten et al. (1980) (dashed) and Megner et al. (2008b) (solid) at the mesopause.

CARMA according to one of these two profiles. During the simulations, the MSPs are subject to transport (diffusion, sedimentation and wind) and coagulation as calculated within CARMA. MSPs are not replenished during the course of the simulations.

The MSP model by Hunten et al. (1980) assumes a meteoric influx of 44 t/day and calculates an MSP profile based on the following three processes: ablation of the meteoroids, recondensation of the ablated material to form MSPs, and finally coagulation, diffusion and sedimentation of MSPs in the atmosphere. The resulting MSP number densities are on the order of $10^4\,\mathrm{cm}^{-3}$ to $10^5\,\mathrm{cm}^{-3}$. The MSP profile incorporated into CARMA closely follows the size distribution determined by the model of Hunten et al. (1980), however this MSP profile is assumed to be altitude independent as introduced in the model setup by Rapp and Thomas (2006). Although the simulations are not initialized with the exact profile determined by Hunten et al. (1980), this MSP initialization will be referred to as the 'Hunten-profile'. Figure 3.4 (dashed) shows the Hunten size distribution as used in CARMA, demonstrating the extreme decrease of the MSP number density towards larger radii. This extreme decrease is also illustrated by the numbers in Tab. 3.1. This table lists the number density of MSPs which are larger than 0.5 nm, 0.8 nm, 1.0 nm, and 1.2 nm for the MSP profile of Hunten et al. (1980).

In addition to the processes included in the Hunten et al. (1980) model, the MSP model by Megner et al. (2008b) takes the meridional transport of MSPs into account. The mean meridional circulation transports the MSPs from the summer pole to the winter pole. As a consequence, the MSP number density at the summer polar mesopause is greatly reduced, as illustrated in Fig. 3.4 (solid line) and with the numbers in Tab. 3.1. Compared to the MSP profile of Hunten et al. (1980), the MSP number densities are reduced by about two orders of magnitude. The seasonal variation of atmospheric MSP content due to the meridional circulation has been verified by SOFIE observations (Hervig et al., 2009a), with a distinct minimum during the summer months.

MSP profile	Number density of MSPs [cm^{-3}] larger than			
	0.5 nm	0.8 nm	1.0 nm	1.2 nm
Hunten et al. (1980)	16300	5610	2650	1030
Megner et al. (2008b)	1750	92	15	6

Table 3.1: Number density of MSPs which are larger then 0.5 nm, 0.8 nm, 1.0 nm, and 1.2 nm, respectively. The numbers shown for the MSP profile of Megner et al. (2008b) refer to an altitude of 87 km, they increase slightly towards lower altitudes.

Most simulations will be conducted with the MSP profile of Megner et al. (2008b), because it is commonly accepted that the low MSP number densities of the Megner et al. (2008b) profile are more realistic than the significantly higher values in the profile of Hunten et al. (1980). The Hunten et al. (1980) profile will be used for conceptual studies, where an altitude independent MSP profile is preferred, or for comparisons to earlier NLC modeling studies which also used the Hunten et al. (1980) profile.

3.3 Examples of NLC simulations

The CARMA model output comprises the particle size distributions and water vapor concentration in each gridbox, as well as the atmospheric input fields (temperature, wind velocity, pressure, and density). The following Figs. 3.5 and 3.6 show all relevant parameters derived from the model output for exemplary NLC simulations.

Figure 3.5 shows the simulation results for climatological background fields. Throughout the simulation time of 48 h, the altitude range between 82 km and 91 km is supersaturated (panel a). This is the altitude range where ice particles exist. The ice particles nucleate at the temperature minimum at 87 km altitude and as they grow, they sediment to lower altitudes. The sedimentation process is comparatively slow, because the upward directed vertical wind partly compensates the sedimentation velocity. The largest mean radius is reached at about 82 km altitude (panel d), which coincides with the altitude of the maximum backscatter coefficient (panel e). Due to the evaporation of the ice particles below that altitude, a layer of increased water vapor mixing ratio can be found between 81 km and 82 km altitude (panel b), while the water vapor at higher altitudes is strongly depleted. In the climatological simulation, the ice particle number density reaches values of up to 100 cm^{-3} (panel c) and maximum radii of 60 nm (panel d). The backscatter coefficient indicates that a very bright NLC (backscatter coefficient larger than $13 \times 10^{-10}\,m^{-1}\,sr^{-1}$) develops in these background fields.

Figure 3.6 shows the simulation of NLCs in wave driven background fields, which differs from the climatological simulations in several aspects. Due to the large variability of the

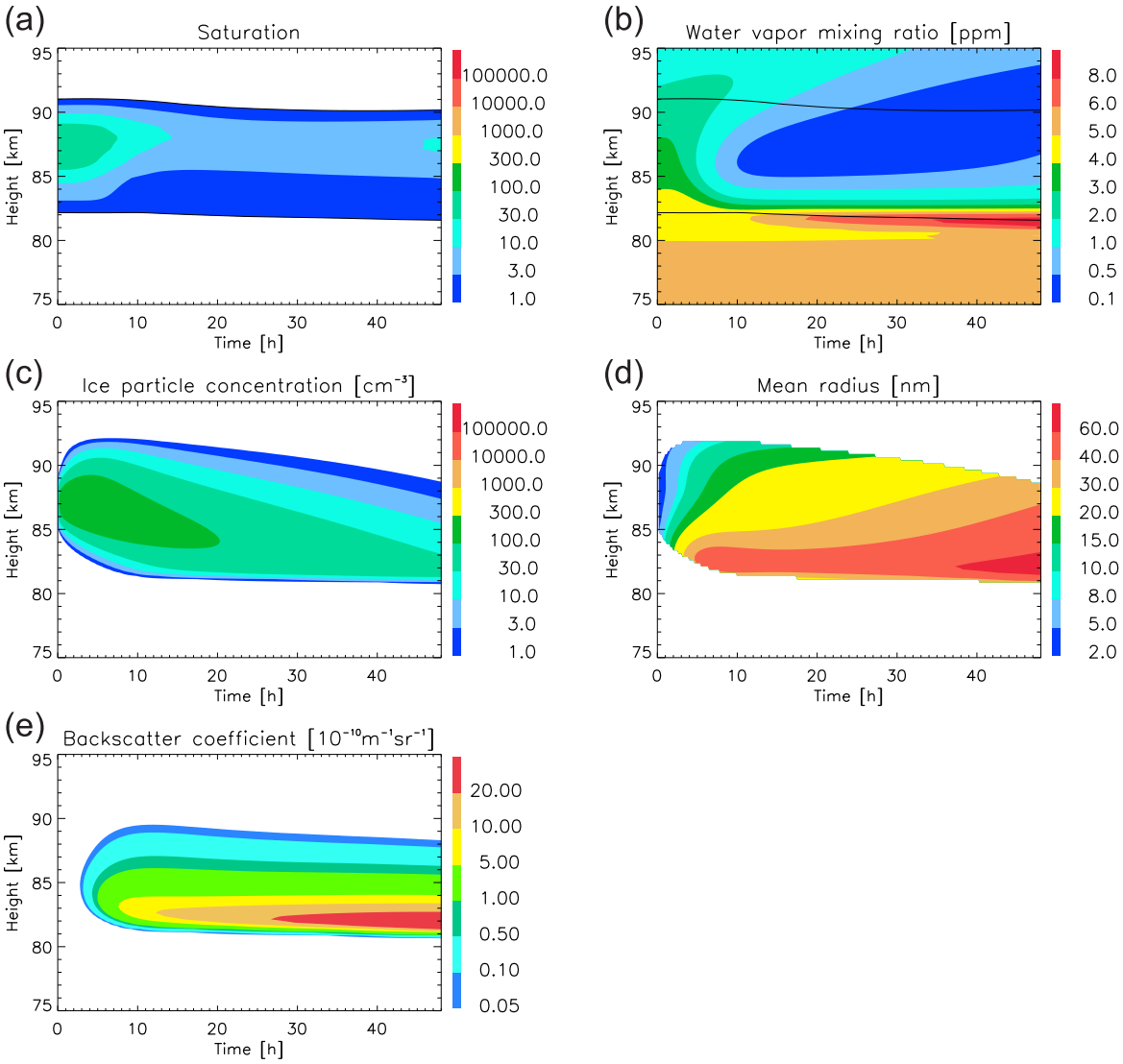

Figure 3.5: Example simulation of a NLC generated with CARMA in climatological background fields. Panel (a) shows the saturation ratio S, (b) the water vapor mixing ratio with the black line at $S = 1$, (c) the ice particle number density with (d) the corresponding mean radius and (e) the resulting backscatter coefficient at a wavelength of 532 nm. The background temperature and vertical wind fields are shown in Fig. 3.2.

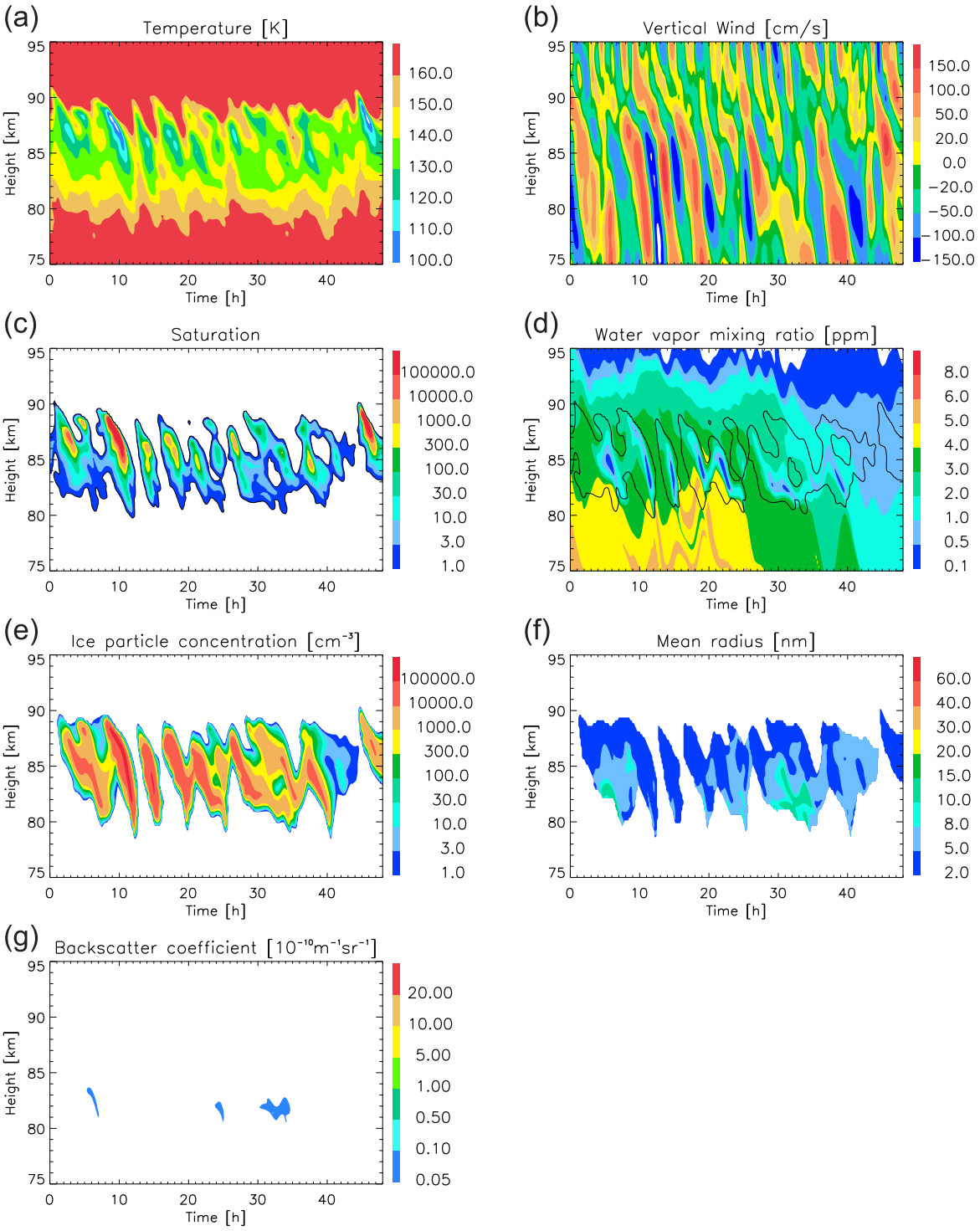

Figure 3.6: Example simulation of NLCs generated with CARMA in the wave driven background fields of the KMCM. Panel (a) shows the input fields of temperature and (b) vertical wind from KMCM. Panel (c) shows the saturation ratio S, (d) the water vapor mixing ratio with the black line at $S = 1$, (e) the ice particle number density and (f) the mean radius. Panel (e) shows the resulting backscatter coefficient at a wavelength of 532 nm.

background temperature (panel a), the supersaturated altitude range is highly variable with alternating times of supersaturation and subsaturation (panel c). Therefore, it is not possible for ice particles to grow continually for several days. Instead, ice particles nucleate during the cold phase of the waves and are then transported by the vertical wind (panel b). Note that the vertical wind reaches amplitudes as larger as $\pm 1.5\,\mathrm{m\,s^{-1}}$, whereas the climatological vertical wind is at maximum $0.05\,\mathrm{m\,s^{-1}}$. These large vertical wind velocities exceed the sedimentation velocities. Thus, sedimentation plays only a minor role in the wave driven simulations. The very low temperatures in the cold phases of the waves lead to critical radii which are smaller than in the climatological conditions. As a consequence, a much larger fraction of the MSP population can act as ice nuclei. This leads to ice number densities of up to several thousands per cubic centimeter, in extreme cases even up to hundred thousands per cubic centimeter (panel e). The particles remain comparatively small with mean radii rarely exceeding 15 nm (panel f). This affects the scattering properties of the ice particles which is reflected by the very low backscatter coefficients of less than $0.1 \times 10^{-10}\,\mathrm{m^{-1}\,sr^{-1}}$, meaning that they remain below the detection threshold of $10^{-10}\,\mathrm{m^{-1}\,sr^{-1}}$. The ice particles evaporate rapidly as soon as they fall below the supersaturated altitude range. They leave 'trails' of enhanced water vapor mixing ratio at 80 km altitude and below (panel d).

Both simulations were performed with the dust profile of Hunten et al. (1980). Simulations with lower MSP number density as in the profile of Megner et al. (2008b) lead to generally lower ice number densities and slightly larger radii. A detailed discussion of the influence of the MSP number density on NLC properties follows in Ch. 5.

3.4 Extension and simplification of the model

Tracer module

For some questions of this thesis it is helpful to trace individual ice particles, which is in principle not possible with an Eulerian transport scheme. To circumvent this limitation, a tracer module was developed, which was specifically designed for nucleation studies. The basic principle of this tracer module is the following: When the nucleation rate exceeds a certain threshold (usually 0.1 ice particles per cubic centimeter per hour), a passive tracer particle is generated. This tracer particle is then transported by the background wind and undergoes sedimentation.

The sedimentation velocity of an ice particle is radius dependent. In order to best reflect the transport of the NLC by the tracer movement, the tracer sedimentation velocity is set to be the sedimentation velocity of the radius bin with largest number density (or largest mass) at the position of the tracer. Whenever the ice particle number density falls below a threshold value (usually 0.1 ice particles per cubic centimeter), the tracer

is removed. The tracer positions are not bound to the underlying grid of CARMA, the tracers are free to take any position within a gridbox. An important feature of this module is that tracers are only generated during nucleation bursts, which allows a clear identification of the nucleation region. This is otherwise difficult since a change in ice particle number density can also be caused by advection (in particular by the divergence correction in the 1D setup).

Particle shape

Although several observations suggest that mesospheric ice particles are non-spherical (Baumgarten et al., 2002; Eremenko, 2005; Rapp et al., 2007; Hervig et al., 2009b; Kiliani et al., 2015), the CARMA model assumes spherical ice particles. The ice particle shape generally affects three parameters: the ice particle growth rate, the sedimentation velocity, and the scattering cross section. The latter is calculated in the post-processing of the data, where the particle shape can be adjusted to the desired shape. This is not possible for particle growth and sedimentation velocity, since they continually affect the development of the NLCs throughout the simulation.

The sedimentation velocity is important only in the climatological wind fields, where the ice particles' sedimentation is balanced by the vertical wind, which allows them to stay in the supersaturated region for a longer time. In the wave-driven background fields, the vertical wind velocity is much larger than the sedimentation velocity, so that sedimentation is generally of minor importance. Hence, a slight modification of the sedimentation velocity due to non-spherical ice particles can be neglected.

The growth rate is affected by the particle shape via the surface area. A non-spherical particle will always have a larger surface area compared to a volume-equivalent sphere. This results in larger growth rates for non-spherical particles. Satellite observations suggest that the dominant axis ratio (AR) of mesospheric ice particles is about 2 (Hervig et al., 2009b). A prolate ellipsoid with AR=2 has a surface area which is 7% larger than the surface area of the volume-equivalent sphere. Thus, an ice particle which has an AR=2 will grow 7% faster than a volume-equivalent spherical particle. This is a small but noticeable effect. In particular the backscatter coefficient would increase faster. However, the physical mechanism behind the non-spherical growth is currently unknown. It could be an effect of the ice crystal structure or ice particle charging. Additionally, observations suggest that the axis ratio might not be constant, but dependent on the altitude relative to the maximum brightness, dependent on the time of the season and the local ice mass density (Hervig et al., 2009b). Due to all these uncertainties concerning the axis ratio, the microphysical calculations are performed with spherical particles. Nevertheless, it is acknowledged that the ice particle radius might be underestimated.

3.5 Summary

The microphysical model CARMA is used in a setup designed for polar summer mesopause conditions. The interaction of the three model constituents – MSPs, ice particles, and water vapor – is calculated in prescribed atmospheric background fields. Nucleation, growth, coagulation, and transport (by the background wind, diffusion and sedimentation) is calculated in each time step for the one-dimensional model domain which spans the altitude range between 72 km and 102 km.

The atmospheric background is described by two different setups: either by climatological fields of temperature (Lübken, 1999) and vertical wind (Berger and Zahn, 2002) or by time resolved fields of the Kühlungsborn Mechanistic general Circulation Model (KMCM), which includes gravity waves and planetary waves. An example for NLC development in each of these fields is given in Figs. 3.5 and 3.6. In both background fields, ice particles nucleate at the altitude of minimum temperature and then grow to larger radii, while subsequently reaching lower altitudes. However, the transport mechanism to lower altitudes differs in the two setups. Sedimentation is the dominant process in the climatological fields and transport by the vertical wind is the main process in the wave driven fields.

4 Equilibrium temperature of MSPs

Parts of the results presented in this chapter have been published in Asmus et al. (2014).

MSPs are formed from the material of ablated meteoroids. Meteoroids mainly consist of iron, magnesium, silicium, and sodium. These metals form compounds (e.g. oxides, hydroxides, and carbonates) which then polymerize to nanometer-sized MSPs (Plane et al., 2015). While the composition of MSPs has still not been determined experimentally, there are indications from lab experiments and satellite observations that meteor smoke particles are believed to consist of olivine ($Mg_{1.9}Fe_{0.1}SiO_4$), hematite (Fe_2O_3), different magnesium-iron-silicates (pyroxenes, $Mg_xFe_{1-x}SiO_3$) (Saunders et al., 2010) or wuestite (FeO) and magnesiowuestite ($Mg_xFe_{1-x}O$) (Hervig et al., 2012). The influence of the chemical composition on the MSP equilibrium temperature is shown in the following.

4.1 Balance equation for MSP equilibrium temperature

MSPs are exposed to several energy sources and sinks. The balance between sources and sinks determines the equilibrium temperature of the particles. On the one hand, solar radiation P_{sol} and terrestrial radiation P_{ter} are power sources. On the other hand, infrared cooling P_{rad} and energy transfer through collisions with air molecules P_{col} are power sinks (Fiocco et al., 1975; Grams and Fiocco, 1977; Eidhammer and Havnes, 2001; Espy and Jutt, 2002). For steady state conditions, all considered contributions add up to zero, i.e.,

$$P_{\mathrm{sol}} + P_{\mathrm{ter}} - P_{\mathrm{rad}} - P_{\mathrm{col}} = 0. \tag{4.1}$$

The calculation of the radiation terms all follow the same principle: The spectral irradiance $F_\lambda(T^*)$ at the altitude of the particle is multiplied by the absorption efficiency $Q_{\mathrm{abs}}(\lambda, r, n)$ (λ wavelength, r particle radius, n refractive index) and integrated over

the complete spectral range. This quantity is then multiplied with the absorbing or emitting area of the particle, which is assumed to be spherical. The spectral irradiance is approximated by black body irradiance given by Planck's law

$$F_\lambda(T^*) = \frac{2\pi hc^2}{\lambda^5} \frac{1}{\exp\left(\frac{hc}{\lambda k_b T^*}\right) - 1}, \tag{4.2}$$

where T^* is the temperature of the black body, c is the speed of light, k_b is the Boltzmann constant, and h is the Planck constant (see also Fig. 4.2).

The power source due to solar radiation has two contributions, (1) the direct radiation from the sun and (2) the fraction of the radiation reflected by the Earth's surface with albedo A at solar zenith angle χ, which is given by $2A\cos\chi$. The solar power source can therefore be written as

$$P_{\text{sol}} = \pi r^2 \epsilon (1 + 2A\cos\chi) \int_0^\infty Q_{\text{abs}}(\lambda, r, n) F_\lambda(T_\odot) \mathrm{d}\lambda \tag{4.3}$$

where $T_\odot = 5780\,\text{K}$ is the temperature of the sun and $\epsilon = (R_\odot/R_0)^2$ is the so-called solar dilution factor with the radius of the sun $R_\odot$ and the sun-earth distance R_0.

The second term P_{ter} in the balance equation describes the particle heating due to infrared radiation and is defined as

$$P_{\text{ter}} = \pi r^2 \int_0^\infty Q_{\text{abs}}(\lambda, r, n) F_\lambda(T_{\text{E}}) \mathrm{d}\lambda \tag{4.4}$$

The temperature T_{E} is assumed to be the temperature of the stratopause with 280 K. The dilution factor for this term is neglected, since the particle resides in close proximity to the surface of the earth (compared to the radius of the earth).

The particle itself emits radiation corresponding to its surface temperature T_{P}. This power loss $P_{\text{rad}}(T_{\text{P}})$ is described by

$$P_{\text{rad}}(T_{\text{P}}) = 4\pi r^2 \int_0^\infty Q_{\text{abs}}(\lambda, r, n) F_\lambda(T_{\text{P}}) \mathrm{d}\lambda. \tag{4.5}$$

Thereby, it is assumed that the particle radiates homogeneously in all directions.

The collisions between the MSPs and the ambient atmosphere result in a power loss term if the surrounding air is cooler than the MSPs (or an heating term if the air is warmer). In the free molecular flow regime, the energy transfer through collisions generally depends on the thermal velocity v_{therm} and number density n_{gas} of the surrounding gas, the thermal accommodation coefficient α_{therm}, the specific heat ratio of the gas γ, and

the gas flow velocity relative to the particle motion. It is reasonable to assume that the particle moves with the background wind and that the sedimentation velocity is small compared to the vertical wind velocity, so that the relative motion between particle and gas can be neglected. With this assumption, the equation for the collisional heat transfer from the particle to the gas as given by Gombosi (1994) and multiplied by the surface area simplifies to

$$P_{\mathrm{col}}(T_{\mathrm{P}}) = 4\pi r^2 \alpha_{\mathrm{therm}} \frac{n_{\mathrm{gas}} v_{\mathrm{therm}}}{4} k_b \frac{\gamma+1}{2(\gamma-1)} (T_{\mathrm{P}} - T_{\mathrm{A}}). \tag{4.6}$$

The equilibrium temperature can now be derived from the thermal balance equation 4.1. The power contributions of $P_{\mathrm{rad}}(T_{\mathrm{P}})$ and $P_{\mathrm{col}}(T_{\mathrm{P}})$ both depend on the particle temperature T_{P}. However, $P_{\mathrm{rad}}(T_{\mathrm{P}})$ is a nontrivial function of T_{P} so that a closed expression for the equilibrium temperature cannot be found. Instead, an iterative scheme is applied where the particle temperature of the previous step $i-1$ is used in the term of $P_{\mathrm{rad}}(T_{\mathrm{P}}^{i-1})$ to calculate T_{P}^{i} in the following manner:

$$T_{\mathrm{P}}^{i} = T_{\mathrm{A}} + \frac{P_{\mathrm{sol}} + P_{\mathrm{ter}} - P_{\mathrm{rad}}(T_{\mathrm{P}}^{i-1})}{\alpha_{\mathrm{therm}} \pi r^2 n_{\mathrm{gas}} k_b v_{\mathrm{therm}} \frac{\gamma+1}{2(\gamma-1)}}. \tag{4.7}$$

In the initial step the particle temperature is set equal to the ambient atmospheric temperature ($T_{\mathrm{P}}^{0} = T_{\mathrm{A}}$). The iteration is terminated when the difference $\left| T_{\mathrm{P}}^{i} - T_{\mathrm{P}}^{i-1} \right|$ falls below the threshold of $10^{-3}\,\mathrm{K}$.

For the following calculations of the equilibrium temperature T_{P}, the thermal accommodation coefficient is set to $\alpha_{\mathrm{therm}} = 0.5$, the albedo to $A = 0.3$, and the solar zenith angle to $\chi = 52°$.

4.2 Optical properties of MSPs

The absorption efficiency $Q_{\mathrm{abs}}(\lambda, r, n)$ is calculated using Mie theory (Bohren and Huffman, 1983) by evaluating the difference between extinction efficiency and scattering efficiency

$$Q_{\mathrm{abs}} = Q_{\mathrm{ext}} - Q_{\mathrm{sca}}. \tag{4.8}$$

The question whether the optical properties of the bulk material can be applied to systems in the size of a few nanometers has been studied experimentally by Meinen et al. (2012). They find good agreement between the measured extinction cross section of hematite (Fe_2O_3) and the corresponding Mie calculations for particle sizes down to 1.5 nm radius.

Figure 4.1 shows the absorption efficiency for all MSP materials analyzed in the following. The selection is based on the materials included in the study of Hervig et al.

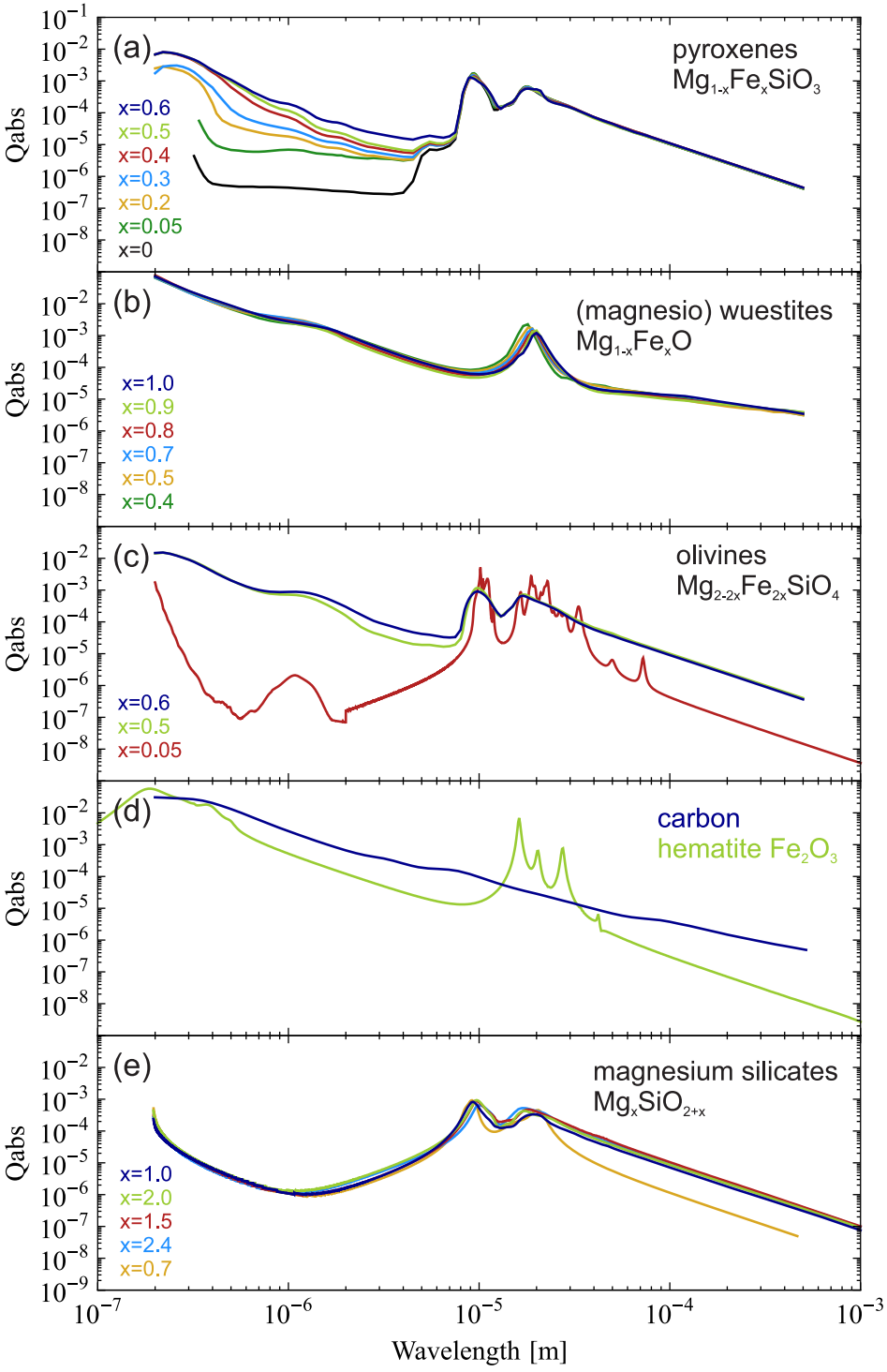

Figure 4.1: Absorption efficiencies of a 1 nm particle composed of (a) pyroxenes, (b) (magnesio-)wuestites, (c) olivines, (d) carbon and hematite, and (e) magnesium silicates.

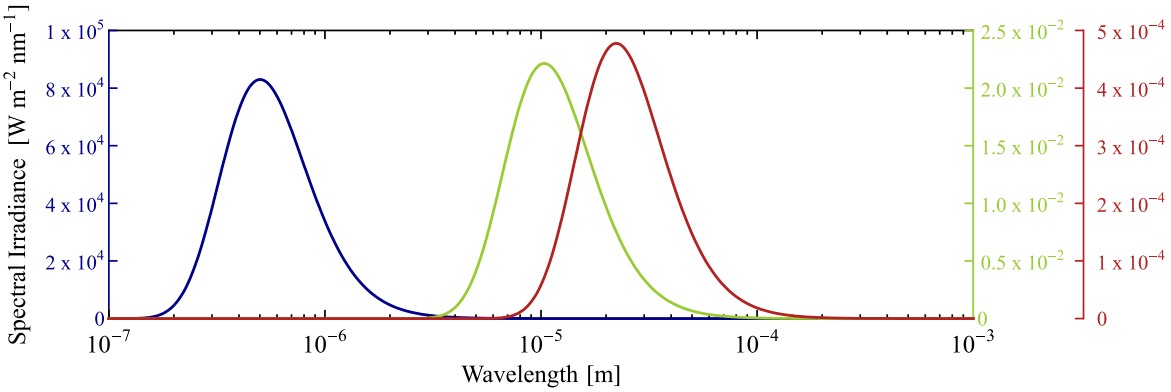

Figure 4.2: Black body spectrum for $T = 5780\,\mathrm{K}$ (blue), $T = 280\,\mathrm{K}$ (green) and $T = 130\,\mathrm{K}$ (red), with the individual scale indicated by the corresponding color.

(2012). Further information on these materials, like reference for the refractive indices or the phase, are included in Tab. 4.1. For comparisons and to facilitate the discussion of the absorption efficiencies, the black body spectrum $F_\lambda(T_\odot)$ for the temperature of the sun is shown in Fig. 4.2, along with $F_\lambda(T_\mathrm{E})$ and the black body spectrum for $T = 130\,\mathrm{K}$.

Panel (a) of Fig. 4.1 shows Q_abs for pyroxenes ($\mathrm{Fe}_x\mathrm{Mg}_{1-x}\mathrm{SiO}_3$), with different relative iron contents x. Between the wavelengths of 200 nm and 7 µm the absorption efficiency increases strongly with increasing iron content. Since the differences occur in the wavelength range of the solar spectrum, the absorption of solar radiation will be largely dependent on the iron content of the pyroxenes. Consequently, it is expected that the equilibrium temperature of MSPs composed of pyroxenes will depend on the relative iron content.

Panel (b) shows the absorption efficiency for (magnesio-)wuestite, again for different iron contents x. Interestingly, the difference between the individual curves is not as distinct as for the pyroxenes, although the iron content varies over the same range of relative iron contents. For all (magnesio-)wuestite compositions, the absorption efficiency in the visible is about one order of magnitude larger than for the pyroxene composition with the largest absorption efficiency. The increase of Q_abs towards smaller wavelengths is due to the characteristic $1/\lambda$ dependency in the small-sphere approximation of Q_abs (Bohren and Huffman, 1983).

Panel (c) shows Q_abs for different olivine compositions. The pronounced difference of the red curve compared to the other two curves is not only due to the significantly lower iron content, but also due to the different phases ($x = 0.05$: crystalline; $x = 0.5$ and $x = 0.6$: glassy, see Tab. 4.1).

The absorption efficiencies of carbon and hematite are shown in panel (d). Carbon has no characteristic absorption peaks, because the refractive index of carbon is almost

constant in the here considered spectral range. The spectral dependence is therefore mainly determined by the $1/\lambda$ dependency. The spectral dependence of Q_{abs} for hematite is similar to the spectral dependence of Q_{abs} for (magnesio-)wuestite, with enhanced absorption between 10 µm and 30 µm, although hematite has more distinct peaks. In the visible, the absorption of hematite is roughly one order of magnitude lower than for (magnesio-)wuestite. Hence, it is expected that the equilibrium temperature of hematite particles is lower than the equilibrium temperature of (magnesio-)wuestite particles.

Magnesium silicates, shown in panel (e), have the lowest absorption efficiency from the here shown materials, especially in the visible wavelength range. The equilibrium temperature of magnesium silicate particles is therefore expected to be comparatively low, since the contribution of P_{sol} to the balance equation is almost negligible.

4.3 Equilibrium temperature

Figure 4.3 shows the temperature difference ΔT between the equilibrium temperature T_{P} and the temperature of the background atmosphere T_{A} as a function of particle radius and altitude. The background temperature T_{A} is taken from the climatology by Lübken (1999) for July conditions at 69° N (see Fig. 3.2). The temperature difference generally increases with altitude and radius. The only altitude dependent contribution to the balance equation is the collisional loss term P_{col}, which decreases with altitude due to the decreasing air density (the temperature decrease is of minor importance). The radius dependence of ΔT is also due to the collision term, which scales with the particle surface, while the radiative terms scale with the particle volume. Thus, particles at higher altitudes and with larger radii are dominated by radiative heating, because the collisional cooling is comparatively inefficient.

The temperature difference ΔT for the two pyroxene compositions in Fig. 4.3 illustrates that the iron content has a large influence on the equilibrium temperature. The left panel shows ΔT for MSPs composed of $Fe_{0.6}Mg_{0.4}SiO_3$ and the right panel for MSPs composed of $MgSiO_3$. The difference between the two panels is only due to the different relative iron contents. For example, a 1.1 nm MSP at 87 km altitude has a ΔT of 2.1 K if the relative iron content is $x = 0.6$, and a ΔT of 0.1 K if the relative iron content $x = 0$.

An overview over typical values of ΔT for a 1.1 nm MSP at 87 km altitude is given in Tab. 4.1 for various MSP compositions. The table is sorted by ΔT in decreasing order. Within each group of chemical compositions, the equilibrium temperature decreases with decreasing iron content. This indicates that the tendency shown above in Fig. 4.3 for pyroxene particles also holds for other iron containing particles. Furthermore,

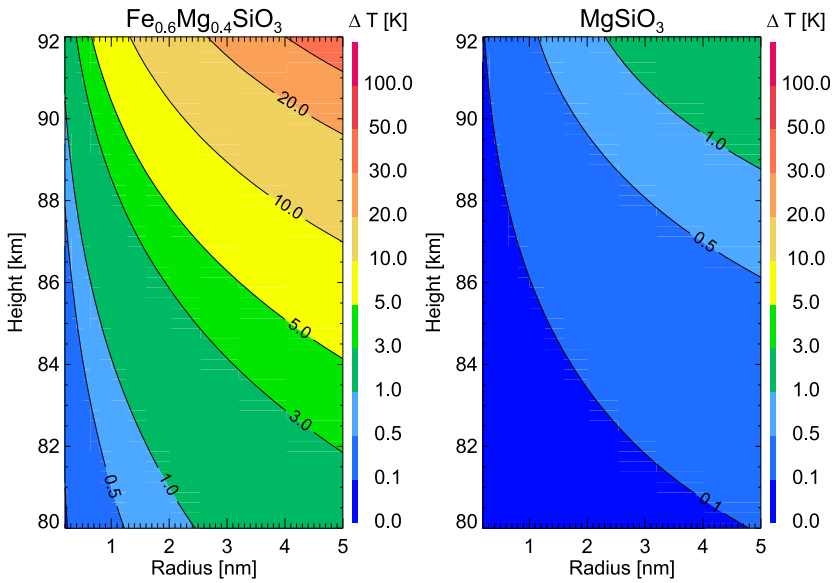

Figure 4.3: Temperature difference ΔT between equilibrium temperature and background temperature for a MSP composed of pyroxene $Fe_xMg_{1-x}SiO_3$ with (left) $x = 0.6$ and (right) $x = 0$. This figure is reproduced from Asmus et al. (2014) for different MSP materials.

the lowest equilibrium temperatures are obtained for the iron-free magnesium silicate particles.

The equilibrium temperature has so far been determined from steady state conditions. The explicit time dependence of T_P can be solved for a given heat capacity c_P and particle density ρ_MSP. In a first order approximation the characteristic time constant τ is given by (see Appendix A.2)

$$\tau = \frac{8 r \rho_\mathrm{MSP} c_\mathrm{P} (\gamma - 1)}{3 \alpha_\mathrm{therm} n_\mathrm{gas} v_\mathrm{therm} k_b (\gamma + 1)}. \tag{4.9}$$

Figure 4.4 shows the evolution of T_P for a 1.1 nm particle composed of FeO which has a background temperature T_A and is then exposed to the power sources and sinks listed above. The specific heat capacity of FeO is $c_\mathrm{P} = 476\,\mathrm{J\,kg^{-1}\,K^{-1}}$ at 130 K (Stølen et al., 1996). The particle approaches its equilibrium temperature with a characteristic time constant of 2.5×10^{-3} s, thus, the equilibrium temperature is reached within less than 10^{-2} s. This means that the equilibrium temperature adopts almost instantaneously to variations of the background temperature or to variations of the power terms (e.g. due to changing solar zenith angles during the course of a day).

MSP composition	phase	ΔT[K]	reference
Carbon			
C	(a)	18.0	Jäger et al. (1998)
(Magnesio-) Wuestite			
FeO	(?)	14.4	Henning et al. (1995)
$Mg_{0.1}Fe_{0.9}O$	(c)	13.8	—″—
$Mg_{0.2}Fe_{0.8}O$	(c)	14.2	—″—
$Mg_{0.3}Fe_{0.7}O$	(c)	13.6	—″—
$Mg_{0.5}Fe_{0.5}O$	(c)	13.2	—″—
$Mg_{0.6}Fe_{0.4}O$	(c)	12.2	—″—
Hematite			
Fe_2O_3	(?)	9.6	AIU Jena (2016)
Olivine			
$Mg_{0.8}Fe_{1.2}SiO_4$	(g)	4.1	Dorschner et al. (1995)
$MgFeSiO_4$	(g)	4.1	—″—
$Mg_{1.9}Fe_{0.1}SiO_4$	(c)	0.2	Fabian et al. (2001)
Pyroxene			
$Mg_{0.4}Fe_{0.6}SiO_3$	(g)	2.1	Dorschner et al. (1995)
$Mg_{0.5}Fe_{0.5}SiO_3$	(g)	1.9	—″—
$Mg_{0.6}Fe_{0.4}SiO_3$	(g)	1.6	—″—
$Mg_{0.7}Fe_{0.3}SiO_3$	(g)	0.7	—″—
$Mg_{0.8}Fe_{0.2}SiO_3$	(g)	0.5	—″—
$Mg_{0.95}Fe_{0.05}SiO_3$	(g)	0.2	—″—
$MgSiO_3$	(g)	0.1	—″—
Magnesium Silicate			
$Mg_{1.5}SiO_{3.5}$	(a)	0.11	Jäger et al. (2003)
Mg_2SiO_4	(a)	0.11	—″—
$Mg_{2.4}SiO_{4.4}$	(a)	0.10	—″—
$MgSiO_3$	(a)	0.08	—″—
$Mg_{0.7}SiO_{2.7}$	(a)	0.08	—″—

Table 4.1: Temperature difference between a 1.1 nm MSP and the ambient atmosphere at 87 km altitude for different MSP compositions. The temperature of the ambient atmosphere is assumed to be 130 K. The phase of the materials is listed in the second column (a: amorphous, c: crystalline, g: glassy, ?: unknown) and the reference for the refractive indices is listed in the last column.

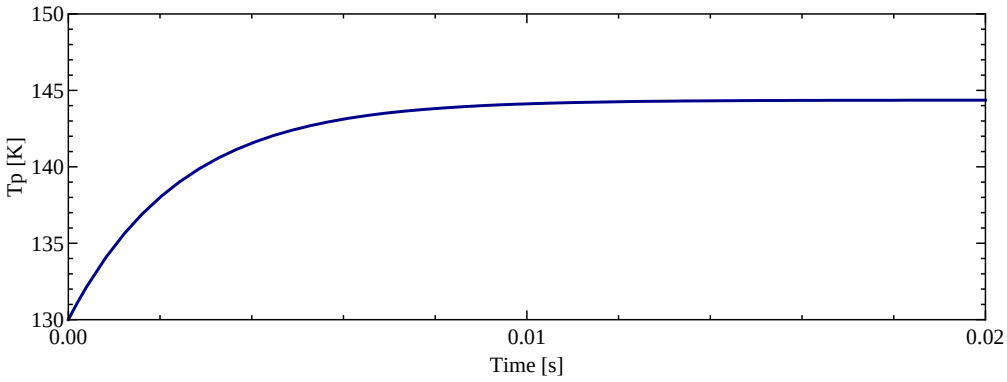

Figure 4.4: Time evolution of the MSP equilibrium temperature T_P for a 1.1 nm particle composed of FeO (background atmosphere 130 K, 87 km altitude).

4.4 Implication for ice microphysics

A minimal increase of the MSP temperature compared to the ambient air temperature leads to a vast reduction of the nucleation rate (see Sec. 2.1.4 and Fig. 2.9). However, not only the magnitude of the nucleation rate is reduced, but also the critical radius is shifted to larger values (see Eq. 2.34 and Fig. 2.8). As a consequence, fewer MSPs are available as ice nuclei because the MSP size distribution decays exponentially with radius (see Fig.3.4). Thus, for the iron rich materials presented in Tab. 4.1, nucleation becomes almost impossible. A similar conclusion was already stated by Witt (1968), who mentioned that MSPs composed of iron should be poor ice nuclei. His arguments were based on the same physical mechanisms, namely that iron (or in general conducting materials) are highly absorbing in the visible wavelength range bur poorly emissive in the infrared.

In the following, the effect of heated ice nuclei on NLC properties is demonstrated with simplified CARMA simulations. For these simulations, a temperature difference between MSPs and the ambient atmosphere is assumed, which varies with altitude but does not depend on the radius of the MSPs. The altitude dependence is calculated for a 2 nm particle composed of pyroxene (see red line in Fig. 4.5) and scaled in a way that the temperature difference ΔT at 87 km altitude is 1 K, 3 K, 5 K, and 7 K (gray lines). In order to clearly demonstrate the effect of ΔT, the climatological background profiles are chosen in these simulations, so that no further variability of the nucleation rate is induced by changing background temperatures. The ice number densities resulting from these simulations are show in Fig. 4.6 and the ice particle radii in Fig. 4.7.

The temperature difference ΔT has a striking effect on the ice particle number density. While the reference case $\Delta T = 0$ K leads to ice particle number densities of more than

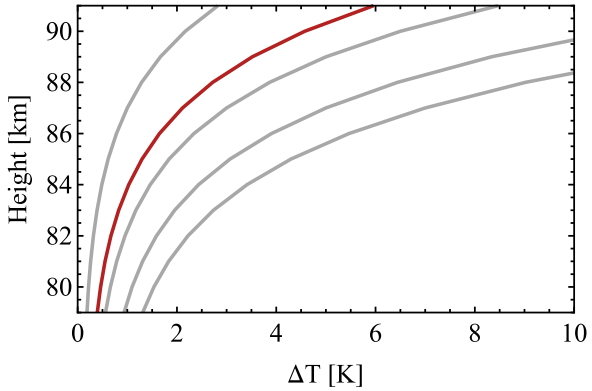

Figure 4.5: Profile of ΔT used for the CARMA simulations. The red line shows the altitude dependence of ΔT of a 2 nm MSP composed of $Fe_{0.5}Mg_{0.5}SiO_3$. This profile is scaled so that ΔT at 87 km altitude is 1 K, 3 K, 5 K, and 7 K (gray lines).

100 cm^{-3}, an increase of the MSP temperature by 5 K results in ice number densities of only 1 cm^{-3} and an increase of 7 K results in less than 0.1 cm^{-3}. Not only the ice number density changes with ΔT, but also the ice particle radii: In the reference case, the ice particle growth is limited by the available water vapor. The relatively large number of ice particles in the reference case rapidly depletes the available water vapor (see also Fig. 3.5b), which leads to freeze drying of the mesopause region. In the $\Delta T = 7$ K simulation, the few ice particles cannot deplete the available water vapor. Thus, the ice particles experience maximum growth rates which lead to very large ice particle radii. As seen in Fig. 4.7, it takes almost two days in the reference simulation until the ice particles reach radii larger than 50 nm, while it takes less than one day in the simulation with $\Delta T = 7$ K to reach the same size.

4.5 Discussion

The equilibrium temperature of MSPs has been calculated for daylight conditions with constant solar zenith angle $\chi = 52°$. In reality, χ varies with local time and with season, which influences the equilibrium temperature. To demonstrate the effect of the diurnal variation of χ, Fig. 4.8 shows ΔT for a FeO particle as a function of local time. The daily variation of ΔT is about 4 K. The colors refer to different dates throughout the NLC season from 15. June to 1. August and show that the seasonal variation is small compared to the diurnal variation. The variability of ΔT shown in Fig. 4.8 is based only on the variation of χ. Further variability due to changing background temperatures during the NLC season (see Fig. 3.2a) are on the order of less than 0.05 K.

The diurnal variation of the MSP equilibrium temperature is most pronounced for MSP materials which are highly absorbing in the visible wavelength range, like (magnesio-)

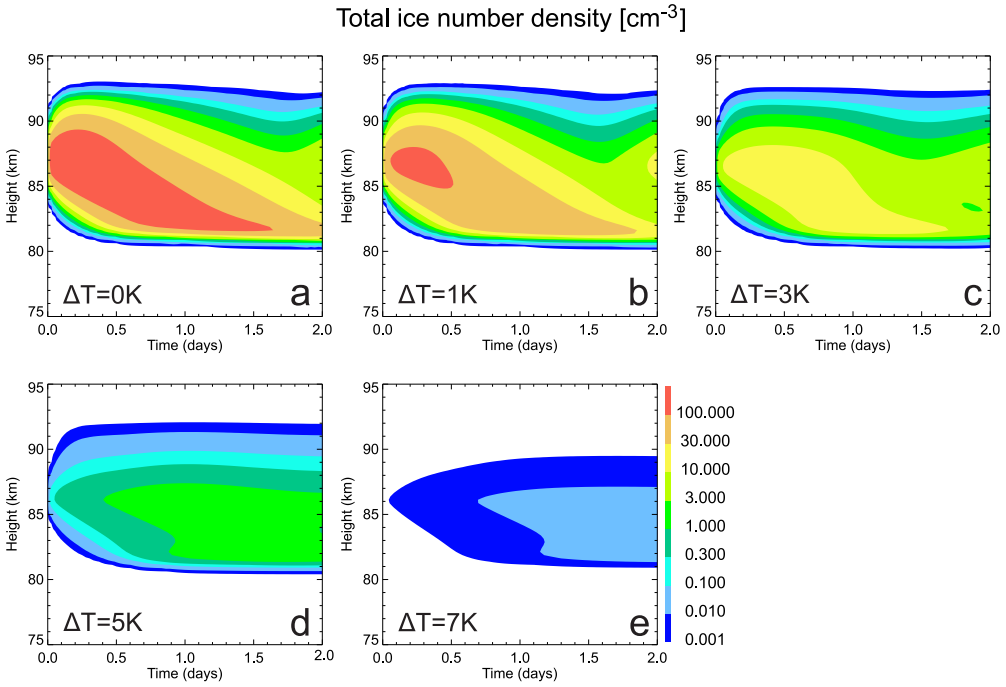

Figure 4.6: Ice number densities with varying temperature differences between MSPs and the ambient atmosphere. ΔT refers to the temperature difference at 87 km altitude. This figure is reproduced from Asmus et al. (2014).

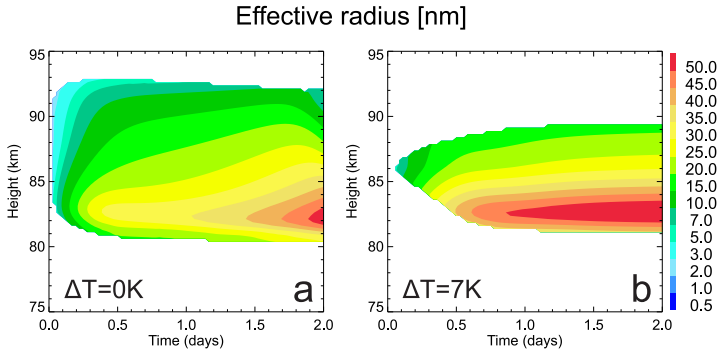

Figure 4.7: Effective radius of ice particles for the reference case with $\Delta T = 0\,\mathrm{K}$ and $\Delta T = 7\,\mathrm{K}$. The temperature difference refers to the altitude of 87 km. This figure is reproduced from Asmus et al. (2014).

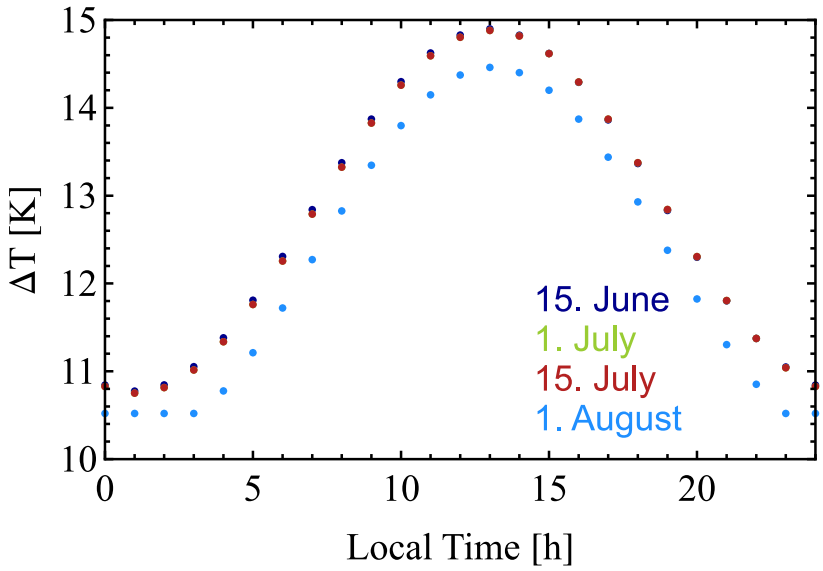

Figure 4.8: Temperature difference between the equilibrium temperature of 1.1 nm sized MSP composed of FeO and the temperature of the ambient atmosphere (130 K) as a function of local time. The different colors refer to different dates in the NLC season.

wuestites and hematite. Therefore, the diurnal variation shown in Fig. 4.8 for FeO is an upper limit. The diurnal variation of ΔT leads to varying nucleation rates throughout the day. A nucleation event occurring around noon at low solar zenith angles results in lower ice number densities than the same event at higher zenith angles. This does not mean, that the ice number density is generally controlled by the solar zenith angle, but the χ dependence of the nucleation rate might contribute to the diurnal variation of NLCs (see for example Fiedler et al. 2005).

During nighttime, the solar power term P_{sol} is zero. However, since NLCs are a polar summer phenomenon, the sun does not set at mesospheric altitudes during the NLC season. At 69°N and 87 km altitude, the last sunset occurs two months before solstice and then again two months after solstice[1]. Thus, the case where $P_{\mathrm{sol}} = 0$ is not relevant for the nucleation of mesospheric ice particles.

Assuming a black body spectrum for the solar radiation term P_{sol} and for the terrestrial radiation term P_{ter} simplifies the calculation of T_{P}, but also introduces errors to T_{P}. This issue has been addressed in Asmus et al. (2014) by evaluating the equilibrium temperature of ice particles. The equilibrium temperature of ice particles is in particular sensitive to differences in the terrestrial radiation spectrum $F_\lambda(T_{\mathrm{E}})$, since ice

[1] Calculated with NASA Solar Systems Dynamics: HORIZONS Web interface (`http://ssd.jpl.nasa.gov/horizons.cgi`) for 69°N. Sunset at 87 km altitude is assumed when the apparent solar elevation angle is below $10° = \arccos\left[R_{\mathrm{earth}}/(R_{\mathrm{earth}} + 87\,\mathrm{km})\right]$.

is transparent at wavelengths in the visible and mainly absorbing in the infrared. The equilibrium temperature of ice particles has previously been calculated by Espy and Jutt (2002), who used the same terms for the balance equation (Eq. 4.1), but integrated the spectra from the radiative transfer model MODTRAN. Asmus et al. (2014) compared the equilibrium temperature obtained with the simplified black body model to the equilibrium temperature obtained from the model with the MODTRAN spectra. They find (their Fig. 1) that the difference between both models is small. E.g., the difference between both models is less than 0.1 K for a 50 nm ice particle at 88 km altitude. For larger ice particles, the absolute difference between the two models increases, but because also ΔT increases for larger particle, the relative error remains small. For 50 nm ice particles, the relative difference between the two models is less than 3%, thus justifying the black body simplification for the current purpose.

The largest uncertainty of the equilibrium temperature is induced by the uncertainty of the thermal accommodation coefficient α_{therm}. Since ΔT depends linearly on α_{therm} in a first order approximation, any relative uncertainty of α_{therm} directly contributes to the relative uncertainty of ΔT. The chosen value of $\alpha_{\text{therm}} = 0.5$ is based on previous studies evaluating the equilibrium temperature of particles in the mesosphere (e.g., Grams and Fiocco, 1977; Espy and Jutt, 2002). Grams and Fiocco (1977) mention in their discussion that values of $\alpha_{\text{therm}} < 0.1$ and up to unity have been observed for a variety of gases and particles. However, no measurements are available which are directly applicable for MSPs in the mesosphere (to the best of our knowledge). An indication that α_{therm} might be larger than 0.5 comes from simulations of the gas flow around sounding rockets in the mesosphere, which achieve good results with $\alpha_{\text{therm}} = 1$ (Bird, 1988; Gumbel, 2001). If MSPs behave in this aspect similar to the technical surfaces of sounding rockets and MSPs are adequately described by $\alpha_{\text{therm}} = 1$, the cooling would be twice as efficient as assumed in this study and the temperature differences would be reduced by 50%.

The CARMA simulations presented in Fig. 4.6 and 4.7 reinforce the hypothesis of this thesis, namely that heated MSPs are poor ice nuclei. The extreme reduction of the ice number densities for larger values of ΔT is purely due to the higher equilibrium temperature of the MSPs. The lower ice number densities lead to NLCs with drastically reduced ice density and backscatter coefficient. For example, the backscatter coefficient of the NLC in the $\Delta T = 7\,\text{K}$ simulation is 4 orders of magnitude lower than in the reference simulation with $\Delta T = 0\,\text{K}$, and hence below the detection threshold of all optical instruments. Even though the backscatter coefficient scales with the ice particle radius to the power of six in the visible (Rayleigh scattering), the increased radius in the $\Delta T = 7\,\text{K}$ simulation cannot compensate the extreme reduction of the ice number density caused by the warmer ice nuclei.

4.6 Summary

Based on current assumptions, MSPs are presumably composed of materials which have large absorption efficiencies in the visible wavelength range, which leads to an increased equilibrium temperature of MSPs. The equilibrium temperature is determined by the balance of power sources, which are solar and terrestrial radiation, and power sinks, which are infrared cooling and collisions with ambient gas molecules. The temperature difference between MSPs and the ambient atmosphere $\Delta T = T_{\mathrm{P}} - T_{\mathrm{A}}$ generally increases with altitude and particle radius, and strongly depends on the composition of the MSPs. Highly absorbing materials such as (magnesio-)wuestites lead to a MSP equilibrium temperature at mesopause heights which is 14 K higher than the temperature of the ambient atmosphere. On the contrary, MSPs composed of low absorbing materials such as magnesium-silicates acquire an equilibrium temperature just slightly above the ambient gas temperature with $\Delta T = 0.1\,\mathrm{K}$. Within each group of materials (e.g., pyroxenes, (magnesio-)wuestites, etc.), ΔT increases with increasing relative iron content. The characteristic time constant for reaching the equilibrium temperature is on the order of $10^{-3}\,\mathrm{s}$, which means that the MSP temperature adopts almost instantaneously to changing power sources or sinks.

The temperature difference between MSPs and the ambient atmosphere has a striking effect on the resulting ice number densities. CARMA simulations with a typical profile of ΔT showed that the ice number density is dramatically reduced when MSPs are slightly heated. A ΔT of 5 K (7 K) leads to ice number densities which are less than 3% (0.01%) of the ice number densities obtained in the reference simulation with $\Delta T = 0\,\mathrm{K}$. Although the ice particle radii are larger when fewer ice particles are present, the ice density and NLC brightness remains small and impedes the detection of those NLCs with optical instruments.

Due to the diurnal variation of the solar zenith angle, the equilibrium temperature of MSPs has a diurnal variation as well. It is possible, that the resulting variation of the nucleation rate contributes to the observed diurnal cycle of NLC properties.

5 Sensitivity of NLC properties to the nucleation rate

Parts of the results presented in this chapter have been published in Wilms et al. (2016).

Several of the parameters which determine the nucleation rate are highly uncertain, as discussed in Sec. 2.1.4. Additionally, the temperature difference between MSP and background atmosphere modifies the nucleation rate. This leads to uncertainties in the nucleation rate of several orders of magnitude. In the following, the effects of uncertainties in the nucleation rate are studied systematically. First, the mean properties of NLCs modeled in a reference setup are presented, then the nucleation rate is varied over a wide range and the resulting NLC properties are compared to observations. The observations included in the comparison are the following: Lidar observations from ALOMAR (Arctic Lidar Observatory for Middle Atmosphere Research) at 69° N, 16° E, observations from the Solar Occultation For Ice Experiment (SOFIE) on the AIM (Aeronomy of Ice in the Mesosphere) satellite, and observations from the Optical Spectrograph and InfraRed Imager System (OSIRIS) on the Odin satellite.

5.1 Mean properties of modeled NLCs

The mean properties of NLCs modelled with the wave driven KMCM background profiles are depicted in Figure 5.1. Panel (a) shows the mean ice particle number density and panel (b) the mean radius. The mean number density is roughly constant over the altitude range from 81 km to 88 km with 200 cm^{-3} to 300 cm^{-3} (dashed line). Limiting the modeled NLCs to those which would be detectable by SOFIE (extinction coefficient greater than $2 \times 10^{-7}\,\mathrm{km}^{-1}$ at 3.064 µm, Hervig et al., 2009c), an altitude profile is obtained (solid line), where the number density strongly increases with altitude. This is in reasonable agreement with observational results from SOFIE (Bardeen et al., 2010) and the Odin satellite (Hultgren and Gumbel, 2014). The difference can be explained by the corresponding profile of the mean particle size, with small particles at high altitudes and larger ones below. As the optical signal is extremely sensitive to the particle radius (scaling with power laws between r^6 and r^3 depending on observation wavelength), high clouds with small particles can only be detected if they have large

number densities. Therefore, the applied SOFIE detection limit induces a bias towards larger number densities at higher altitudes. The time averaged particle radius reaches its maximum value of about 15 nm at 82 km. Compared to particles sizes retrieved from observations (e.g., Hervig et al., 2009b; Hultgren and Gumbel, 2014; Baumgarten et al., 2008), these particles remain comparatively small.

5.2 Setup of sensitivity experiments

There are different parameters that lead to uncertainties in the nucleation rate. One way of studying the effect of these uncertainties would be by varying each parameter within its uncertainty range. Besides the lack of knowledge concerning the uncertainty range of each individual parameter, this approach would lead to an almost endless number of simulations. To circumvent this problem, the effects of uncertainties are classified into two groups. The two parameters which are important for the overall development of NLCs are (1) the general order of magnitude of the nucleation rate per particle J/N_N and (2) the number of ice nuclei N_N. The first parameter determines the time constant of the nucleation process, while the second parameter determines the maximum number of ice particles which are generated.

The uncertainty of the order of magnitude of J is mainly determined by the uncertainty of the desorption energy ΔF_des. The desorption energy enters the equation of the nucleation rate in the exponential term and has a positive sign (see Eq. 2.33). This means that increasing ΔF_des simply increases J for a given radius and temperature and vice versa for decreasing ΔF_des. In other words, the variation of ΔF_des acts as a scaling factor, i.e. a prefactor to the nucleation rate. In the following simulations, this prefactor is varied over ± 10 orders of magnitude. This range is not based on the specific uncertainty of ΔF_des, but it rather covers the relevant range where an influence of the prefactor is observed in the simulations. To be completely consistent with Eq. 2.33, the prefactor should be temperature dependent. This temperature dependence is neglected because the onset of nucleation is expected to occur always around the same temperature (J/N_N increases by more than 5 orders of magnitude between 131 K and 130 K, see Fig. 2.7b).

The uncertainty of the number density of available ice nuclei N_N is determined by the uncertainty of the critical radius r^* and the MSP size distribution. The uncertainty of r^* is predominantly determined by the uncertainty of the surface tension σ. However, the variation of r^* via the surface tension also effects the nucleation barrier $\Delta F^* \propto \sigma r^{*2}$ (see Eq. 2.9) and therefore the order of magnitude of J/N_N. Thus, varying the nucleation rate via the surface tension will have the effect that the individual influence of either shifting r^* or varying the order of magnitude of J/N_N cannot be separated from each other. For this reason, the uncertainty of the second parameter, the number of available

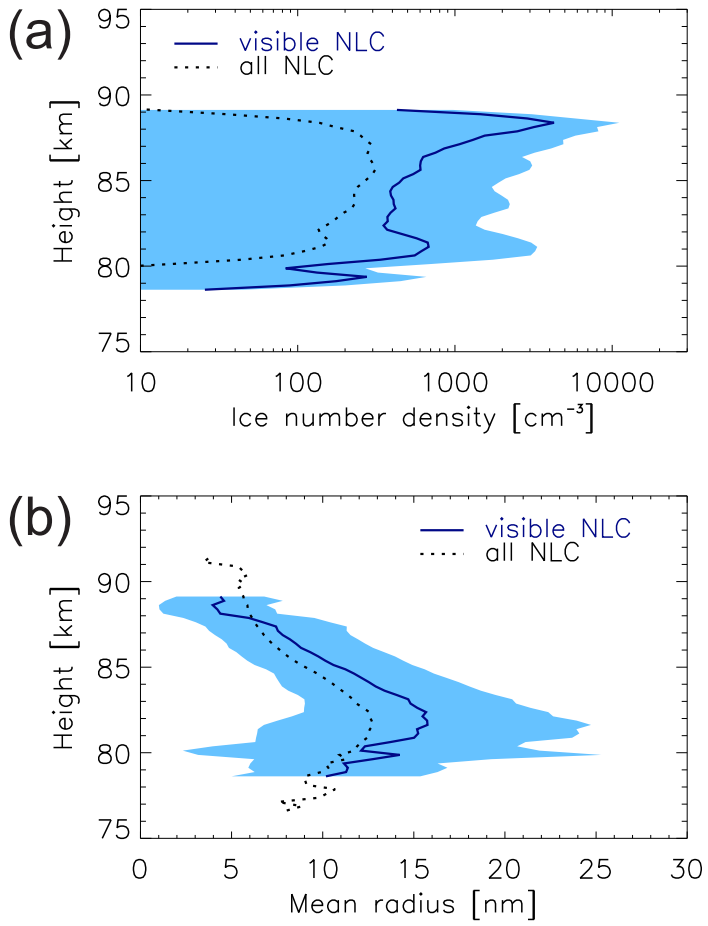

Figure 5.1: Mean properties of simulated NLC: (a) ice particle number density and (b) mean radius. The dashed line includes all simulated NLC and the solid line only those visible to SOFIE. The shaded area corresponds to one standard deviation of the visible NLC. The wave driven simulations with reference nucleation rate and the MSP profile of Megner et al. (2008b) have been averaged for these plots. This figure is reproduced from Wilms et al. (2016).

ice nuclei, is studied by varying the number of MSPs. These simulations are set up with MSP profiles scaled with various factors, but it should be kept in mind that they are intended to also illustrate the uncertainty of the critical radius, e.g. caused by the poorly known surface tension.

With this approach the effect of both parameters, the order of magnitude of J/N_N and the number of ice nuclei N_N, can be clearly distinguished. For the following simulations, the CARMA model is set up with either climatological or wave driven background profiles and with the MSP profile of either Hunten et al. (1980) or Megner et al. (2008b). The nucleation rate is systematically modified with a prefactor which ranges from 10^{-10} to 10^{10} with 4 values per decade. The MSP profile is multiplied by the factors of 100, 10, 0.1, 0.01, and 0.001. In further sensitivity simulations, a constant temperature offset is added to the temperature profile and the vertical wind velocity is decreased.

5.3 NLC properties as function of nucleation rate

A first illustration of the influence of the nucleation rate on NLC properties is given in Fig. 5.2. Panel (a) presents NLCs which develop in the climatological background with standard nucleation rate (top) and with a nucleation rate reduced by three orders of magnitude (bottom). Panel (b) presents NLCs which develop in the wave driven background, also for the standard nucleation rate (top) and for a nucleation rate reduced by five orders of magnitude (bottom). In both cases the particles grow to significantly larger radii if the nucleation rate is reduced. The maximum backscatter coefficient at 532 nm is increased by more than a factor of 10 by the reduction of J/N_N in the wave driven case. Thus the nucleation rate can make the difference between NLCs which are detectable or not.

In order to understand the basic dependencies between nucleation rate, ice particle number density, mean radius and backscatter signal, the first set of CARMA simulations with climatological background conditions and the dust profile of Hunten et al. (1980) is analyzed. This set of simulations provides an excellent framework to study the effects of varying nucleation rates, because all relevant parameters are easily controlled. In particular the nucleation altitude does not vary, which would be the case for the Megner et al. (2008b) profile or the time dependent background fields. Figure 5.3 gives an overview over the NLC properties after 36 h of simulation time (24 h after reaching the final background temperature) for nucleation rate prefactors between 10^{-10} and 10^{10}. The total ice particle number density n_tot at the altitude of the maximum backscatter coefficient is given in black and the mean radius r_mean in blue. The red curves show the maximum NLC backscatter coefficient β_max for light with a wavelength of $\lambda = 532\,\mathrm{nm}$. The different red curves refer to the optical properties obtained for spheroids with axis ratios (AR) between between AR = 1/7 and AR = 7 (Rapp et al., 2007; Hervig et al.,

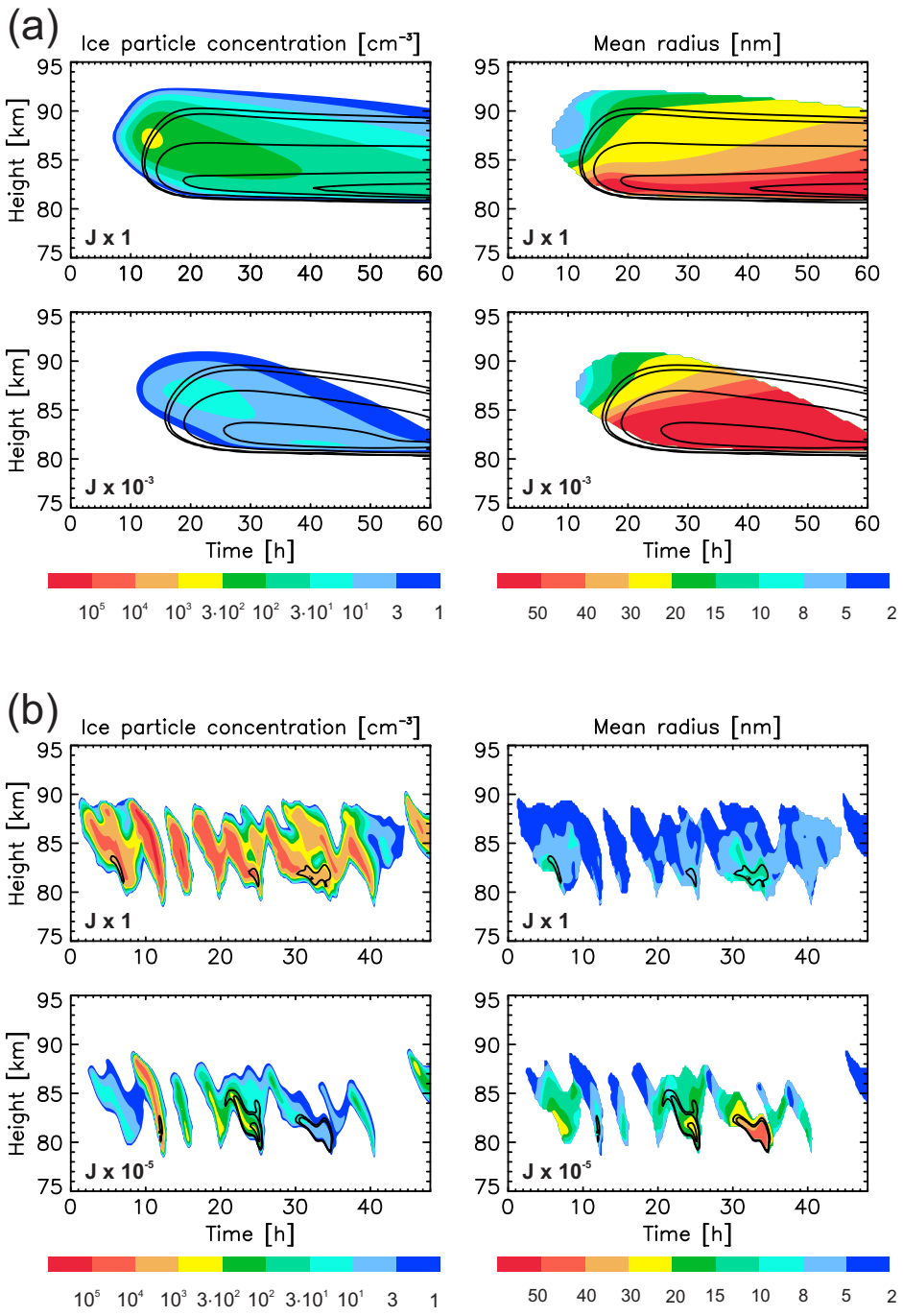

Figure 5.2: CARMA simulation with (a) climatological and (b) wave driven background fields. The corresponding temperature and wind fields for the wave driven simulations are shown in Fig. 3.3 (b). The upper row in (a) and (b) is generated with the reference nucleation rate ($J \times 1$), the lower row with reduced nucleation rate ($J \times 10^{-3}$ and $J \times 10^{-5}$). The black contour lines indicate backscatter coefficients of $(0.05, 0.1, 1, 10, 30) \cdot 10^{-10}$ sr^{-1}m^{-1}. This figure is reproduced from Wilms et al. (2016).

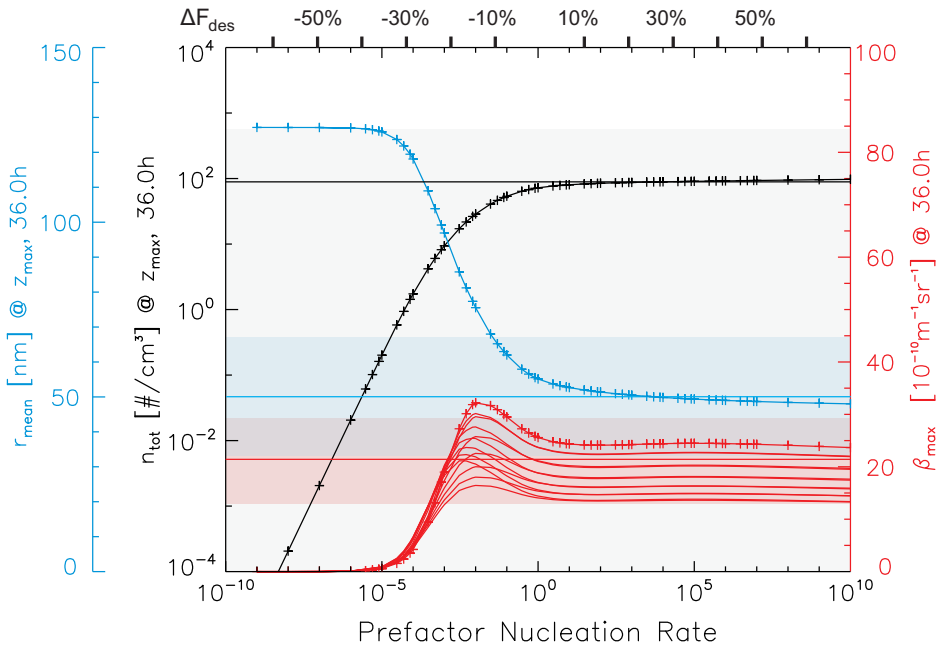

Figure 5.3: NLC properties in climatological background field after 36 h of simulation time (24 h after the final temperature profile is reached) for different nucleation rate prefactors. Mean radius (blue) and total ice number density (black) are given at the altitude of the maximum backscatter coefficient. The backscatter coefficient (red) is shown for spheroidal ice particles with axis ratios between 1/7 and 7, spherical particles are indicated with crosses. The horizontal lines mark mean values for strong NLCs and the shaded range their standard deviation derived by lidar measurements (Baumgarten et al., 2008). The upper scale indicates the relative change in percent of the desorption energy ΔF_{des} leading to the corresponding nucleation rate prefactor. This figure is reproduced from Wilms et al. (2016).

2009b), the backscatter coefficients obtained for spheres are marked with crosses. The range of axis ratios is based on SOFIE satellite observations reported by Hervig et al. (2009b). Although the majority of NLCs detected by SOFIE has AR ≈ 2, NLCs with lower ice mass density tend to be more aspherical (up to AR $= 7$). The nucleation rate prefactor reflects a change of the desorption energy ΔF_{des}, which is indicated by the upper scale in Figure 5.3 for nucleation conditions at 130 K (e.g., a 50% increase of ΔF_{des} corresponds to a prefactor of 10^7).

Several basic dependencies can be directly inferred from Figure 5.3: In the low nucleation rate regime (prefactor less than 10^{-2}) a linear relationship is found between the nucleation rate prefactor and the total ice particle number density. For larger prefactors, n_{tot} reaches the limiting value of about $10^2\,\mathrm{cm}^{-3}$. The smallest values of r_{mean} are reached in the large prefactor regime. In this regime the ice particle growth is limited by the available water vapor, for which a large number of ice particles competes. In the

low prefactor regime the radius is limited by the growth rate. For typical conditions, the growth rate lies between $3\,\mathrm{nm\,h^{-1}}$ and $10\,\mathrm{nm\,h^{-1}}$, which results in (unrealistically large) mean radii of about 130 nm after roughly 24 h of particle growth.

This first overview already shows that NLCs with completely different properties can be modelled for the same background atmosphere by just changing the nucleation rate. However, not all of the scenarios lead to NLC properties which are commonly observed. Therefore the NLC parameters from the CARMA simulations are compared to those derived from lidar observations and to those derived from satellite observations.

5.3.1 Comparison with lidar measurements

Baumgarten et al. (2008) present a summary of NLC properties (e.g. total number density and mean radius) for different NLC brightness classes from 8 years of lidar measurements at ALOMAR (69° N, 16° E). This data set is used to benchmark the model results. In a first step, the brightness class (faint, weak, medium and strong NLC; Fiedler et al., 2003) of the simulated NLCs is identified, considering axis ratios between 1/7 and 7. Then, it is checked whether the mean radius and number density of the simulated NLC fall within one standard deviation of the values given by Baumgarten et al. (2008, Table 3). If this is the case, i.e. when all three simulated parameters match the observations, this is called a 'match' for the considered nucleation rate prefactor. This procedure is repeated for every time step of the simulation and it is counted how many matches for each prefactor are found.

Simulation results for climatological background

Figure 5.4 depicts the results for climatological background conditions and both dust profiles. The top two panels show the histogram of matches for the four brightness classes, panel (a) for simulations using the dust profile of Hunten et al. (1980) and panel (b) for the dust profile of Megner et al. (2008b). Panel (c) indicates the range of prefactors for which NLCs with 'realistic' properties were modeled, it simply marks the prefactors where at least one match has been found.

In the case of the Hunten et al. (1980) profile the standard nucleation rate (prefactor 1) yields good results in producing realistic NLCs in all brightness classes (from faint to strong NLCs). NLCs generated with higher nucleation rates (prefactors larger than 1) also have realistic properties. In this prefactor regime the nucleation rate does not have a significant influence on NLC properties, as shown in Figure 5.3. Reducing the nucleation rate by more than a factor of 10^{-2} prohibits matches in all brightness classes. As seen from the histogram, most matches are obtained for medium and bright NLCs.

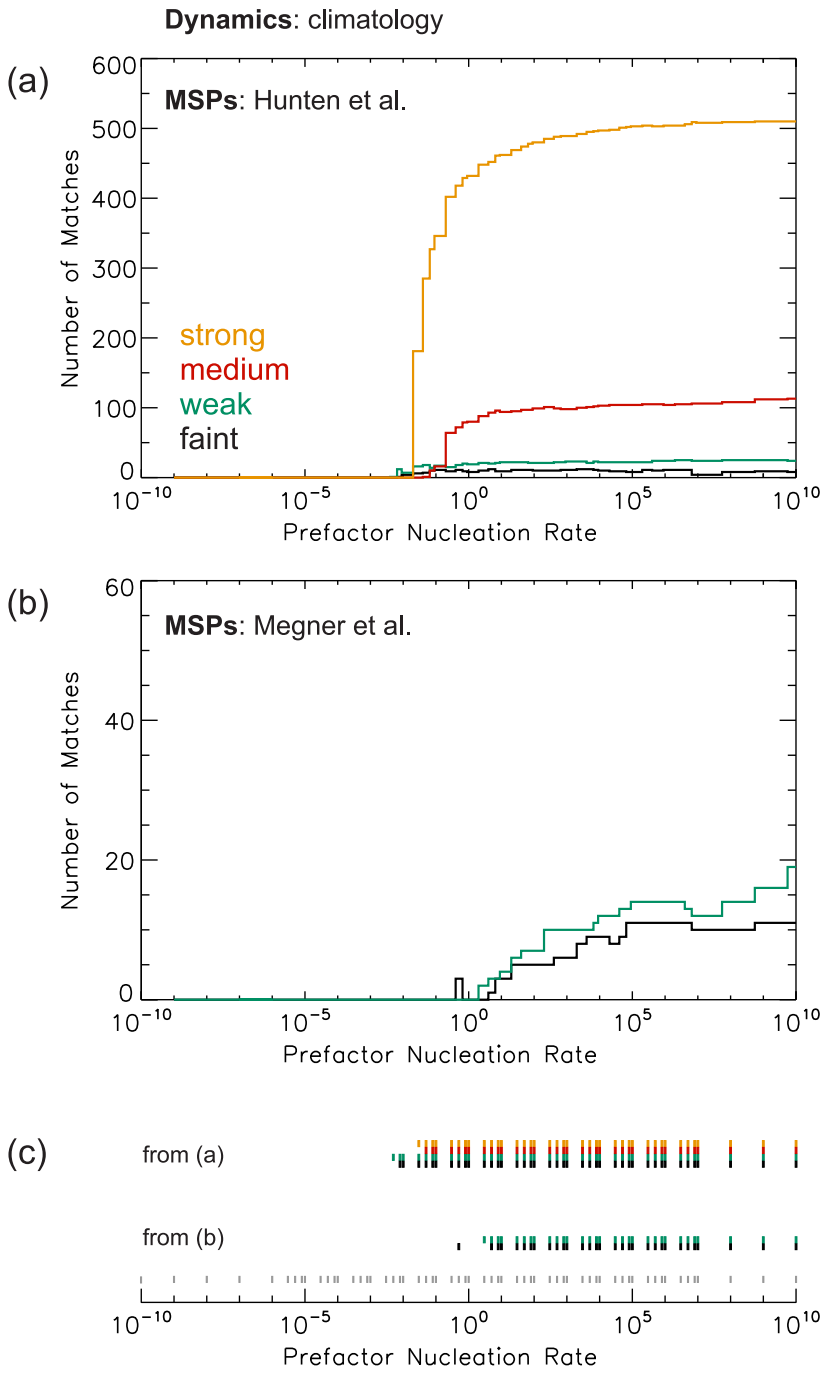

Figure 5.4: The matches of NLCs generated in climatological background profiles with the dust profile of (a) Hunten et al. (1980) and (b) Megner et al. (2008b) are shown as histograms depending on the nucleation rate prefactor (see text for details). Panel (c) shows the prefactors which lead to at least one match. The different colors refer to matches in the different brightness classes from faint to strong NLCs. The gray marks along the abscissa indicate the prefactors which are evaluated. This figure is extended from Wilms et al. (2016).

This is due to the long life time of NLCs in the climatological background, where bright NLCs develop quickly and then survive for several hours (see Fig. 3.5).

In the case of the Megner et al. (2008b) MSP profile, the nucleation rate must be two to three orders of magnitude higher to yield the same NLCs as with the Hunten et al. (1980) profile. This is because the MSP number densities differ by two to three orders of magnitude between the two MSP profiles (see Tab. 3.1). This difference is best seen in the onset of 'realistic' NLCs in panel (c) which occurs at a prefactor of 10^{-2} in the case of the Hunten et al. (1980) profile and at a prefactor of 10 for the Megner et al. (2008b) profile. The lower MSP number density in the profile of Megner et al. (2008b) is partly compensated by a higher nucleation rate per particle, but the final number of ice particles is nevertheless limited by the total number of MSPs and is therefore lower than in the simulation with the Hunten et al. (1980) profile. The low number density of ice particles allows them to grow to exceptionally (and unrealistically) large radii (130 nm and more) and become very bright. As a result, the combination of ice number density, mean radius and backscatter coefficient is not in the range of typical observations of Baumgarten et al. (2008). Consequently no matches are found for medium and strong NLC with the dust profile of Megner et al. (2008b). Only the few matches for faint and medium NLCs are found from the first time steps of the simulation, where the NLC still develops and has not yet reached its final brightness.

Simulation results for wave driven background

Figure 5.5 shows the same analysis as in Fig. 5.4 but with the wave driven background fields of the KMCM and for all six starting times of the CARMA simulations. The first point to note is that the prefactor range where 'realistic' NLCs occur is strongly limited and centered around a prefactor of about 10^{-4} for the Hunten et al. (1980) profile and 10^{-1} for the Megner et al. (2008b) profile. As in the climatological case, the difference between the two dust profiles can be attributed to the different number densities of available MSPs (i.e. MSPs larger than r^*) which differ by about two to three orders of magnitude (see Tab. 3.1). Contrary to the results shown in Figure 5.4, both dust profiles lead to matches in only the brightness classes of faint and weak NLCs, because brighter clouds generally do not develop in these simulations with wave driven background profiles. This indicates that the NLC development is strongly determined by the wave driven perturbations of the background atmosphere. As shown later, this is in particular due to waves in the vertical wind, which limit the growth time of the ice particles.

In the following, the sensitivity of these results with respect to the chosen atmospheric background conditions and the MSP profile is analyzed. The MSP number density is varied by multiplying the original profile with the factors of 100, 10, 0.1, 0.01, and 0.001. Note that this variation can either reflect the general uncertainty of the MSP number

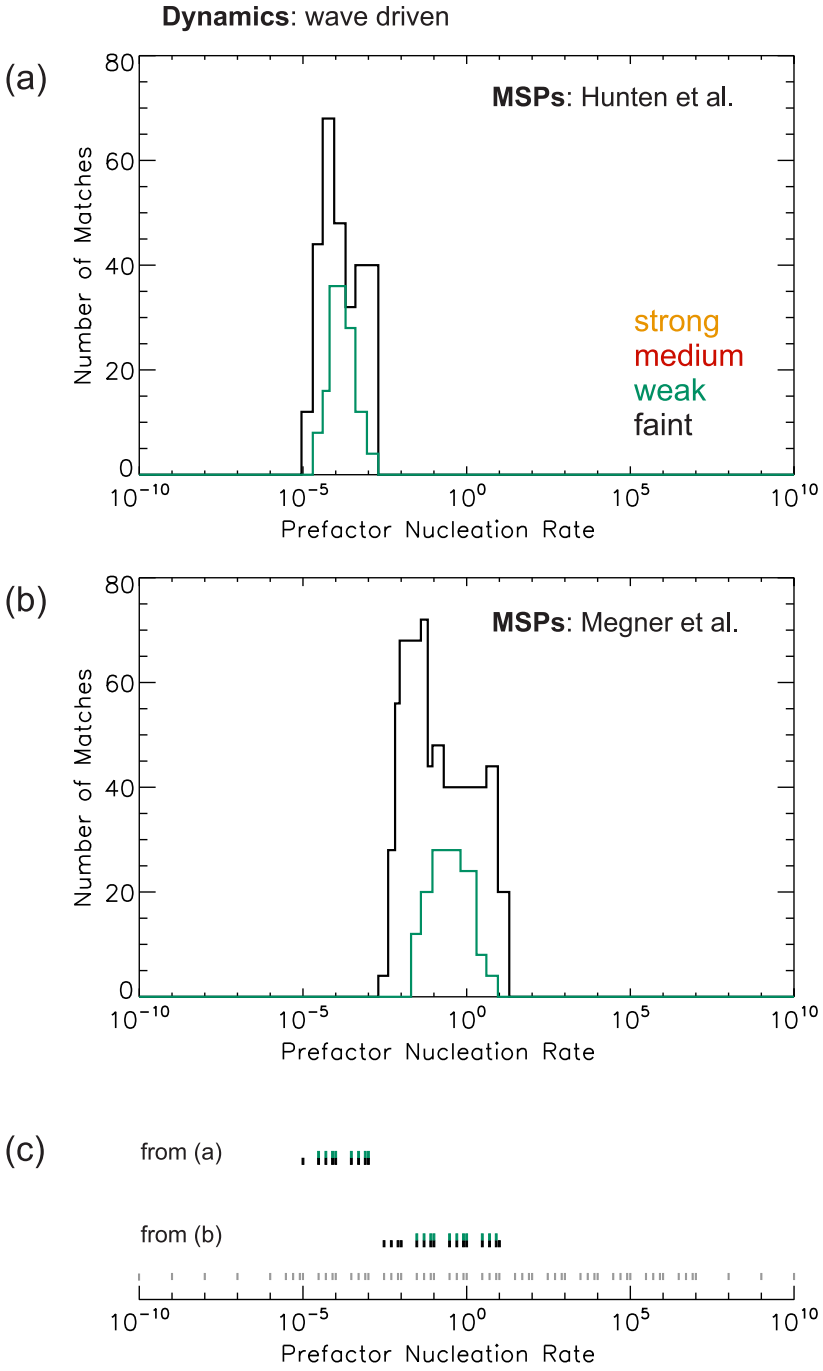

Figure 5.5: The same analysis as presented in Fig. 5.4, but for the wave driven simulations using the KMCM background profiles. This figure is extended from Wilms et al. (2016).

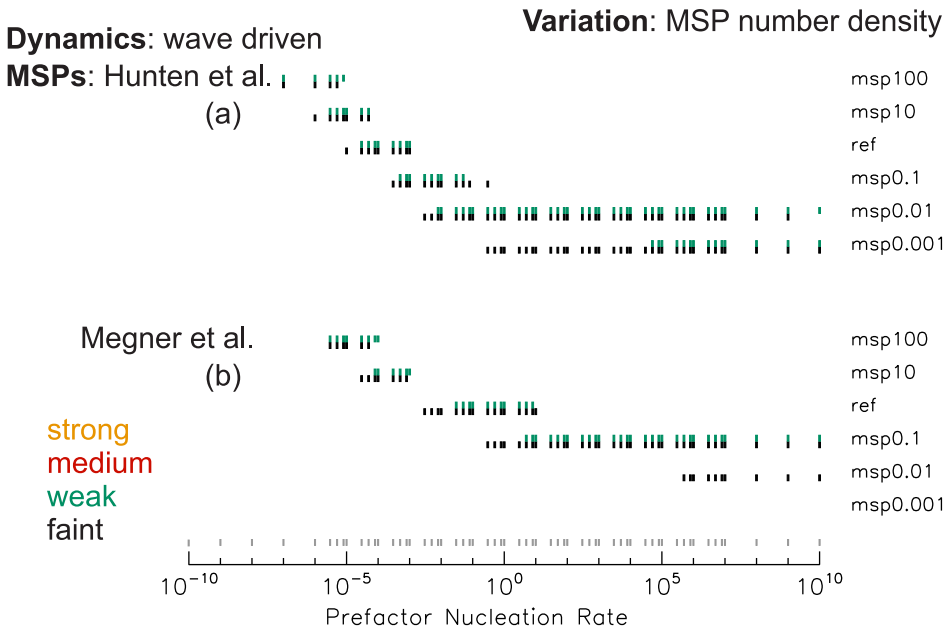

Figure 5.6: Overview over nucleation rate prefactors that lead to NLCs comparable to lidar observations (as in Fig. 5.4c and Fig. 5.5c). The MSP profile of (a) Hunten et al. (1980) and (b) Megner et al. (2008b) is multiplied with the factors of 100, 10, 0.1, 0.01, 0.001. The reference case is labeled with 'ref'. This figure is extended from Wilms et al. (2016).

density or the uncertainty of the critical radius. A reduction of the MSP number density thereby corresponds to a larger critical radius (e.g., larger surface tension), and vice versa for an increase of the MSP number density. The temperature profile is varied by adding an altitude and time independent offset of 5 K, 3 K,1 K, −1 K,−3 K,−5 K, and −10 K, reflecting, for example, the effect of tides or the seasonal variation. The sensitivity to the vertical wind variations is tested by multiplying the wind field with the factor of 0.5. Temperature and wind fields are changed independently of each other, so they do not necessarily represent a realistic state of the atmosphere. However, this setup allows to distinguish wind induced effects from temperature induced effects. These CARMA simulations are evaluated with the same method as described above. The results are presented in Figs. 5.6, 5.7, and 5.9. For reasons of clarity, only the plots indicating the range of prefactors are shown and not the complete histograms. Whenever the histograms offer further insights, they are evaluated separately.

From Fig. 5.6 it is found that the nucleation rate range in which realistic NLC can be modelled is directly linked to the available MSP number density. The increase of the MSP number density by one order of magnitude shifts the matching nucleation rate prefactors by one order of magnitude towards lower prefactors. This inverse relationship can be seen in Fig. 5.6 (a) for the simulations titled 'msp100' to 'msp0.1'. In the case

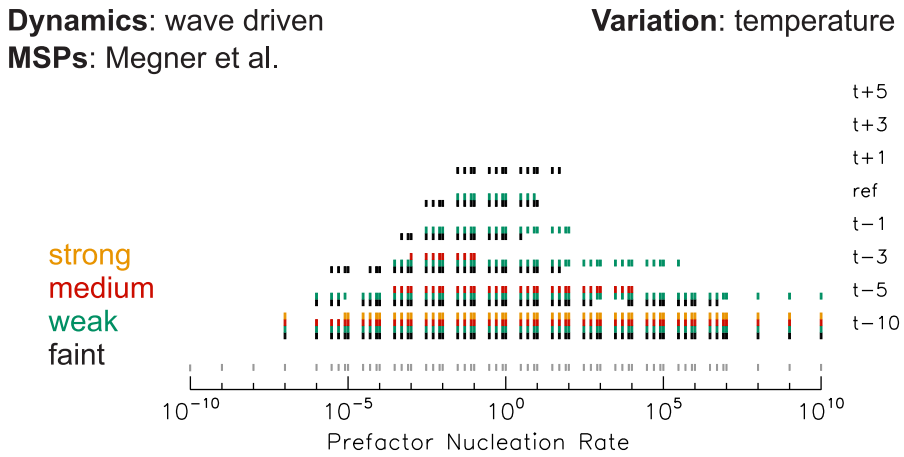

Figure 5.7: Overview over nucleation rate prefactors that lead to NLCs comparable to lidar observations (as in Fig. 5.6b). The temperature profile is modified with a constant offset of 5 K, 3 K,1 K, −1 K,−3 K,−5 K,−10 K. The reference case is labeled with 'ref'. This figure is reproduced from Wilms et al. (2016).

of greatly reduced MSP number densities ('msp0.01' and 'msp0.001') NLCs occur over a broad range of nucleation rate prefactors. As only few MSPs are present in these simulations, the nucleation rate per particle must be generally higher in order to generate the same number density of ice particles. This will rapidly deplete the available MSPs. If this happens on time scales smaller than typical dynamical time scales, then the nucleation rate can be almost arbitrarily large without altering the NLC properties. Similar results are found when varying the dust profile of Megner et al. (2008b) as shown in panel (b). However, the relationship between the matching prefactor range and the MSP scaling factor is not exactly linear, namely for the following reason: The main nucleation height is at the temperature minimum for the case that the dust profile does not exhibit an altitude dependence. In the profile of Megner et al. (2008b), the MSP number density increases towards lower altitudes (cf. Fig. 1 of Gumbel and Megner, 2009), thus leading to a main nucleation region about 2 km lower than in the simulations with the profile of Hunten et al. (1980). This altitude difference changes with absolute MSP number density, thus leading to a deviation from the linear relationship. For the lowest MSP number densities, none of the simulated NLCs match the observations, because too few ice particles are generated to yield sufficiently bright NLCs.

The simulations with varied background temperature in Fig. 5.7 indicate that the prefactor range is less restricted when the temperature is lower. Additionally, it is found that the background temperature has to be decreased by 3 K for medium NLCs to develop and by 10 K for strong NLCs. Here, only the results from the simulations with the MSP profile of Megner et al. (2008b) are shown, because the simulations with the Hunten et al. (1980) profile lead to the same conclusions. The maxima of the

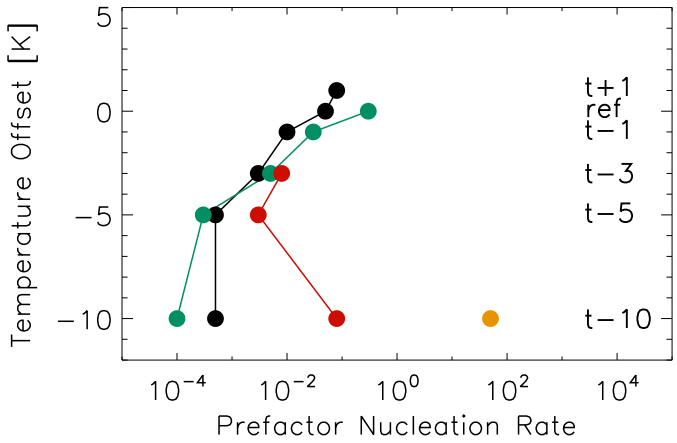

Figure 5.8: The nucleation rate prefactor that obtained the largest number of matches for different offsets of the KMCM background temperature profile. The different colors refer to the different brightness classes of NLCs (black: faint NLCs, green: weak NLCs, red: medium NLCs, yellow: strong NLCs).

histograms, which underlie Fig. 5.7, are shifted to lower prefactors if the background temperature is reduced, as shown in Fig. 5.8. This means that even though the prefactor range is less restricted for lower temperatures, the most matches for realistic NLCs are obtained when the nucleation rate is further reduced compared to the reference setup. In the most extreme case, when the background temperature is reduced by 10 K, the histogram is very broad, with the result that no distinct maximum is present as in the other simulations. For this reason, the prefactor with the maximum number of matches does not fit well to the trend described above.

Figure 5.9 shows the sensitivity to the vertical wind velocity. NLC brightness is greatly increased if the vertical wind is scaled by a factor of 0.5. Scaling the vertical wind retains the time intervals of upward and downward transport and simply increases or decreases the vertical distance travelled by the ice particles during one wave cycle. If the wind amplitude is reduced by only a factor of two, strong and medium NLCs develop, whereas otherwise only weak and faint NLCs occur. This increase in brightness can be explained by the particle trajectories which are shown in Figure 5.10 (see Sec. 3.4 for details). Panel (a) shows NLC properties for the original wind field and panel (b) for wind velocities reduced by a factor of two. The black lines represent characteristic trajectories. While in panel (b) the trajectories follow the up- and downward motion throughout several wave cycles, they are mostly limited to one downward phase in the original wind field in panel (a). Since the trajectories visualize the transport of the ice particles, it becomes clear that a reduction of the vertical wind greatly enhances the ice particle lifetime. As a consequence, the ice particles grow to larger radii (middle row) and the backscatter coefficient increases accordingly (bottom row).

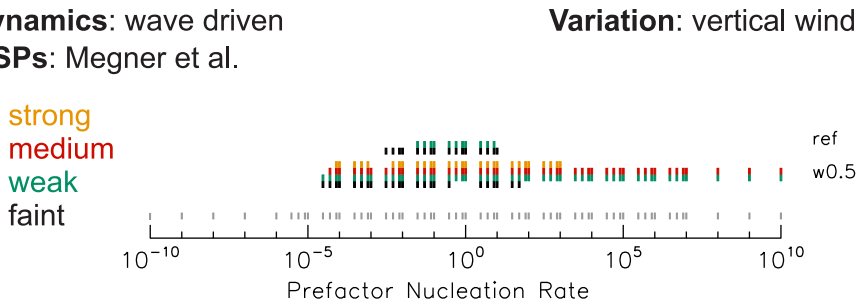

Figure 5.9: Overview over nucleation rate prefactors that lead to NLCs comparable to lidar observations (as in Fig. 5.6b). The vertical wind profile is multiplied with the factor of 0.5, the reference case is labeled with 'ref'. This figure is reproduced from Wilms et al. (2016).

5.3.2 Comparison with satellite measurements

NLC properties have been extensively studied from space (e.g., DeLand et al., 2006). Sophisticated retrievals allow for the deduction of NLC parameters from satellite measurements such as the total number density of ice particles and their mean radius (e.g., Thomas and McKay, 1985; von Savigny et al., 2004; Karlsson and Gumbel, 2005; Hervig et al., 2009c). The SOFIE instrument on the AIM satellite uses solar occultation measurements in the wavelength range from 0.3 µm to 5.3 µm to determine NLC properties as well as vertical profiles of temperature, water vapor and other trace gas mixing ratios (Gordley et al., 2009). Measurements of mesospheric ice particle properties are also performed by the OSIRIS instrument on the Odin satellite (Hultgren et al., 2013). By applying a tomographic retrieval, horizontal and vertical profiles of ice particle properties are determined simultaneously. Under the assumption of a Gaussian size distribution, where the width is directly related to the mean radius (Baumgarten et al., 2010), Hultgren and Gumbel (2014) derive the number density, mean radius and ice mass density of NLCs from OSIRIS measurements.

Hervig et al. (2009c, Fig. 17) depict their SOFIE NLC measurements in the $n_{\mathrm{tot}} - r_{\mathrm{mean}}$ plane, where all datapoints are from the altitude of the maximum extinction coefficient. Hultgren and Gumbel (2014, Fig. 9) show a similar plot with their $n_{\mathrm{tot}} - r_{\mathrm{mean}}$ measurements, but with datapoints from the complete vertical profile. In order to qualitatively compare the NLC modeling results with the two satellite data sets, the modeled NLCs are visualized in the same $n_{\mathrm{tot}} - r_{\mathrm{mean}}$ plane. Figure 5.11 (left) shows the CARMA results at the altitude of maximum backscatter coefficient, color coded by the nucleation rate prefactor. The shaded area in the background marks the range of values reported by Hervig et al. (2009c). In Figure 5.11 (right) the simulated ice particle properties of all altitudes are shown, again color coded by the nucleation rate prefactor. Here, the shaded area marks the range of values reported by Hultgren and

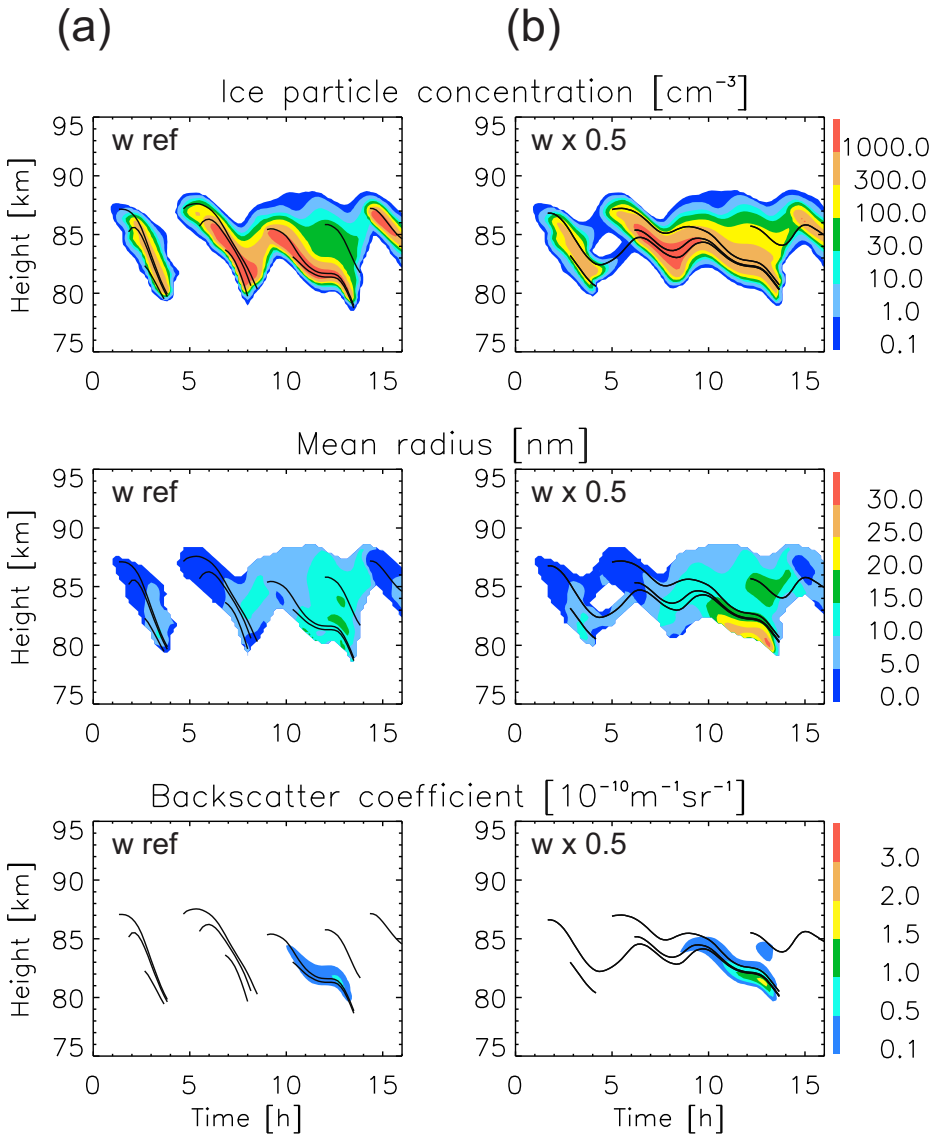

Figure 5.10: Visualization of tracer trajectories (black lines) in (a) the reference wind field and (b) the wind field scaled by 0.5. The ice number density is shown in the top row, the mean radius of the ice particles in the middle and backscatter coefficient in the lower row. This figure is reproduced from Wilms et al. (2016).

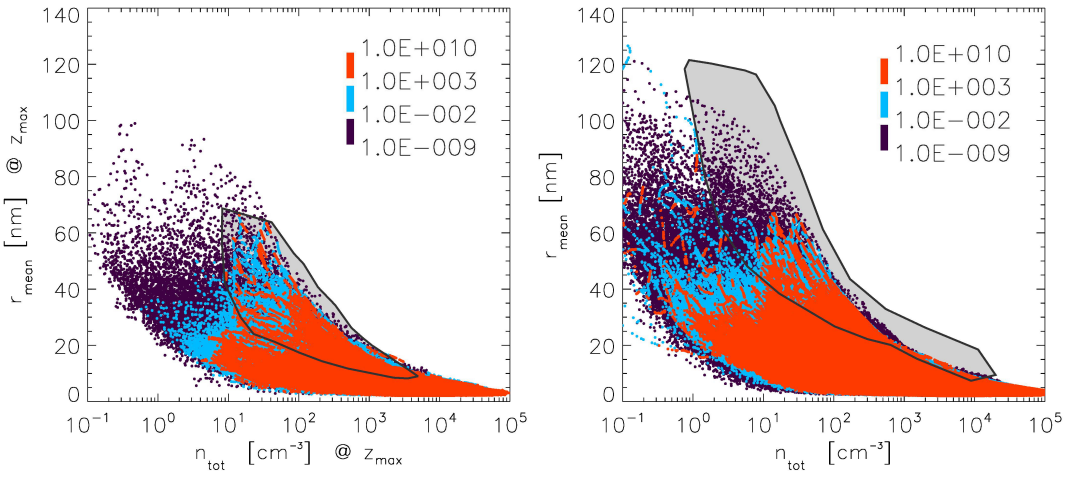

Figure 5.11: Distribution of modelled NLCs in the $n_{\mathrm{tot}} - r_{\mathrm{mean}}$ plane (left) at the altitude of the maximum backscatter signal and (right) for all altitudes. The analysis is based on simulations with the dust profile of Megner et al. (2008b) and the wave driven background profiles. The colors refer to different ranges of nucleation rate prefactors. Contour lines delimit the area where satellites have detected NLCs, based on (left) Hervig et al. (2009c) and (right) Hultgren and Gumbel (2014). This figure is reproduced from Wilms et al. 2016).

Gumbel (2014). In these figures the data of all KMCM simulations in the reference setup and those with varied background temperatures are combined, as those possibly present realistic states of the atmosphere. The data set is limited to those points with an ice mass density greater than $0.1\,\mathrm{ng\,m^{-3}}$.

The best coverage of the parameter space seen by the two satellites is achieved with CARMA simulations using reduced nucleation rates (dark colored data points). The large particle radii which are detected by the satellites (up to 70 nm and 120 nm for SOFIE and OSIRIS respectively) are only generated in CARMA runs with nucleation rate prefactors lower than 10^{-2}. However, not the whole observed parameter space is covered by the simulations. In particular, the range where the satellite data extends to larger number densities and simultaneously to larger radii is not covered by the simulations. The NLCs situated in this range are characterized by larger ice mass densities, which are not reached in the model.

For emphasizing the importance of gravity wave fluctuations, Fig. 5.12 shows the equivalent analysis as in the previous figure, but with the climatological background fields. It is clearly evident, that these simulations only partly cover the observed range, in particular because the observed large ice particle number densities are not generated in the climatological backgrounds.

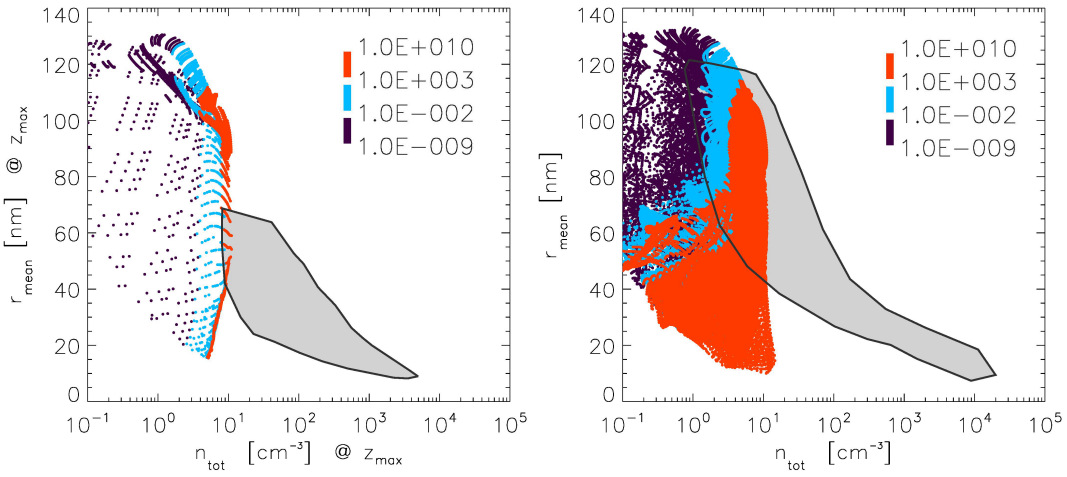

Figure 5.12: Distribution of modelled NLCs in the $n_{\mathrm{tot}} - r_{\mathrm{mean}}$ plane at (left) the altitude of the maximum backscatter signal and (right) for all altitudes. The analysis is based on simulations with the dust profile of Megner et al. (2008b) and the climatological background profiles. The colors refer to different ranges of nucleation rate prefactors. Contour lines delimit the area where satellites have detected NLCs, based on (left) Hervig et al. (2009c) and (right) Hultgren and Gumbel (2014).

5.4 Discussion

The nucleation rate is a critical factor which determines the properties of mesospheric ice particles. By changing the nucleation rate, NLCs with notably different characteristics are generated. In wave driven simulations and when using a MSP background profile with rather numerous MSPs (the profile from Hunten et al., 1980) the nucleation rate must be reduced significantly in order to model NLCs that resemble those seen by observations. The comparison with lidar measurements (Baumgarten et al., 2008) yields the best agreement if the nucleation rate is reduced by four to five orders of magnitude compared to standard assumptions. As the nucleation rate is defined by the nucleation rate per particle times the MSP number density, the above mentioned required reduction of the nucleation rate can partly be compensated by a lower number density of MSPs, such as in the MSP profile by Megner et al. (2008b). The comparison with satellite observations of NLCs (Hervig et al., 2009c; Hultgren and Gumbel, 2014) yields the best agreement if the nucleation rate per particle is reduced by two orders of magnitude or more for both dust profiles.

The theoretically expected inverse relationship between nucleation rate per particle and MSP number density is supported by our simulations: Increasing the MSP number density by one order of magnitude requires the nucleation rate prefactor to be decreased by one order of magnitude to yield equivalent NLCs (see Figure 5.6). This inverse relationship holds as long as there are enough MSPs available, i.e. the limiting factor is

not the availability of MSPs but the nucleation rate. If the availability of MSP is the limiting factor, the nucleation rate can be arbitrarily large in the simulations without affecting NLC properties.

5.4.1 Comparison with 'minimal impact' hypothesis by Megner (2011)

The backscatter signal B should be roughly proportional to $N \cdot r^6$ based on the reasonable assumption that mesospheric ice particles act as Rayleigh scatterers in the visible wavelength range. Expressing the radius r via the ice mass M_{ice} yields $B \propto M_{\mathrm{ice}}^2/N$. The backscatter signal should thus vary with ice number density N and should therefore depend on the number density of initial ice nuclei, i.e. the MSP number density. This relationship has previously been investigated by Megner (2011). Using the CARMA model she varied the number density of 1 nm-sized MSP from 1 cm^{-3} to 10^5 cm^{-3} and analyzed the resulting NLC properties. Unexpectedly, she found B and M_{ice} to be almost independent of the initial ice nuclei number density N.

The set of simulations presented above includes sensitivity runs with different MSP number densities, which is use to test the $B \propto M_{\mathrm{ice}}^2/N$ relationship. The set of simulations with the Hunten et al. (1980) profile and varied number densities are set up similar to the simulations by Megner (2011): (1) no altitude dependence of the MSP profile and (2) with a MSP number density that ranges from about $2\,\mathrm{cm}^{-3}$ ('msp0.001') to $2 \times 10^5\,\mathrm{cm}^{-3}$ ('msp100') for MSP larger than 1 nm, covering the complete range of MSP number densities that has been analyzed by Megner (2011). Following her analysis, column integrated variables are considered, so that B is the integrated albedo and M_{ice} is the ice water column. However, the NLC properties resulting from this study show several differences: In Figure 5.13 (a) the time series of the ice water column M_{ice} is presented, which is more sensitive to the initial number of MSPs than in the analysis of Megner (2011, Fig. 2a) (note the logarithmic scale). Increasing the MSP number density mainly shifts the curves of M_{ice} to larger values. The behavior of the integrated albedo B in panel (b) is more complex due to the nonlinearity of the cloud development process. Therefore, the $B \propto M_{\mathrm{ice}}^2/N$ relationship is tested by plotting M_{ice}^2/B in panel (c), which should be proportional to N. This is roughly the case, as the different curves are separated by about one order of magnitude, reflecting the one order of magnitude difference in the underlying MSP number density. To illustrate this dependence more clearly, the time averaged values for M_{ice}^2/B are shown versus MSP number densities in panel (d). An almost linear dependence is found, supporting the $B \propto M_{\mathrm{ice}}^2/N$ relationship. Only the CARMA run 'msp100' deviates significantly from this relationship. In this simulation the NLC development is limited by the available water vapor. Due to the very large number density of MSPs, a large number of ice

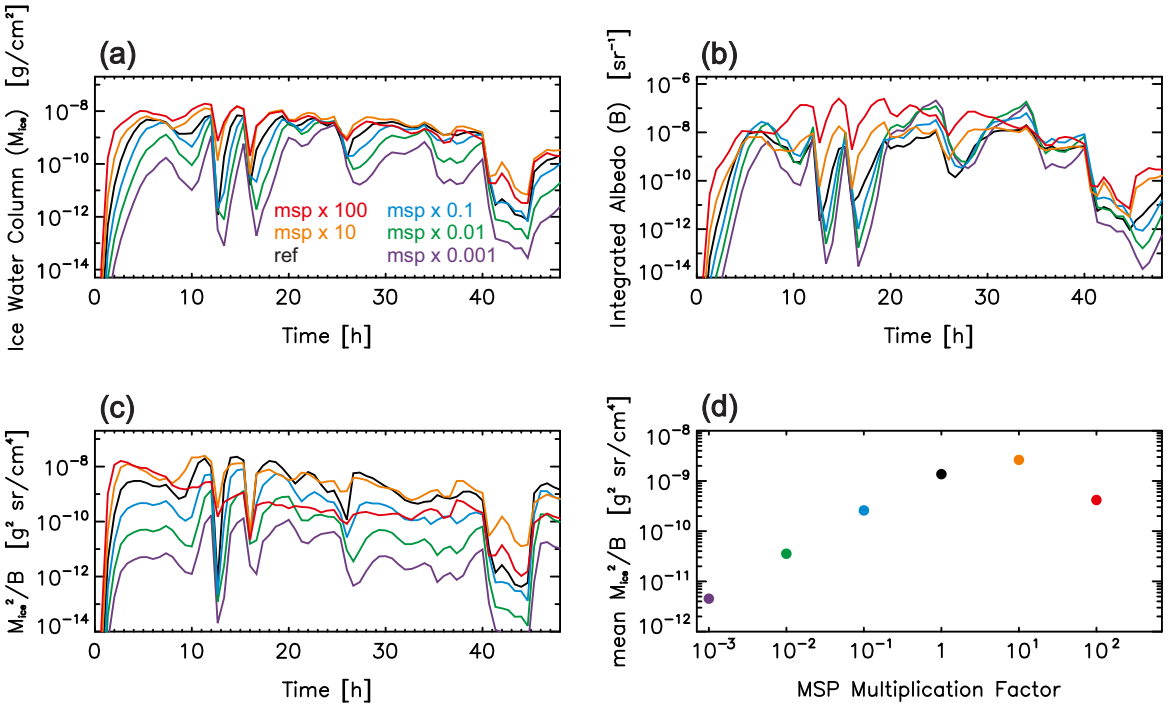

Figure 5.13: Temporal development of (a) ice water column M_{ice}, (b) integrated albedo B, and (c) M_{ice}^2/B from the simulation shown in Fig. 5.2b with prefactor 1. The number density of initial MSPs is increased relative to the reference run by a factor of 10 and 100 and decreased by a factor of 0.1, 0.01, and 0.001. (d) Time-averaged values for M_{ice}^2/B are shown for the different MSP number density scaling factors. This figure is reproduced from Wilms et al. (2016).

particles is formed which rapidly depletes the available water vapor. It is thus not available at later time steps, leading to a gradual decrease of B in the 'msp100' run. The conclusion to be drawn from this analysis is that our simulations follow the simple relationship of $B \propto M_{\text{ice}}^2/N$, at least as long as the available water vapor is not the limiting factor.

How can the difference to the simulations of Megner (2011) be explained? Megner (2011) used wave-perturbed temperature fields to drive the model, but did not use (except for one case) the corresponding wind fields. Instead, the ice particles experienced a time-constant up-draft due to the mean vertical wind. Hence, the only way for ice particles to reach lower altitudes where they can grow effectively ('growth region') is by Eddy diffusion. This is also the case when Megner (2011) used the wave-perturbed wind fields, as the assumed vertical wind velocities were smaller than the turbulent velocities associated with the vertical Eddy diffusion coefficient (Lübken, 1997). As a result, the simulated NLC properties in Megner (2011) are independent of the initial number of ice particles. In the here presented simulations the dominant process for vertical

transport is the vertical wind, because the turbulent velocities and sedimentation velocities are comparable to or smaller than the wave-perturbed wind velocities. As seen for example in Fig. 3.6e the whole particle population is transported downward with the wave-perturbed wind after nucleation. The total ice particle number density is roughly unchanged between the nucleation region and growth region. Therefore, all nucleated particles do contribute to the brightness of the cloud. Hence, the clear relationship is found between initial MSP number density, or nucleation conditions in general, and the observed NLC properties.

5.4.2 Discussion of sensitivities

The results presented in Figure 5.7 emphasise the importance of the background temperature. The first point to note is that in an atmosphere with lower background temperature, the development of realistic NLC is less sensitive to the nucleation rate. The second point is that medium and strong NLCs only develop if the temperature is reduced by at least 3 K and 10 K, respectively. This result is consistent with different interpretations of the temperature offset implemented in the simulations: First of all, the mean KMCM temperature has a warm bias of about 5 K compared to the coldest temperatures measured at ALOMAR by Lübken (1999) with the falling spheres technique (see Figure 3.2). Nevertheless, the mean KMCM profile lies well in the range of temperatures measured within the NLC season. The result that NLCs get brighter in a colder environment is consistent with the observed seasonal variation. The brightest NLCs are detected at the peak of the season around 25 days after solstice (mid of July) (Fiedler et al., 2009). This coincides with the minimum temperatures of the climatology by Lübken (1999). However, a reduction of 5 K in the model is not enough to yield strong NLCs. This implies that for the development of strong NLCs an additional forcing is necessary. The temperature offset implemented in the simulations can reflect large scale temperature perturbations with long periods and large vertical wavelengths, such as planetary waves or tides. It has been shown in various studies that both have a major influence on NLCs. Fiedler et al. (2005) conclude from the mean diurnal variation of NLCs that occurrence, brightness and altitude of NLCs are significantly controlled by tides. Planetary waves are known to modulate NLC occurrence and brightness (e.g., Kirkwood and Stebel, 2003; Merkel et al., 2003). It was shown by Merkel et al. (2008) that the brightness of NLCs is almost anticorrelated to the temperature perturbations induced by planetary waves. They find that the maximum amplitude of temperature perturbations is relatively small (2 K - 3.5 K) but has a significant effect on NLC brightness. A similar tendency is found in the here presented CARMA simulations, where a reduction of the background temperature by 3 K increases the NLC brightness from weak to medium NLC (see Figure 5.7). Liu et al. (2015) find similar temperature amplitudes and a high anticorrelation to NLC ice water content. For a temperature decrease of 3 K, they measure an ice water content

increase between $5\,\mathrm{g\,km^{-2}}$ and $30\,\mathrm{g\,km^{-2}}$ (see their Fig. 5). The CARMA simulations show a similar response: A reduction of the background temperature of 3 K leads to an increase of the ice water content between $17\,\mathrm{g\,km^{-2}}$ and $34\,\mathrm{g\,km^{-2}}$. This can be considered as support for the interpretation of the temperature offset in terms of planetary wave perturbations.

Besides the nucleation conditions and background temperatures, the vertical wind at the mesopause is one of the key parameters that affect NLC properties in the CARMA simulations. The magnitude and direction of the vertical wind determines the residence time of ice particles in the supersaturated altitude range. As the cold phase of a wave is typically followed by a downwind phase, freshly nucleated ice particles are subsequently transported to lower altitudes by the background wind, which is much faster than the additional downward sedimentation. Ice particles which are transported below the supersaturated region will evaporate rapidly. If the ice particles survive the downwind phase they can experience another full wave cycle with the following upwind phase, which extends their lifetime significantly. Whether the ice particles survive the downwind phase or not depends on the wind amplitude, the period of the wave and the vertical extent of the supersaturated region. Since the lifetime determines the maximum size and therefore also the brightness of the cloud, it is crucial to check whether the KMCM wind amplitudes are realistic or not.

First of all it is important to stress that the mesopause region is characterized by highly variable vertical wind velocities. This large variability and also the amplitude of the vertical wind have been measured by various instruments and reported in numerous studies. Typical vertical wind amplitudes measured by the EISCAT (European Incoherent Scatter) radar range from ± 2 m/s to ± 6 m/s (Hoppe and Hansen, 1988; Hoppe and Fritts, 1995; Mitchell and Howells, 1998; Rapp and Hoppe, 2006), vertical wind variances range from 5 $\mathrm{m^2/s^2}$ to 15 $\mathrm{m^2/s^2}$ (Fritts et al., 1990; Strelnikova and Rapp, 2011). Vertical wind variances measured by the mobile SOUSY (SOUnding SYstem) radar are on the order of 2 $\mathrm{m^2/s^2}$ to 3 $\mathrm{m^2/s^2}$ (Rüster and Reid, 1990). MAARSY, the Middle Atmosphere Alomar Radar System, regularly detects vertical wind amplitudes of 5 m/s (Stober et al., 2013). From chaff foil cloud experiments, wind amplitudes of ± 4 m/s to ± 6 m/s have been deduced (Widdel, 1987). Vertical wind velocities determined from the Doppler shift of the OH emission line, measured with a Michelson interferometer by Bhattacharya and Gerrard (2010), reveal daily mean velocities (over an 8 h window) of 0 m/s to ± 10 m/s with daily standard deviations of 7 m/s to 14 m/s. Iron lidar measurements reported by Höffner and Lautenbach (2009) show vertical wind amplitudes of ± 4 m/s.

The KMCM vertical wind velocities are at maximum 1.5 m/s, the variance is about 0.25 $\mathrm{m^2/s^2}$, as indicated by the standard deviation in Fig. 3.2. Compared to the measurements listed above, the KMCM wind amplitudes are significantly smaller. However, the important question is, on which time scales dominant upward or downward

motions persist, as the short time scales (5 min to 30 min) contribute the most to the total vertical wind variance (e.g. Rüster and Reid, 1990; Fritts et al., 1990; Strelnikova and Rapp, 2011). The MAARSY measurements reveal large scale variations of the wind field, where phases of up and down-welling last up to several hours (Stober et al., 2013). These wind fields are comparable to the KMCM field (Figure 3.3), except for the additional superimposed fluctuations on shorter time scales found in the radar measurements. Similar characteristics are present in the wind fields reported by Höffner and Lautenbach (2009) and to some lesser extent by Mitchell and Howells (1998).

From a theoretical perspective, the perturbations of temperature $\hat{T}$ and vertical wind $\hat{w}$, which are induced by gravity waves, are related via the polarization relation (e.g., Holton, 2004; Geller and Gong, 2010; Fritts et al., 2014)

$$\hat{w} = \frac{\mathrm{i}g\omega}{N^2}\frac{\hat{T}}{T_0} \tag{5.1}$$

with background temperature T_0, gravitational acceleration g, Brunt-Väisälä frequency N and angular frequency of the gravity wave ω. For typical conditions ($T_0 = 130\,\mathrm{K}$, $N = 0.02\,\mathrm{s}^{-1}$, $g = 9.81\,\mathrm{m\,s}^{-2}$) a 10 K temperature amplitude is associated with a vertical wind amplitude of $\hat{w} = 0.83\,\mathrm{m/s}$ or $0.33\,\mathrm{m/s}$ for a 4 h or 10 h wave, respectively. Temperature amplitudes of 10 K are observed, for example, in in-situ temperature profiles (Rapp et al., 2002). In KMCM typical temperature fluctuations at the mesopause are $\hat{T} = 9\,\mathrm{K}$ with wind fluctuations of $\hat{w} = 0.45\,\mathrm{m/s}$ (see Figure 3.2). This agrees very well with the theoretically expected values for waves with periods on the order of 6 h. For a detailed study on the applicability of the polarization relations to mesospheric conditions, see Placke et al. (2013).

Megner et al. (2009) report NLCs at exceptionally high altitudes, which were detected by rocket photometers. The peculiarity of this NLC was that it consisted of large particles (effective radius of 50 nm), which does not comply with the conventional picture of ice particles which grow as they sediment to lower altitudes. They concluded that strong up-welling was necessary for the explanation of their observation. NLCs that existed below the altitude range of supersaturation have been found by Christensen et al. (2016), who combined tomographic measurements of temperature, water vapor and NLCs from the Odin satellite. They found that these ice particles were not able to reach those low altitudes only by sedimentation, but rather needed downward vertical wind velocities on the order of 1 m/s to 3 m/s. Both these studies are examples where observations can only be explained by strong vertical winds.

Instead of directly comparing the vertical wind, the downward progression rate of NLCs can be compared. Early studies as those from Langer (1995) report downward progression rates between 1.8 km/h and 2.6 km/h. Kaifler et al. (2013b) analyzed the progression rate depending on the duration of the NLCs. They find a mean downward

progression rate of 0.3 km/h, which comprises upward and downward motions of NLCs equally. Focusing only on the downward motion (e.g. in their Fig. 3), the predominant rates range between 1.3 km/h and 2.3 km/h. A typical (visible) NLC from the CARMA model (as for example in Fig. 3.6), has a downward progression rate of about 1.8 km/h. This value lies well in the range of the measured downward progression rates.

The following four points summarize the discussion of the vertical wind velocities: (1) Radar observations of the vertical wind velocity show large amplitudes on a regular basis. (2) Vertical wind perturbations in KMCM agree well with those associated with typical temperature perturbations at the summer mesopause. (3) NLC measurements have been reported which can only be explained by the presence of large vertical winds. (4) The downward motion of the modeled NLC, which is mainly determined by the vertical wind, lies well within the range of lidar measurements.

These comparisons are only singular reference points, but nevertheless, they confirm that the vertical wind velocities used in this study are within a reasonable range. The comparison with the work of Kiliani et al. (2013) shows to which extent the vertical wind influences the development of NLCs. They studied the temporal evolution of NLCs using the Leibniz-Institute Middle Atmosphere (LIMA) model with the Lagrangian ice transport model LIMA/ICE. Their ice particles reside at approximately their nucleation altitude for more than two days, before they progress downward at the sedimentation rate of ~ 0.2 km/h. This is in sharp contrast to the CARMA/KMCM simulations, where the ice particles survive only a few wave cycles and the vertical motion is almost solely controlled by the vertical wind (see Figure 5.10). This can be attributed to the significantly smaller vertical velocities in the LIMA model, which range from -0.2 m/s to 0.15 m/s. This is roughly the range reported by Stevens et al. (2010) for monthly mean values of the vertical wind using a mesospheric data assimilation system. As seen above, instantaneous wind amplitudes are much higher than these average values. The importance of the vertical wind velocity on the formation of NLCs was already recognized by Klostermeyer (1998) from a time scale analysis.

The main question of this chapter was to what extent the properties of mesospheric ice particles are governed by the nucleation rate. It is found that the nucleation rate is indeed a crucial factor, but nevertheless 'suitable' dynamical conditions are a prerequisite for the development of detectable NLCs. Suitable dynamical conditions are those where ice particles are able to remain in the supersaturated altitude region until they grow to detectable sizes. This is for example given in the climatological background fields, where the mean vertical wind is directed upward and counteracts sedimentation. However, in the wave driven simulations it is not the mean vertical wind which determines the NLC development. It is rather the variability of the vertical wind, which imposes additional constraints on the growth of mesospheric ice particles. The high sensitivity to the vertical velocity is the main conclusions to be drawn from Fig. 5.9 and the trajectories presented in Fig. 5.10.

When using wave driven background profiles, the exact calculation of the microphysical processes becomes essential. The duration of ice particle growth is limited and the assumption that an existing supersaturation will be considerably depleted is no longer applicable. Thus, when going from NLC simulations with rather slowly varying or climatological background conditions to more realistic ones, new limitations arise which challenge our current understanding of the microphysical development of NLCs.

It must be kept in mind, that the relevant parameter that is varied in this study is the rate of newly formed ice particles. This is achieved by varying the nucleation rate per particle. Similar results can be achieved by varying the ice nuclei number density. From the CARMA simulations with the MSP profile of Hunten et al. (1980) it is found that the nucleation rate must be reduced by four to five orders of magnitude to yield realistic NLCs. This statement is in a limited range equivalent to saying that in order to model realistic NLCs the MSP number density must be lower than in the profile of Hunten et al. (1980). This interpretation fits well to the results of Megner et al. (2008b), who find that under the influence of meridional transport the number density of MSPs is significantly lower than in the distribution of Hunten et al. (1980). As their profile yields only about 10 MSP per cm^3 that are larger than 1 nm, Megner et al. (2008a) pose the challenging question, whether MSPs can in general provide enough ice nuclei to explain the phenomenon of electron bite-outs (e.g., Ulwick et al., 1988). Strong electron bite-outs occur occasionally in the vicinity of polar mesospheric summer echoes (Blix et al., 2003; Li and Rapp, 2013) and require ice number densities on the order of $10^3\,cm^{-3}$ to be explained (Reid, 1990). Megner et al. (2008a) argue that a nucleus which carries a charge has a significantly reduced critical radius (or even no critical radius at all). Thus, a larger fraction of the MSP population would be available as ice nuclei, which could solve the dilemma of too low ice nuclei number densities. From our CARMA simulations with the profile of Megner et al. (2008b) it is found that ice number densities on the order of several $10^3\,cm^{-3}$ and up to $10^5\,cm^{-3}$ are easily reached. This is because the wave induced temperature fluctuations lower the critical radius dramatically and allow for a large fraction of the MSP size distribution to nucleate (compare Fig. 5.11 with Fig. 5.12). It is therefore concluded that charged ice nuclei are not a necessary prerequisite for the explanation of large ice number densities. Instead, a temperature induced lowering of the critical radius is a possible alternative explanation. This, however, does not question the importance of considering charged MSPs in modeling mesospheric ice particles.

There could be other mechanisms which modify the nucleation or growth of mesospheric ice particles, which are not included in the current CARMA setup. These can either be effects associated with unresolved dynamical properties of the background atmosphere, or further microphysical processes or dependencies not considered by the CARMA microphysics. An example of unresolved dynamics is the variability of the background atmosphere on time scales of less than about 1 h. Rapid fluctuations of the vertical wind with the corresponding vertical displacements and changing saturation conditions

can pose a considerate limitation on the growth process. The overall effect of such small scale variations is yet to be analyzed. An example of a microphysical process which could alter our basic understanding of NLC development is coagulation of the ice particles. This effect is discussed in the following.

The picture of NLC development, obtained from the presented CARMA simulations, suggests that all ice particles which nucleate will eventually contribute to the observable NLC properties. Thus, there is a direct correlation between nucleation conditions and observable ice particle number density. However, effective coagulation of small ice particles could significantly alter this picture. In this case, the ice number density could be reduced during the time the NLC develops, which would lead to low number densities without the requirement of a low nucleation rate. Hence, the observable number densities would be decoupled from the nucleation rate. Furthermore, the ice particle growth rate would be enhanced by coagulation, which would be welcomed since the modeled ice particles remain rather small in the presented simulations. Coagulation would need to be very efficient on time scales of a few hours in order to be relevant. Rapp and Thomas (2006) have shown that the effects of coagulation are negligible even on time scales of 48 h. Nonetheless, if charged ice particles of both polarities are present, the coagulation rate will be increased due to the electrostatic attraction. Gumbel et al. (2003) showed that both polarities can be present under certain conditions, although most conditions are characterized by (partly) negatively charged ice particles because the electron capture rates exceed the capture rates of positive ions. If both polarities occur, then the Brownian coagulation kernel is increased for these oppositely charged particles by a factor of $\lambda_{i,j}/(1-\exp(-\lambda_{i,j}))$ with $\lambda_{i,j} \propto 1/(r_i + r_j)$ (Alonso, 1999). The largest increase of the Brownian coagulation kernel is obtained for small particle radii $r_{i,j}$, e.g., an increase by a factor of 6 for two 1 nm particles, decreasing to a factor of 1.8 for two 10 nm particles. This means that even if oppositely charged particles were present and even if they had sufficient lifetimes, an increase of the coagulation rate by a factor of 6 would not alter the observed NLC properties notably. Based on these estimations and previous studies by Rapp and Thomas (2006) and Turco et al. (1982), coagulation can be ruled out. Therefore, the picture of a direct relation between the nucleation conditions and the observable NLC number densities is not challenged by coagulation.

5.5 Summary

NLC properties are significantly determined by the nucleation conditions, i.e. by the nucleation rate per particle and by the number of available MSPs. Large nucleation rates thereby lead to numerous ice particles, which remain rather small due to limited water vapor, and vice versa for low nucleation rates.

Besides the nucleation rate, also the atmospheric background conditions have a strong impact on the development of NLCs, in particular whether the background atmosphere is described by climatological conditions or whether it is perturbed by waves. The reason is that the mechanisms which limit the growth of these ice particles are different: In climatological backgrounds, the ice particles can consume the available water vapor until the supersaturation is depleted. Until that point is reached, the only limitation is sedimentation, which is partly compensated by the prevailing upward vertical wind. This results in rather long particle lifetimes between several hours and days. In wave driven backgrounds, the lifetime is significantly shorter. The ice particles commonly survive only a few wave cycles, often even only one. The times where ice particles can nucleate and grow are therefore strongly limited. Due to this limitation, the microphysical time scales of nucleation and particle growth gain in importance and determine whether the ice particles grow to detectable sizes or not. This requires exact microphysical modeling of nucleation and subsequent growth. However, our understanding of the nucleation process under mesospheric conditions is poor, concerning the exact nucleation pathway as well as the parameters which determine the nucleation rate quantitatively. Since the nucleation rate determines one of the two critical microphysical time scales, NLC properties strongly depend on the nucleation conditions.

In order for NLC to grow to detectable sizes and have similar properties as those detected by lidar and satellite measurements, the nucleation rate must be reduced compared to standard assumptions of the classical nucleation theory. In case of numerous MSPs, as in the dust profile of Hunten et al. (1980), the nucleation rate must be reduced by four to five orders of magnitude to best match the properties reported from lidar observations (Baumgarten et al., 2008). Given fewer MSPs, as in the profile of Megner et al. (2008b), standard assumptions lead to fairly realistic properties. It is found that the more MSPs are available (e.g., because the critical radius is small), the lower the nucleation rate per particle must generally be for modeling realistic NLCs. Satellite observations and modeled NLCs agree best when the nucleation rate is reduced by two orders of magnitude or more. In particular large particle radii up to 100 nm only develop in simulations with reduced nucleation rates. Larger nucleation rates produce larger number densities of ice particles, which tend to result in very dim NLCs and which often remain below the detection threshold of optical instruments.

The nucleation rate and the wave driven background conditions at the mesopause are equally critical for the formation of NLC: The nucleation rate determines the number density of ice particles, while the dynamical state of the background atmosphere governs the subsequent particle growth. Especially the vertical wind limits the lifetime of mesospheric ice particles and should therefore receive special consideration in forthcoming NLC modelling studies. Additionally, it is found that an additional cooling, as for example caused by tides or planetary waves, is necessary for the formation of bright NLCs.

6 Implications of recent laboratory results

A laboratory experiment has been designed to study the nucleation of MSP analogues under summer mesopause conditions by the Atmospheric Aerosol Research group at the Karlsruhe Institute of Technology (KIT). Their experiment consists of a plasma microwave for generating MSP analogues of various compositions and an ion trap with adjustable saturation conditions. The nucleation and growth of ice particles is measured via their time dependent mass increase, which is detected by a mass spectrometer. Details of the experiment are described by Duft et al. (2015). First results of heterogeneous nucleation of CO_2 measured with this experiment have been published by Nachbar et al. (2016). With this experiment it is possible to determine the desorption energy ΔF_{des} from the amount of adsorbed water on the MSP surface. For typical summer mesopause conditions, a desorption energy of $\Delta F_{\mathrm{des}} = (6.89 \pm 0.3) \cdot 10^{-20}\,\mathrm{J}$ for singly charged iron oxide particles is found (Duft and Nachbar, 2016, private communication). This is about 2.5 times larger than the currently assumed desorption energy. In terms of a nucleation rate prefactor as introduced for the sensitivity studies in Sec. 5.2, this experimentally determined value of ΔF_{des} corresponds to a prefactor of 10^{18}! In other words, the nucleation process of NLCs occurs 18 orders of magnitude faster than so far assumed.

Prefactors larger than 10^{10} have not been considered in the simulations which are analyzed in Ch. 5. From the basic dependencies it can be assumed, that prefactors exceeding 10^{10} lead to even larger ice number densities and accordingly smaller ice particle radii. However, the analysis in Ch. 5 clearly indicates that realistic NLCs can only be modeled if the nucleation rate is reduced compared to standard assumptions. But the laboratory results reveal that nucleation occurs several orders of magnitude faster than expected for standard assumptions. This apparent contradiction immediately raises the question, whether both results are mutually exclusive, or whether they can both contribute to a coherent picture of NLC microphysics.

As discussed in Sec. 2.1.3 and 2.1.4, several of the parameters which determine the nucleation rate are highly uncertain. By experimentally determining the desorption energy, one of the major uncertainties has been removed, but there are many more parameters which can change the nucleation rate by several orders of magnitude. In particular, if the MSPs are warmer than their environment, the nucleation rate will be

reduced by several orders of magnitude according to classical nucleation theory, (see Sec. 2.9). As described in Ch. 4 we expect MSPs to be warmer than the environment, at least for iron rich MSP compositions. Hence, it is likely that this temperature difference has an influence on the nucleation of mesospheric ice particles. Thus, the effect of an enhanced MSP equilibrium temperature is investigated in the following

The setup for all following simulations utilizes the experimentally determined value for the desorption energy and takes into account the MSP equilibrium temperature T_P for calculating the nucleation rate. First, the temperature difference $\Delta T = T_\mathrm{P} - T_\mathrm{A}$ which is necessary to model realistic NLCs, is estimated by assuming a time and radius-independent temperature difference ΔT. Then, in a second set of simulations, the MSP temperature is calculated explicitly for various MSP compositions. The modeled NLCs of both setups are compared to lidar observations.

6.1 Simulations with simplified ΔT profile

In a first, simplified setup, the temperature difference ΔT is assumed to have a typical altitude dependence but is otherwise assumed to be radius independent and constant over time (see Sec. 4.4). The altitude dependence of ΔT is considered by fitting ΔT of a 2 nm MSP composed of $Mg_{0.5}Fe_{0.5}SiO_3$ as a function of altitude. This profile is then scaled to the desired temperature difference ΔT, which is given for the altitude of 87 km (see Fig. 4.5). This is the same approach as for the simulations shown in Fig. 4.6 and 4.7. The temperature difference ΔT at 87 km altitude is varied from 0 K to 20 K in steps of 1 K. For comparing the modeled NLCs to the lidar observations reported by Baumgarten et al. (2008), the same method as in Sec. 5.3.1 is applied, i.e., the NLC backscatter coefficient, mean radius and total number density of the simulated ice particles must fall within one standard deviation of the values reported by Baumgarten et al. (2008). The setup and analysis of these simulations with varying ΔT is comparable to the simulations presented in the previous chapter in the sense that the variation of the prefactor is replaced by the variation of ΔT. The most realistic NLCs, which were previously obtained for low nucleation rate prefactors, are now expected for large values of ΔT.

The values of ΔT, which lead in the simulations to NLCs that match the observations, are marked in Fig. 6.1. The top row indicates the results obtained with the reference KMCM background profile and the MSP size distribution by Megner et al. (2008b). Matching properties for faint NLC are found when the temperature difference is 11 K or more. Weak NLC with realistic properties are obtained when $\Delta T = 14$ K. As in the previous simulations, only faint and weak NLCs develop in the reference background atmosphere, but no medium or strong NLCs. The middle row shows the results for the simulations where the background temperature has been reduced by 5 K. This

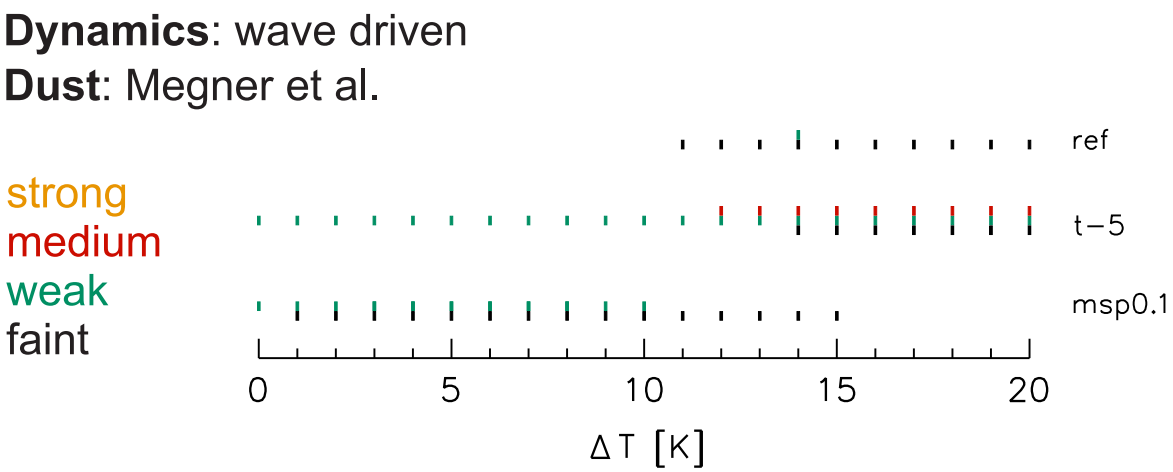

Figure 6.1: Overview over the required temperature difference between MSPs and ambient atmosphere to yield NLCs which match the lidar observations by Baumgarten et al. (2008). (Top) Reference setup with the wave driven KMCM background fields and the MSP profile of Megner et al. (2008b). The dependence on the background fields is demonstrated by evaluating simulations with (middle) reduced mean temperature by 5 K and (bottom) the MSP profile multiplied by 0.1.

temperature offset must not be confused with ΔT, since it refers to the sensitivity to the background atmosphere (e.g., seasonal variation), whereas the latter ΔT refers to the temperature difference between MSPs and the ambient atmosphere. It is found that ΔT has almost no influence when the background atmosphere is 5 K colder than in the reference case. Matching NLCs are found in at least one brightness class for all values of ΔT between 0 K and 20 K. This result agrees very well to the insights gained from Sec. 5.3.1, where it was found that in a colder atmosphere the nucleation rate is not as critical for the development of realistic NLC properties (cf. Fig. 5.7). This tendency is even clearer when the background temperature is reduced by 10 K, which yields matching NLCs in all four brightness classes and all considered values of ΔT (not shown). The last row of Fig. 6.1 shows the matching values of ΔT when the MSP number density is reduced to 0.1 times the original number density. Here the matching NLCs are found for values of ΔT between 0 K and 15 K, which are smaller values of ΔT than in the reference case. This can be explained similar to the inverse relationship found in Fig. 5.6: The lower MSP number density in the 'msp0.1' simulation can partly be compensated by a higher nucleation rate per particle in order to yield the optimum ice number density. In these simulations, a higher nucleation rate per particle is obtained for lower values of ΔT. In comparison to Fig. 5.6, it is therefore plausible that matches down to $\Delta T = 0$ K are found in the last row of Fig. 6.1.

6.2 Simulations with explicit ΔT for different MSP compositions

The equilibrium temperature of MSPs depends on their absorption properties. Thus, the resulting temperature difference $\Delta T = T_\mathrm{P} - T_\mathrm{A}$ is characteristic for the MSP composition. The temperature difference ΔT, required for the simulation of realistic NLCs, was estimated from the simplified simulations to be between 10 K and 20 K (see Fig. 6.1). Table 4.1 indicates that values of ΔT between 10 K and 20 K are found for example for (magnesio-)wuestite particles. Thus, (magnesio-)wuestite could be a possible MSP composition, which reduces the nucleation rate by the optimal factor to lead to NLCs with realistic properties. In the following, different MSP compositions are analyzed to assess their feasibility to yield realistic NLCs, when the model accounts for their increased equilibrium temperature and the experimentally determined desorption energy.

Different from the simulations with the constant ΔT profile, a new set of simulations is generated with the explicit calculation of the equilibrium temperature in each time step for each altitude and size bin. The explicit calculations in each time step are necessary since the background temperature given by the KMCM is time dependent and thus influences the MSP equilibrium temperature in each time step differently. The simulations are performed for all MSP materials given in Tab. 4.1. The NLC properties obtained by these simulations are compared to the lidar observations reported by Baumgarten et al. (2008) (see Sec. 5.3.1 for details) and the results are summarized in Tab. 6.1.

The colored boxes in Tab. 6.1 indicate that matching properties were found for NLCs modeled with the given composition. The different colors refer to the four brightness classes: black for faint NLCs, green for weak NLCs, red for medium NLCs, and yellow for bright NLCs, following the style of previous evaluations. The full range of sensitivities as in Fig. 5.6, 5.7, and 5.9 was analyzed. Nevertheless, the table is limited to characteristic results, which are the results for the reference setup (ref), the setup with reduced MSP number density ('msp0.1') and reduced background temperature ('t-5'). These are the same sensitivities as the ones shown in Fig. 6.1 for the simplified ΔT profile. The fifth column of Tab. 6.1 shows the percentage of SOFIE observations which could be explained by the modeled properties of MSP-ice mixtures. These values are reproduced from Hervig et al. (2012). The MSP compositions are listed in the same order as in Tab. 4.1. This means, that MSP compositions which have a higher equilibrium temperature are found at the top of the table, while MSPs which acquire a lower equilibrium temperature reside at the lower part of Tab. 6.1. In terms of the nucleation rate J, this translates to an increasing J for compositions further down in the table. This tendency is indicated by the arrows in the last column: highest ΔT

and lowest J at the top of the table, lowest ΔT and highest J at the bottom of the table.

The results from the simulations with the reference setup indicate that matching NLC properties are found for (magnesio-)wuestite MSPs, hematite MSPs and MSPs composed of $Mg_{0.8}Fe_{1.2}SiO_3$. These are iron rich compositions which are characterized by a high equilibrium temperature. As argued above, matches are expected for those iron rich materials, because the simplified simulations indicate that a rather large temperature difference of more than $\Delta T = 10\,\mathrm{K}$ is necessary to compensate the larger desorption energy. Strikingly, the matching MSP compositions are exactly those compositions, which showed the highest percentage of matches with the SOFIE observations. It is interesting to note, that carbon MSPs do not result in NLCs with matching properties, even though they are typically even warmer than for example wuestite MSPs.

In the simulations with reduced MSP number density, matches are found for MSP compositions which have a lower equilibrium temperature compared to the matches found in the reference simulations. In particular, weak NLCs, indicated by the green box, are found even for the magnesium silicates which have a ΔT on the order of 0.1 K and therefore the largest nucleation rate of all compositions listed in Tab. 6.1. These results are directly comparable to the previous simulations with reduced MSP number density, which yielded realistic NLCs up to prefactors of 10^{10} (Fig. 5.6), or values of ΔT down to 0 K (Fig. 6.1). From the simulations with reduced background temperature it is found that the nucleation conditions which lead to realistic NLCs are not as restricted when the background atmosphere is colder. In the simulations with a 5 K lower background temperature ('t-5'), matching NLC properties are found for all MSP compositions. Medium bright NLCs are only generated in simulations with carbon MSPs, strong NLCs do not occur in this set of simulations.

6.3 Discussion

The desorption energy of iron oxide MSP analogues, recently determined in laboratory experiments, leads to a nucleation rate which is 18 orders of magnitude larger than currently assumed. On the contrary, the results presented in Ch. 5 show that the nucleation rate must be reduced by a few orders of magnitude compared to standard assumptions in order to model realistic NLCs. These two results seem to stand in direct contradiction.

However, as shown in Sec. 4, MSPs are likely to be warmer than the ambient atmosphere by several Kelvin, which reduces the nucleation rate in the classical approach by several orders of magnitude. This reduction of the nucleation rate partly compensates the effect of the significantly larger desorption energy. Thus, the combination of both effects in CARMA can result in nucleation conditions which lead to realistic NLCs.

MSP composition	NLC matching lidar observations ref	msp0.1	t-5	SOFIE matches [%]	Tendency
Carbon					
C				85/76	
(Magnesio-)Wuestite					
FeO				82/73	
$Mg_{0.1}Fe_{0.9}O$				82/74	
$Mg_{0.2}Fe_{0.8}O$				81/72	
$Mg_{0.3}Fe_{0.7}O$				82/73	
$Mg_{0.5}Fe_{0.5}O$				75/67	
$Mg_{0.6}Fe_{0.4}O$				65/56	
Hematite					
Fe_2O_3				39/30	
Olivines					
$Mg_{0.8}Fe_{1.2}SiO_4$				14/23	ΔT
$MgFeSiO_4$4				13/22	
$Mg_{1.9}Fe_{0.1}SiO_4$				1/4	
Pyroxenes					
$Mg_{0.4}Fe_{0.6}SiO_3$				3/9	
$Mg_{0.5}Fe_{0.5}SiO_3$				3/12	J
$Mg_{0.6}Fe_{0.4}SiO_3$				9/18	
$Mg_{0.7}Fe_{0.3}SiO_3$				8/16	
$Mg_{0.8}Fe_{0.2}SiO_3$				7/15	
$Mg_{0.95}Fe_{0.05}SiO_3$				–	
$MgSiO_3$				–	
Magnesium Silicates					
$Mg_{1.5}SiO_{3.5}$				1/4	
Mg_2SiO_4				1/3	
$Mg_{2.4}SiO_{4.4}$				1/3	
$MgSiO_3$				0/3	
$Mg_{0.7}SiO_{2.7}$				1/2	

Table 6.1: (see right page)

Adopting only the results from the recent laboratory experiments would lead to too many ice particles, which would all remain too small. Considering only the equilibrium temperature of MSPs and the modified nucleation theory would lead to too few ice particles. Thus, when the recent laboratory results are adopted for microphysical simulations of NLCs, the combination of both effects is necessary to model realistic NLCs. It was hypothesized in the introduction of this thesis, that MSPs should be rather poor ice nuclei due to their capability to absorb solar radiation and acquire an increased equilibrium temperature; now it is found that exactly this heating is a prerequisite for modeling NLCs with realistic properties.

From the results presented above it is found that in particular iron rich MSP compositions like (magnesio-)wuestite and hematite are suitable ice nuclei. These are exactly those MSP compositions which were identified by Hervig et al. (2012) to be compatible with SOFIE satellite observations, under the assumption that the mesospheric ice particles contain various volume fractions of MSPs. Their analysis is based on extinction measurements at several wavelengths in combination with modeling of the optical properties of MSP-ice mixtures. The results obtained in this thesis are based on microphysical modeling of ice particle nucleation and subsequent growth using the latest laboratory results. Both approaches specify possible MSP compositions, but with completely independent methods. Yet, they yield coherent conclusions. This is a very promising result which warrants further research into this direction.

The KMCM background temperature, which is used in this study, is representative of the beginning and the end of the NLC season in the northern hemisphere. At the peak of the NLC season the background atmosphere is typically 5 K colder. This seasonal dependence is accounted for with the sensitivity simulation 't-5', where the temperature is reduced by 5 K. However, in this set of simulations, a clear identification of possible ice nuclei compositions is not possible. All of the analyzed compositions lead to realistic NLC properties. This is a clear restriction of the conclusion, that

Table 6.1: Overview over MSP compositions which lead to NLCs similar to lidar observations. Colored boxes indicate for which NLC brightness class the matching properties are found (black: faint NLCs, green: weak NLCs, red: medium NLCs, yellow: strong NLCs). The matches for the reference setup (ref) are shown, for the setup with MSP number density multiplied by 0.1 (msp0.1), and for the setup with background temperature reduced by 5 K (t-5). The fifth column shows the percentage of SOFIE observations which agree with the optical properties of ice-MSP mixtures of the given composition (reproduced from Hervig et al., 2012). The two numbers refer to assumed axis ratios of 2 and 6. The last column indicates the microphysical tendency of the materials: The largest values for ΔT are found at the top of the table, which corresponds to low nucleation rates.

only the iron-rich MSPs are suitable ice nuclei. It implies that at the peak of the NLC season, all analyzed MSP compositions are equally well suited ice nuclei. Note, however, that Hervig et al. (2012) performed their analysis with the SOFIE observations in the southern hemisphere, which is characterized by a slightly warmer mesopause region compared to the northern hemisphere mesopause region (Hervig and Siskind, 2006; Hervig et al., 2013). Based on the discussion above, it is consistent with the modeling results that only iron rich materials are observed in the slightly warmer southern hemisphere throughout the complete NLC season. Even though the 't-5' simulations imply that all analyzed MSP compositions are equally well suited ice nuclei, the simulations do not allow any conclusions on the simultaneous nucleation of many different MSP materials.

The MSP compositions, which lead to matching NLCs, vary with background temperature. This dependence offers a possibility to validate the modeling results. Assuming that the MSPs identified by SOFIE are embedded in the ice particles because they once served as ice nuclei, the composition of the embedded MSPs could depend on the background temperature. The MSP compositions identified by SOFIE could then correlate with variations in the background temperature, such as seasonal, latitudinal, or planetary wave induced temperature variations or inter-hemispheric differences. It should be tested whether the MSP compositions identified by SOFIE change with changing background temperature. The simplest approach would be to repeat the analysis of Hervig et al. (2012) for observations of the northern hemisphere. Since lower temperatures are reached in the northern hemisphere mesopause region, the NLC properties should be less sensitive to the nucleation rate (see 't-5' simulations in Ch. 5 and 6) and consequently also less sensitive to the MSP material. If the MSP composition identified by SOFIE changes throughout the NLC season, this result would confirm the results presented in this chapter. If again only iron rich compositions are found, other compositions of ice nuclei might not be present at the polar summer mesopause. If other, non iron containing materials are found throughout the NLC season, this result could hint at further and so far unconsidered microphysical processes. Such an analysis would be a very meaningful and rigorous test, being probably capable of confirming or revising our current understanding of mesospheric ice formation. This holds of course only for the case that MSPs of different compositions are actually present in the mesosphere and that the ice impurities identified by SOFIE are the ice nuclei and not MSPs collected by the growing ice particles.

6.4 Summary

Recent laboratory experiments showed that the desorption energy of iron oxide MSP analogues is larger by a factor of 2.5 compared to previous assumptions. Using the classical nucleation theory described in Sec. 2.1.4, this larger desorption energy increases

the nucleation rate by 18 orders of magnitude. On the contrary, the conclusion from Ch. 5 was that the nucleation rate must be reduced compared to standard assumptions in order model realistic NLCs. These two opposing results can nonetheless be combined into a coherent picture of NLC formation, when the MSP equilibrium temperature is included in the nucleation rate. A temperature difference ΔT between MSPs and ambient atmosphere significantly reduces the nucleation rate. This reduction is able to partly compensate the dramatic increase of the nucleation rate due to the higher desorption energy.

From simplified simulations with a prescribed profile of ΔT, it is found that the MSPs must be warmer by 10 K or more to yield NLCs which are similar to lidar observations. An equilibrium temperature with ΔT of about 10 K or more is only obtained for iron rich MSP compositions, such as (magnesio-)wuestite or hematite. Indeed, when including the full calculation of the equilibrium temperature in the model, these MSP compositions lead to NLCs with realistic properties. In this sense, the best suited MSP compositions are (magnesio-)wuestite and hematite. It is noteworthy, that according to satellite observations, these are exactly the MSP compositions which are embedded in mesospheric ice particles.

In a generally colder atmosphere, the nucleation conditions which yield realistic NLCs are not as restricted. Therefore, also other MSP compositions which are characterized by lower equilibrium temperatures ($\Delta T < 10$ K) can lead to NLCs with realistic properties. This sensitivity to the background temperature offers a possibility to test the modeling results and conclusion against observations: With varying background temperature (e.g., during the NLC season) the composition of MSPs embedded in the mesospheric ice particles could change. Based on the modeling results, only iron rich MSPs (or MSPs with $\Delta T > 10$ K) should be embedded in the ice particles in warm periods, while during colder periods a greater variety of MSP compositions is possible.

7 Summary

Noctilucent Clouds (NLCs) are a summer phenomenon caused by ice particles in the polar mesosphere. The nucleation of mesospheric ice particles, i.e. the initial ice formation, is a major process of the life cycle of NLCs. Yet, the nucleation process is not well understood. While it is commonly assumed that nucleation occurs on meteoric smoke particles (MSPs), it is hypothesized at the beginning of this thesis, that MSPs are actually poor ice nuclei. It is hypothesized that MSPs have an equilibrium temperature which is higher than the ambient air temperature and that the resulting temperature difference impedes the nucleation of mesospheric ice particles on MSPs.

This hypothesis was assessed by microphysical modeling of mesospheric ice particles, explicitly taking into account the equilibrium temperature of MSPs and further uncertainties in the nucleation rate. The Community Aerosol and Radiation Model for Atmospheres (CARMA) was used to conduct the simulations. The following three constituents are included in CARMA: MSPs, ice particles and water vapor. Their interactions are calculated based on the atmospheric conditions, which are prescribed by either climatological or wave-driven background fields. CARMA has been extended to determine the equilibrium temperature of MSPs. Additionally, classical nucleation theory of heterogeneous nucleation was modified to account for a temperature difference between MSPs and the ambient gas. With this theory and the extended CARMA model, the hypothesis was evaluated with the help of the four research questions stated in the introduction. These questions are answered in the following.

Q1: What is the equilibrium temperature of meteoric smoke particles?

MSPs are in thermal equilibrium between absorption of solar and terrestrial radiation, and emission of infrared radiation as well as energy transfer by collisions with the ambient air. Because the energy sinks are rather ineffective, the MSPs have an equilibrium temperature T_P which is higher than the temperature of the ambient air T_A. The temperature difference $\Delta T = T_\mathrm{P} - T_\mathrm{A}$ strongly depends on the composition of the MSPs. The highest temperature difference is obtained for those MSP compositions which are highly absorbing in the visible wavelength range. Examples for strongly absorbing MSP materials are compositions like (magnesio-) wuestite and hematite, which have a large iron content. For typical conditions at the mesopause, a 1.1 nm MSP

composed of wuestite has a ΔT of 14 K. Weakly absorbing and iron free MSP materials, like magnesium silicates, show almost no increase of the equilibrium temperature.

Q2: How is the nucleation rate affected by possibly warmer ice nuclei?

The effect of a temperature difference ΔT on the nucleation rate is twofold: a positive ΔT leads (1) to an increase of the critical radius and (2) to an increase of the energy barrier associated with the phase change from water vapor to ice. The increase of the critical radius reduces the number of available ice nuclei because only those MSPs which are larger than the critical radius can act as nuclei for mesospheric ice particles. The increase of the energy barrier leads to a reduction of the nucleation rate. For typical conditions at the mesopause and a ΔT of 3 K, the critical radius is increased from 1.1 nm to 1.5 nm and the nucleation rate of a 2 nm MSP is reduced by four orders of magnitude.

Q3: Does the nucleation rate have an influence on the observable NLC properties? Can the nucleation rate be constrained by comparing modeled NLC properties with NLC properties derived from observations?

The microphysical properties of mesospheric ice particles, which are typically derived from observations, are ice particle number density and mean radius. The ice number density is directly determined by the nucleation rate during a nucleation event. The mean radius is determined by the subsequent growth of the ice particles. Because the water vapor in the mesopause region is limited, the maximum radius is inversely related to the ice number density: large ice particle radii can only develop if the ice number density is low, whereas a larger ice number density results in smaller ice particle radii. Thus, the nucleation rate directly influences the ice number density and, due to the limited amount of available water vapor, indirectly the mean radius of the ice particles. This simple relationship holds as long as all ice particles in a NLC experience equal growth conditions, which is the case when the main transport is by the vertical wind and not by diffusion or sedimentation.

NLCs were modeled in wave driven background fields with a variable prefactor for the nucleation rate (i.e. a scaling factor), which was varied over ± 10 orders of magnitude. The properties of the modeled NLCs were then compared to lidar and satellite observations. The modeled NLCs agree best with lidar observations in terms of ice number density, mean radius and brightness when the nucleation rate is reduced by up to three orders of magnitude compared to standard assumptions. The range of ice number densities and mean radii observed by satellites is covered best by the simulations where the nucleation rate is reduced by two orders of magnitude or more. The comparison with the lidar and satellite observations both indicate that the

nucleation rate must be reduced compared to standard assumptions in order to model NLCs with realistic properties.

Q4: Are these results consistent with laboratory experiments examining ice nucleation on MSPs?

The nucleation of MSP analogues under realistic mesospheric conditions was recently examined in laboratory experiments. If the ambient conditions allow for nucleation to take place, it was found that nucleation happens rapidly. One of the critical parameters of the nucleation rate, the desorption energy ΔF_{des}, was experimentally determined. This new value of the desorption energy leads to a nucleation rate which is 18 orders of magnitude larger than the currently assumed nucleation rate of mesospheric ice particles. This is in apparent contradiction to the modeling results, which led to the conclusion that the nucleation rate must be reduced to yield realistic NLC properties.

This apparent contradiction can be resolved by combining both effects in the simulations, i.e. to include the full calculation of the MSP equilibrium temperature and the experimentally determined desorption energy in the simulation of NLCs. Therefore, simulations including both effects were performed and evaluated. It was shown that both effects can indeed compensate each other. The extremely large nucleation rate based on the laboratory results gradually decreases when the temperature difference ΔT between MSPs and ambient air increases. Since ΔT strongly depends on the MSP composition, not all MSP compositions have the same ability to compensate the large nucleation rate motivated by the laboratory results. NLCs with realistic properties were successfully modeled only with MSPs which consist of iron-rich compositions. These iron-rich compositions are: (magnesio-)wuestites of varying iron content, hematite and an iron rich olivine composition. These are exactly the compositions that were identified by satellite observations to be the most likely candidates for ice impurities explaining observed spectral signatures in ice extinction measurements.

The hypothesis of the thesis as stated in the introduction is: 'MSPs acquire a higher equilibrium temperature compared to the ambient atmosphere, which inhibits efficient nucleation. MSPs should therefore be poor ice nuclei.'

This hypothesis has to be rejected, because it was shown that even though MSPs are warmer, they are good ice nuclei. The hypothesis is not rejected because the initial assumption was wrong, (the assumption that MSPs must be warmer than the environment), but because the expected consequence could not be confirmed. The laboratory experiments completely revised our understanding of mesospheric ice nucleation. Thus, the expected consequence, namely that a reduction of the nucleation rate would lead to poor ice nuclei, did not prove correct. MSPs are still good ice nuclei, even if they are warmer than the environment. Indeed, the temperature difference

between MSPs and the surrounding atmosphere is not a hindrance for NLC formation, but a prerequisite for modeling NLCs with realistic properties.

The results obtained in this thesis contribute to our understanding of mesospheric ice formation. The presented simulations and the analysis confirm that MSPs can act as ice nuclei and lead to NLCs with realistic properties in microphysical simulations. Furthermore, it was found that not only the initial ice formation is a critical process in the life cycle of mesospheric ice particles, but also the subsequent growth of the ice particles, which is limited by strong vertical winds. For modeling NLCs, in particular with respect to mesospheric trends, it is crucial to correctly represent these microphysical effects. This includes a detailed representation of the nucleation process as well as atmospheric background profiles with realistic temperature and wind perturbations. Otherwise, mesospheric trends are likely not correctly interpreted .

A Appendix

A.1 Changes in CARMA

Changes made in the CARMA code as compared to the version 2.1 used by Rapp and Thomas (2006):

1. A sign error in the parametrization of the surface energy was corrected to agree with Hale and Plummer (1974). As seen in Figure 2.10 the surface tension plays a crucial role for the nucleation rate. With the corrected parametrization, σ is reduced by about 25%. This shifts the critical radius from 1.5 nm to 1.1 nm (background conditions of 130 K, water vapor mixing ratio of 2 ppm and 0.3 Pa).

2. The nucleation rate given by Asmus et al. (2014) is implemented, which allows the particle temperature to be different from the ambient gas temperature. For the case that the particle temperature is equal to the temperature of the surrounding gas the nucleation rate simplifies to the one given by Keesee (1989). The original CARMA version by Rapp and Thomas (2006) included the nucleation rate by Jensen (1989), with a monomer concentration $c_1 = 10^{28}$ cm^{-2} (compare with the now implemented c_1 value given in Sec. 2). This yielded nucleation rates that were higher by roughly 20 orders of magnitude. However, this does not mean, that the generated ice number densities were also larger by 20 orders of magnitude, but rather that the MSP number density was almost instantaneously depleted. As shown in Figure 5.3 the ice number density reaches a limiting value for larger nucleation rates and the NLC properties are not considerably altered by a further increase of J.

3. The prefactor `gro` of the ice particle growth rate is updated every time step to account for changing background conditions.

4. The density of the ice cores, which consist of meteoric dust material, is set to `rhoelem(3)`=2 g/cm^3 in order to match the density of the MSP in the model. This itself does not change the results significantly. However, if `rhoelem(3)` is changed further adjustments have to be made as otherwise the growthrate is reduced by a factor of two: In the subroutine setupbins.f the variable `rhop3(ixyz,ibin,ig)` has to be set to `rhoelem(ienconc(ig))` instead of `rhoelem(ie)`.

5. To ensure that the water vapor concentration stays positive, a retry mechanism similar to the one suggested by Bardeen et al. (2013) was implemented. The basic idea is that the microphysical calculations are repeated with reduced time step if the gas concentration `gc` turns negative. This procedure is repeated until `gc` remains positive throughout the complete time step. If this would require the number of substeps to be larger than `maxsubsteps`, the microphysics are skipped from the substep on before `gc` would turn negative.

A.2 Time constant to reach equilibrium temperature

The calculation of the time constant τ to reach the equilibrium temperature is based on

$$\Delta T = \frac{1}{mc_\mathrm{P}} \Delta Q. \tag{A.1}$$

The change in temperature $\Delta T = T_\mathrm{P} - T_\mathrm{A}$ is thereby related to the added heat ΔQ via the specific heat capacity c_P and mass m of the MSP. This equation is divided by Δt

$$\frac{\Delta T}{\Delta t} = \frac{1}{mc_\mathrm{P}} \frac{\Delta Q}{\Delta t} = \frac{1}{mc_\mathrm{P}} P(T_\mathrm{P}) \tag{A.2}$$

to yield the rate of change in ΔT and ΔQ. The heat energy transferred per time $(\Delta Q/\Delta t)$ is equal to the sum of all power sources and sinks to which the MSP is exposed, which is

$$P(T_\mathrm{P}) = P_\mathrm{sol} + P_\mathrm{ter} - P_\mathrm{col}(T_\mathrm{P}) - P_\mathrm{rad}(T_\mathrm{P}). \tag{A.3}$$

Going to infinitesimal small values of Δt, the left hand side of Eq. A.2 is replaced by the time derivative $\dot{T}_\mathrm{P}$

$$\dot{T}_\mathrm{P} - \frac{1}{mc_\mathrm{P}} P(T_\mathrm{P}) = 0. \tag{A.4}$$

Here it was assumed that the background temperature T_A is constant in time (i.e. $\dot{T}_\mathrm{A} = 0$). Eq. A.4 is an ordinary differential equation of first order. Unfortunately, no direct solution can be found due to the non-linear temperature dependence of $P_\mathrm{rad}(T_\mathrm{P})$ (see Eq. 4.5). To linearize the equation, $P(T_\mathrm{P})$ is approximated by a Taylor expansion up to first order

$$P(T_\mathrm{P}) \approx P(T_\mathrm{A}) + \frac{\mathrm{d}P(T_\mathrm{P})}{\mathrm{d}T_\mathrm{P}} (T_\mathrm{P} - T_\mathrm{A}). \tag{A.5}$$

In the term of $P(T_\mathrm{P})$, only the loss terms depend on T_P and will therefore contribute to $\frac{\mathrm{d}P(T_\mathrm{P})}{\mathrm{d}T_\mathrm{P}}$. The derivative of $P_\mathrm{col}(T_\mathrm{P})$ can easily be calculated

$$\frac{\mathrm{d}P_\mathrm{col}(T_\mathrm{P})}{\mathrm{d}T_\mathrm{P}} = 4\pi r^2 \alpha_\mathrm{therm} \frac{n_\mathrm{gas} v_\mathrm{therm}}{4} k_b \frac{\gamma + 1}{2(\gamma - 1)}, \tag{A.6}$$

however, the derivative of $P_{\mathrm{rad}}(T_{\mathrm{P}})$ has to be approximated.[1] It is found, that for typical conditions at the mesopause, the derivative of $P_{\mathrm{rad}}(T_{\mathrm{P}})$ is much smaller than the derivative of $P_{\mathrm{col}}(T_{\mathrm{P}})$. For example, for hematite and wuestite particles, the derivative of $P_{\mathrm{rad}}(T_{\mathrm{P}})$ is more than two orders of magnitude smaller than the derivative of $P_{\mathrm{col}}(T_{\mathrm{P}})$ and can therefore be neglected in this first order approximation of the time constant.

With the linearization, the differential equation simplifies to

$$\begin{aligned} \dot{T}_{\mathrm{P}} - \frac{1}{mc_{\mathrm{P}}} \left(P(T_{\mathrm{A}}) - a(T_{\mathrm{P}} - T_{\mathrm{A}})\right) &= 0 \\ \dot{T}_{\mathrm{P}} - Q + \frac{a}{mc_{\mathrm{P}}} T_{\mathrm{P}} &= 0 \end{aligned} \tag{A.7}$$

with $a = \frac{\mathrm{d}P_{\mathrm{col}}(T_{\mathrm{P}})}{\mathrm{d}T_{\mathrm{P}}}$ and all constants included in $Q = \frac{1}{mc_{\mathrm{P}}}(P(T_{\mathrm{A}}) + aT_{\mathrm{A}})$. The solution of Eq. A.7 with boundary condition $T_{\mathrm{P}}(0) = T_{\mathrm{A}}$ is

$$\begin{aligned} T_{\mathrm{P}}(t) &= \left(T_{\mathrm{A}} - Q\frac{mc_{\mathrm{P}}}{a}\right) \exp\left(-\frac{a}{mc_{\mathrm{P}}}t\right) + Q\frac{mc_{\mathrm{P}}}{a} \\ &= \frac{P(T_{\mathrm{A}})}{a}\left(1 - \exp\left(-\frac{a}{mc_{\mathrm{P}}}t\right)\right) + T_{\mathrm{A}}. \end{aligned} \tag{A.8}$$

With the mass of the MSP particle $m = 4/3\pi r^3 \rho_{\mathrm{MSP}}$, the time constant $\tau = \frac{mc_{\mathrm{P}}}{a}$ evaluates to

$$\tau = \frac{r\rho_{\mathrm{MSP}} c_{\mathrm{P}}}{3\alpha_{\mathrm{therm}} \frac{n_{\mathrm{gas}} v_{\mathrm{therm}}}{4} k_b \frac{\gamma+1}{2(\gamma-1)}}. \tag{A.9}$$

The equilibrium temperature is

$$\lim_{t\to\infty} T_{\mathrm{P}}(t) = T_{\mathrm{A}} + \frac{P(T_{\mathrm{A}})}{a}. \tag{A.10}$$

Note, that this is the value for the equilibrium temperature which is obtained in the first step of the iteration described by Eq. 4.7.

Figure A.1 shows the function $T_{\mathrm{P}}(t)$ for a MSP particle composed of FeO. The solution of the exact differential equation (Eq. A.4) is given in blue, the approximation achieved by linearizing the equation in green (Eq. A.8). In this example, no difference between the two solutions is identifiable.

[1] If the MSP was a perfect black body, $P_{\mathrm{rad}}(T_{\mathrm{P}})$ would simply be $P_{\mathrm{rad}}(T_{\mathrm{P}}) = 4\pi r^2 \sigma T_{\mathrm{P}}^4$, with the Stefan-Boltzmann constant σ. Since the MSP is not a perfect absorber, this term must be corrected by a factor $\varepsilon(T_{\mathrm{P}})$ which accounts for the absorption characteristics and is in general a function of T_{P} and the MSP material. With this approximation, the derivative of $P_{\mathrm{rad}}(T_{\mathrm{P}})$ is

$$\frac{\mathrm{d}P_{\mathrm{rad}}(T_{\mathrm{P}})}{\mathrm{d}T_{\mathrm{P}}} = 4\pi r^2 \left(4\varepsilon(T_{\mathrm{P}})\sigma T_{\mathrm{P}}^3 + \sigma T_{\mathrm{P}}^4 \frac{\partial}{\partial T_{\mathrm{P}}}\varepsilon(T_{\mathrm{P}})\right).$$

The functions $\varepsilon(T_{\mathrm{P}})$ and $\frac{\partial}{\partial T_{\mathrm{P}}}\varepsilon(T_{\mathrm{P}})$ have been determined numerically for the MSP materials listed in Tab. 4.1.

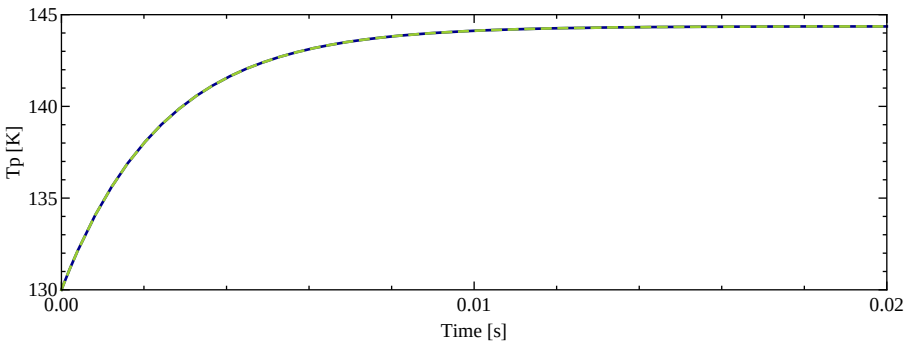

Figure A.1: $T_{\mathrm{P}}(t)$ for a 1.1 nm MSP composed of FeO. The numerical integration of the exact differential equation (see Eq. A.4) is shown in blue, the solution from the linearized equation (Eq. A.8) with τ from Eq. A.9 is shown in green.

Bibliography

Abraham, F. F. (1968). A Reexamination of Homogeneous Nucleation Theory: Thermodynamic Aspects. *J. Atmos. Sci.*, 25, 47. doi:10.1175/1520-0469(1968)025<0047:AROHNT>2.0.CO;2.

Abraham, F. F. and Pound, G. M. (1968). Re-examination of Homogeneous Nucleation Theory: Statistical Thermodynamics Aspects. *J. Chem. Phys.*, 48(2), 732. doi:10.1063/1.1668705.

AIU Jena (2016). Astrophysical Institute and University Observatory Friedrich-Schiller-Universität Jena: Database of Optical Constants for Cosmic Dust.

Alonso, M. (1999). Simultaneous charging and Brownian coagulation of nanometre aerosol particles. *Journal of Physics A: Mathematical and General*, 32(8), 1313.

Asmus, H., Wilms, H., Strelnikov, B., and Rapp, M. (2014). On the heterogeneous nucleation of mesospheric ice on meteoric smoke particles: Microphysical modeling. *J. Atmos. Sol. Terr. Phy.*, 118, 180 – 189. doi:10.1016/j.jastp.2014.03.009.

Backhouse, T. W. (1885). The luminous cirrus cloud of June and July. *Meteor. Mag.*, 20, 133.

Bardeen, C. G., Gettelman, A., Jensen, E. J., Heymsfield, A., Conley, A. J., Delanoë, J., Deng, M., and Toon, O. B. (2013). Improved cirrus simulations in a general circulation model using CARMA sectional microphysics. *J. Geophys. Res.*, 118, 11679 – 11697. doi:10.1002/2013JD020193.

Bardeen, C. G., Toon, O. B., Jensen, E. J., Hervig, M. E., Randall, C. E., Benze, S., Marsh, D. R., and Merkel, A. (2010). Numerical simulations of the three-dimensional distribution of polar mesospheric clouds and comparisons with Cloud Imaging and Particle Size (CIPS) experiment and the Solar Occultation For Ice Experiment (SOFIE) observations. *J. Geophys. Res.*, 115, D1024. doi:10.1029/2009JD012451.

Bardeen, C. G., Toon, O. B., Jensen, E. J., Marsh, D. R., and Harvey, V. L. (2008). Numerical simulations of the three-dimensional distribution of meteoric dust in the mesosphere and upper stratosphere. *J. Geophys. Res.*, 113, D17202. doi:10.1029/2007JD009515.

Baumgarten, G., Chandran, A., Fiedler, J., Hoffmann, P., Kaifler, N., Lumpe, J., Merkel, A., Randall, C. E., Rusch, D., and Thomas, G. (2012). On the horizontal and temporal structure of noctilucent clouds as observed by satellite and lidar at ALOMAR (69N). *Geophys. Res. Lett.*, 39, L01803. doi:10.1029/2011GL049935.

Baumgarten, G., Fiedler, J., Lübken, F.-J., and Cossart, G. v. (2008). Particle properties and water content of noctilucent clouds and their interannual variation. *J. Geophys. Res.*, 113(D6). doi:10.1029/2007JD008884.

Baumgarten, G., Fiedler, J., and Rapp, M. (2010). On microphysical processes of Noctilucent Clouds (NLC): Observations and modeling of mean and width of the particle size-distribution. *Atmos. Chem. Phys.*, 10, 6661–6668. doi:10.5194/acp-10-6661-2010.

Baumgarten, G., Fricke, K. H., and von Cossart, G. (2002). Investigation of the shape of noctilucent cloud particles by polarization lidar technique. *Geophys. Res. Lett.*, 29(13), 8–1/4. doi:10.1029/2001GL013877.

Baumgarten, G. and Fritts, D. C. (2014). Quantifying Kelvin-Helmholtz instability dynamics observed in noctilucent clouds: 1. Methods and observations. *J. Geophys. Res.*, 119, 9324–9337. doi:10.1002/2014JD021832.

Becker, E. (2009). Sensitivity of the Upper Mesosphere to the Lorenz Energy Cycle of the Troposphere. *J. Atmos. Sci.*, 66, 647–666. doi:10.1175/2008JAS2735.1.

Becker, E. and Burkhardt, U. (2007). Nonlinear Horizontal Diffusion for GCMs. *Mon. Wea. Rev.*, 135(4), 1439–1454. doi:10.1175/mwr3348.1.

Becker, R. and Döring, W. (1935). Kinetische Behandlung der Keimbildung in übersättigten Dämpfen. *Ann. Phys-Berlin*, 5(24), 719–752.

Berger, U. and Zahn, U. v. (2002). Icy particles in the summer mesopause region: Three-dimensional modeling of their environment and two-dimensional modeling of their transport. *J. Geophys. Res.*, 107(A11). doi:10.1029/2001JA000316.

Bhattacharya, Y. and Gerrard, A. J. (2010). Wintertime mesopause region vertical winds from Resolute Bay. *J. Geophys. Res.*, 115. doi:10.1029/2010jd014113.

Bird, G. (1988). Aerodynamic effects on atmospheric composition measurements from rocket vehicles in the thermosphere. *Planet. Space Sci.*, 36(9), 921–926. doi:10.1016/0032-0633(88)90099-2.

Blander, M. and Katz, J. L. (1972). The thermodynamics of cluster formation in nucleation theory. *J. Stat. Phys.*, 4(1), 55–59. doi:10.1007/BF01008471.

Blix, T., Rapp, M., and Lübken, F.-J. (2003). Relations between small scale electron number density fluctuations, radar backscatter, and charged aerosol particles. *J. Geophys. Res.*, 108(D8), 8450. doi:10.1029/2002JD002430.

Bohren, C. F. and Huffman, D. R. (1983). *Absorption and Scattering of Light by Small Particles*. New York: John Wiley & Sons.

Bowles, R. K., Reguera, D., Djikaev, Y., and Reiss, H. (2001). A theorem for inhomogeneous systems: The generalization of the nucleation theorem. *J. Chem. Phys.*, 115(4), 1853. doi:10.1063/1.1382818.

Brown, D. E., George, S. M., Huang, C., Wong, E. K. L., Rider, K. B., Smith, R. S., and Kay, B. D. (1996). H_2O Condensation Coefficient and Refractive Index for Vapor-Deposited Ice from Molecular Beam and Optical Interference Measurements. *J. Phys. Chem.*, 100(12), 4988–4995. doi:10.1021/jp952547j.

Byers, H. R. (1965). *Elements of Cloud Physics*. University of Chicago Press.

Ceplecha, Z., Borovička, J., Elford, W. G., ReVelle, D. O., Hawkes, R. L., Porubčan, V., and Šimek, M. (1998). Meteor Phenomena and Bodies. *Space Sci. Rev.*, 84(3/4), 327–471. doi:10.1023/a:1005069928850.

Chandran, A., Rusch, D. W., Palo, S. E., Thomas, G. E., and Taylor, M. J. (2009). Gravity wave observations in the summertime polar mesosphere from Cloud Imaging and Particle Size (CIPS) experiment on the AIM spacecraft. *J. Atmos. Sol. Terr. Phy.*, 71, 392–400. doi:10.1016/j.jastp.2008.09.041.

Chandran, A., Rusch, W., Thomas, G. E., Palo, S. E., Baumgarten, G., Jensen, E. J., and Merkel, A. W. (2012). Atmospheric gravity wave effects on polar mesospheric clouds: A comparison of numerical simulations from CARMA 2D with AIM observations. *J. Geophys. Res.*, 117, D20104. doi:10.1029/2012JD017794.

Christensen, O. M., Benze, S., Eriksson, P., Gumbel, J., Megner, L., and Murtagh, D. P. (2016). The relationship between Polar Mesospheric Clouds and their background atmosphere as observed by Odin-SMR and Odin-OSIRIS. *Atmos. Chem. Phys. Dis.*, 2016, 1–23. doi:10.5194/acp-2016-268.

Clemesha, B. R., Kirchhoff, V. W. J. H., Simonich, D. M., and Takahashi, H. (1978). Evidence of an extra-terrestrial source for the mesospheric sodium layer. *Geophys. Res. Lett.*, 5(10), 873–876. doi:10.1029/gl005i010p00873.

Colella, P. and Woodward, P. R. (1984). The Piecewise Parabolic Method (PPM) for Gas-Dynamic Simulations. *J. Comput. Phys.*, 54.

DeLand, M. T., Shettle, E. P., Thomas, G. E., and Olivero, J. J. (2006). A quarter-century of satellite polar mesospheric cloud observations. *J. Atmos. Sol. Terr. Phy.*, 68(1), 9–29. doi:10.1016/j.jastp.2005.08.003.

Demissie, T. D., Espy, P. J., Kleinknecht, N. H., Hatlen, M., Kaifler, N., and Baumgarten, G. (2014). Characteristics and sources of gravity waves observed in noctilucent

cloud over Norway. *Atmos. Chem. Phys.*, 14(22), 12133–12142. doi:10.5194/acp-14-12133-2014.

Dorschner, J., Begemann, B., Henning, T., Jaeger, C., and Mutschke, H. (1995). Steps toward interstellar silicate mineralogy. II. Study of Mg-Fe-silicate glasses of variable composition. *Astron. Astrophys.*, 300, 503–520.

Duft, D., Nachbar, M., Eritt, M., and Leisner, T. (2015). A Linear Trap for Studying the Interaction of Nanoparticles with Supersaturated Vapors. *Aerosol Sci. Technol.*, 49(9), 682–690. doi:10.1080/02786826.2015.1063583.

Eidhammer, T. and Havnes, O. (2001). Size dependence of the mesospheric dust temperature And its influence on the noctilucent clouds and polar mesosphere summer echo phenomena. *J. Geophys. Res.*, 106(A11), 24831–24841.

Eremenko, M. N. (2005). Shape and composition of PMC particles derived from satellite remote sensing measurements. *Geophys. Res. Lett.*, 32(16). doi:10.1029/2005GL023013.

Espy, P. and Jutt, H. (2002). Equilibrium temperature of water–ice aerosols in the high-latitude summer mesosphere. *J. Atmos. Sol. Terr. Phy.*, 64(17), 1823–1832.

Fabian, D., Henning, T., Jäger, C., Mutschke, H., Dorschner, J., and Wehrhan, O. (2001). Steps toward interstellar silicate mineralogy. *Astron. Astrophys.*, 378, 228–238. doi:10.1051/0004-6361:20011196.

Fiedler, J., Baumgarten, G., Berger, U., Hoffmann, P., Kaifler, N., and Lübken, F.-J. (2011). NLC and the background atmosphere above ALOMAR. *Atmos. Chem. Phys.*, 11, 5701–5717. doi:10.5194/acp-11-5701-2011.

Fiedler, J., Baumgarten, G., and Lübken, F.-J. (2009). NLC observations during one solar cycle above ALOMAR. *J. Atmos. Sol. Terr. Phy.*, 71(3-4), 424 – 433. doi:10.1016/j.jastp.2008.11.010.

Fiedler, J., Baumgarten, G., and von Cossart, G. (2003). Noctilucent clouds above ALOMAR between 1997 and 2001: Occurrence and properties. *J. Geophys. Res.*, 108(D8), 8453. doi:10.1029/2002JD002419.

Fiedler, J., Baumgarten, G., and von Cossart, G. (2005). Mean diurnal variations of noctilucent clouds during 7 years of lidar observations at ALOMAR. *Ann. Geophys.*, 23, 1175 – 1181. doi:10.5194/angeo-23-1175-2005.

Fiocco, G., Grams, G., and Visconti, G. (1975). Equilibrium temperatures of small particles in the Earth's upper atmosphere (50–110 km). *J. Atmos. Terr. Phys.*, 37(10), 1327–1337.

Fletcher, N. H. (1958). Size Effect in Heterogeneous Nucleation. *J. Chem. Phys.*, 29(3), 572–576.

Ford, I. J. (1997). Nucleation theorems, the statistical mechanics of molecular clusters, and a revision of classical nucleation theory. *Phys. Rev. E*, 56(5), 5615 – 5629. doi:10.1103/PhysRevE.56.5615.

Fritts, D. C., Hoppe, U.-P., and Inhester, B. (1990). A study of the vertical motion field near the high-latitude summer mesopause during MAC/SINE. *J. Atmos. Terr. Phys.*, 52(10), 927 – 938. doi:10.1016/0021-9169(90)90025-I.

Fritts, D. C., Pautet, P.-D., Bossert, K., Taylor, M. J., Williams, B. P., Iimura, H., Yuan, T., Mitchell, N. J., and Stober, G. (2014). Quantifying gravity wave momentum fluxes with Mesosphere Temperature Mappers and correlative instrumentation. *J. Geophys. Res.*, 119, 13,583–13,603. doi:10.1002/2014jd022150.

Garcia, R. R., Marsh, D. R., Kinnison, D. E., Boville, B. A., and Sassi, F. (2007). Simulation of secular trends in the middle atmosphere, 1950 – 2003. *J. Geophys. Res.*, 112(D9). doi:10.1029/2006jd007485.

Gelinas, L., Lynch, K., Kelley, M., Collins, S., Baker, S., Zhou, Q., and Friedman, J. (1998). First observation of meteoritic charged dust in the tropical mesosphere. *Geophys. Res. Lett.*, 25(21), 4047–4050.

Geller, M. A. and Gong, J. (2010). Gravity wave kinetic, potential, and vertical fluctuation energies as indicators of different frequency gravity waves. *J. Geophys. Res.*, 115, D11111. doi:10.1029/2009JD012266.

Gibbs, J. W. (1906). *The Scientific Papers of J. Willard Gibbs*. Longmans, Green and co.

Girshick, S. L. and Chiu, C.-P. (1990). Kinetic nucleation theory: A new expression for the rate of homogeneous nucleation from an ideal supersaturated vapor. *J. Chem. Phys.*, 93(2), 1273–1277.

Gombosi, T. I. (1994). *Gaskinetic Theory*. Cambridge: Cambridge University Press.

Gordley, L. L., Hervig, M. E., Fish, C., Russell III, J. M., Bailey, S., Cook, J., Hansen, S., Shumway, A., Paxton, G., Deaver, L., Marshall, T., Burton, J., Magill, B., Brown, C., Thompson, E., and Kempc, J. (2009). The solar occulatation for ice experiment. *J. Atmos. Sol. Terr. Phy.*, 71, 300–315.

Grams, G. and Fiocco, G. (1977). Equilibrium Temperatures of Spherical Ice Particles in the Upper Atmosphere and Implications for Noctilucent Cloud Formation. *J. Geophys. Res.*, 82(6), 961–966.

Gumbel, J. (2001). Aerodynamic influences on atmospheric in situ measurements from sounding rockets. *J. Geophys. Res.*, 106(A6), 10553–10563. doi:10.1029/2000ja900166.

Gumbel, J. and Megner, L. (2009). Charged meteoric smoke as ice nuclei in the mesosphere: Part 1 – A review of basic concepts . *J. Atmos. Sol. Terr. Phy.*, 71(12), 1225 – 1235. doi:10.1016/j.jastp.2009.04.012.

Gumbel, J., Siskind, D. E., Witt, G., Torkar, M., and Friedrich, M. (2003). Influences of ice particles on the ion chemistry of the polar summer mesosphere. *J. Geophys. Res.*, 108(D8). doi:10.1029/2002JD002413.

Gumbel, J. and Witt, G. (2002). Cluster ions and ice particle nucleation: Positive feedback at the summer mesopause. *Geophys. Res. Lett.*, 29(16). doi:10.1029/2002GL015146.

Hale, B. N. and Plummer, P. L. M. (1974). Molecular model for ice clusters in a supersaturated vapor. *J. Chem. Phys.*, 61, 4012 – 4019. doi:10.1063/1.1681694.

Henderson, M. A. (2002). The interaction of water with solid surfaces: fundamental aspects revisited. *Surf. Sci. Rep.*, 46(1-8), 1 – 308. doi:10.1016/S0167-5729(01)00020-6.

Henning, T., Begemann, B., Mutschke, H., and Dorschner, J. (1995). Optical properties of oxide dust grains. *Astron. Astrophys. Suppl.*, 112, 143–149.

Hervig, M. and Siskind, D. (2006). Decadal and inter-hemispheric variability in polar mesospheric clouds, water vapor, and temperature. *J. Atmos. Sol. Terr. Phy.*, 68(1), 30 – 41. doi:10.1016/j.jastp.2005.08.010.

Hervig, M., Thompson, R. E., McHugh, M., Gordley, L. L., Russell III, J. M., and Summers, M. E. (2001). First confirmation that water ice is the primary component of polar mesospheric clouds. *Geophys. Res. Lett.*, 28(6), 971–974. doi:10.1029/2000GL012104.

Hervig, M. E., Berger, U., and Siskind, D. E. (2016). Decadal variability in PMCs and implications for changing temperature and water vapor in the upper mesosphere. *J. Geophys. Res.*, 121(5), 2383–2392. doi:10.1002/2015jd024439.

Hervig, M. E., Deaver, L. E., Bardeen, C. G., Russell III, J. M., Bailey, S. M., and Gordley, L. L. (2012). The content and composition of meteoric smoke in mesospheric ice particles from SOFIE observations. *J. Atmos. Sol. Terr. Phy.*, 84-85, 1–6. doi:10.1016/j.jastp.2012.04.005.

Hervig, M. E. and Gordley, L. L. (2010). Temperature, shape, and phase of mesospheric ice from Solar Occultation for Ice Experiment observations. *J. Geophys. Res.*, 115, D15208. doi:10.1029/2010JD013918.

Hervig, M. E., Gordley, L. L., Deaver, L. E., Siskind, D. E., Stevens, M. H., Russell, J. M., Bailey, S. M., Megner, L., and Bardeen, C. G. (2009a). First Satellite

Observations of Meteoric Smoke in the Middle Atmosphere. *Geophys. Res. Lett.*, 36(18). doi:10.1029/2009GL039737.

Hervig, M. E., Gordley, L. L., Russell III, J. M., and Bailey, S. M. (2009b). SOFIE PMC observations during the northern summer of 2007. *J. Atmos. Sol. Terr. Phy.*, 71, 331 – 339. doi:10.1016/j.jastp.2008.08.010.

Hervig, M. E., Gordley, L. L., Stevens, M. H., Russell III, J. M., Bailey, S. M., and Baumgarten, G. (2009c). Interpretation of SOFIE PMC measurements: Cloud identification and derivation of mass density, particle shape, and particle size. *J. Atmos. Sol. Terr. Phy.*, 71, 316–330. doi:10.1016/j.jastp.2008.07.009.

Hervig, M. E., Siskind, D. E., Stevens, M. H., and Deaver, L. E. (2013). Interhemispheric comparison of PMCs and their environment from SOFIE observations . *J. Atmos. Sol. Terr. Phy.*, 104, 285 – 298. doi:10.1016/j.jastp.2012.10.013.

Höffner, J. and Lautenbach, J. (2009). Daylight measurements of mesopause temperature and vertical wind with the mobile scanning iron lidar. *Opt. Lett.*, 34, 1351 – 1353. doi:10.1364/OL.34.001351.

Holton, J. R. (2004). *An Introduction to Dynamic Meteorology*. International Geophysics Series. Elsevier Academic Press, 4 edition.

Hoppe, U.-P. and Fritts, D. C. (1995). High-resolution measurements of vertical velocity with the European incoherent scatter VHF radar 1. Motion field characteristics and measurement bias. *J. Geophys. Res.*, 100(D8), 16,813 – 16,825.

Hoppe, U.-P. and Hansen, T. L. (1988). Studies of vertical motion in the upper mesosphere using EISCAT UHF radar. *Ann. Geophys.*, 6(2), 181–186.

Hultgren, K. and Gumbel, J. (2014). Tomographic and spectral views on the lifecycle of polar mesospheric clouds from Odin/OSIRIS. *J. Geophys. Res.*, 119(24), 14,129–14,143. doi:10.1002/2014JD022435.

Hultgren, K., Gumbel, J., Degenstein, D., Bourassa, A., Lloyd, N., and Stegman, J. (2013). First simultaneous retrievals of horizontal and vertical structures of Polar Mesospheric Clouds from Odin/OSIRIS tomography. *J. Atmos. Sol. Terr. Phy.*, 104, 213 – 223. doi:10.1016/j.jastp.2013.06.013.

Hunten, D. M., Turco, R. P., and Toon, O. B. (1980). Smoke and Dust Particles of Meteoric Origin in the Mesosphere and Stratosphere. *J. Atmos. Sci.*, 37(6), 1342–1357.

Iland, K., Wölk, J., Strey, R., and Kashchiev, D. (2007). Argon nucleation in a cryogenic nucleation pulse chamber. *J. Chem. Phys.*, 127(15), 154506. doi:10.1063/1.2764486.

Jacobson, M. Z., Turco, R. P., Jensen, E. J., and Toon, O. B. (1994). Modeling coagulation among particles of different composition and size. *Atmos. Environ.*, 28(7), 1327–1338.

Jäger, C., Dorschner, J., Mutschke, H., Posch, T., and Henning, T. (2003). Steps toward interstellar silicate mineralogy. *Astron. Astrophys.*, 408(1), 193–204. doi:10.1051/0004-6361:20030916.

Jäger, C., Mutschke, H., and Henning, T. (1998). Optical properties of carbonaceous dust analogues. *Astron. Astrophys.*, 332, 291–299. doi:10.1051/0004-6361:20030916.

Jensen, E. and Thomas, G. E. (1989). On the diurnal Variation of Noctilucent Clouds. *J. Geophys. Res.*, 94(D12), 14693–14702.

Jensen, E. J. (1989). *A numerical model of polar mesospheric cloud formation and evolution*. PhD thesis, University of Colorado.

Jesse, O. (1885). Auffallende Abenderscheinung am Himmel. *Meteor. Z.*, 2, 311–312.

Jesse, O. (1896). Die Höhe der leuchtenden Nachtwolken. *Astron. Nachr.*, 140(3347), 161–168.

Kaifler, N., Baumgarten, G., Fiedler, J., and Lübken, F.-J. (2013a). Quantification of waves in lidar observations of noctilucent clouds at scales from seconds to minutes. *Atmos. Chem. Phys.*, 13, 7397–7429. doi:10.5194/acp-13-11757-2013.

Kaifler, N., Baumgarten, G., Klekociuk, A. R., Alexander, S. P., Fiedler, J., and Lübken, F.-J. (2013b). Small scale structures of NLC observed by lidar at 69Â°N/69Â°S and their possible relation to gravity waves. *J. Atmos. Sol. Terr. Phy.*, 104, 244–252. doi:10.1016/j.jastp.2013.01.004.

Kalikmanov, V. I. (2013). *Nucleation Theory*. Springer.

Karlsson, B. and Gumbel, J. (2005). Challenges in the limb retrieval of noctilucent cloud properties from Odin/OSIRIS. *Adv. Space Res.*, 36(5), 935–942. doi:10.1016/j.asr.2005.04.074.

Kashchiev, D. (1982). On the relation between nucleation work, nucleus size, and nucleation rate. *J. Chem. Phys.*, 76(10), 5098–5102. doi:10.1063/1.442808.

Kashchiev, D. (2003). Thermodynamically consistent description of the work to form a nucleus of any size. *J. Chem. Phys.*, 118(4), 1837–1851. doi:10.1063/1.1531614.

Kashchiev, D. (2006). Analysis of experimental data for the nucleation rate of water droplets. *J. Chem. Phys.*, 125(4), 044505. doi:10.1063/1.2222373.

Katz, J. L. and Donohue, M. D. (1979). A kinetic approach to homogeneous nucleation theory. In S. A. R. I. Prigogine (Ed.), *Advances in Chemical Physics*, volume 40 (pp. 137–155). John Wiley & Sons, Inc. doi:10.1002/9780470142592.ch3.

Katz, J. L. and Wiedersich, H. (1977). Nucleation theory without Maxwell Demons. *J. Colloid Interface Sci.*, 61(2), 351 – 355. doi:10.1016/0021-9797(77)90397-6.

Keesee, R. G. (1989). Nucleation and Particle Formation in the Upper Atmosphere. *J. Geophys. Res.*, 94(D12), 14683–14692.

Kiliani, J., Baumgarten, G., Lübken, F.-J., and Berger, U. (2015). Impact of particle shape on the morphology of noctilucent clouds. *Atmos. Chem. Phys.*, 15(22), 12897–12907. doi:10.5194/acp-15-12897-2015.

Kiliani, J., Baumgarten, G., Lübken, F.-J., Berger, U., and Hoffmann, P. (2013). Temporal and spatial characteristics of the formation of strong noctilucent clouds. *J. Atmos. Sol. Terr. Phy.*, 104, 151–166. doi:10.1016/j.jastp.2013.01.005.

Kirkwood, S. and Stebel, K. (2003). Influence of planetary waves on noctilucent cloud occurrence over NW Europe. *J. Geophys. Res.*, 108, 8440. doi:10.1029/2002JD002356.

Klostermeyer, J. (1998). A simple model of the ice particle size distribution in noctilucent clouds. *J. Geophys. Res.*, 103(D22), 28743–28752. doi:10.1029/98JD02070.

Koga, K., Zeng, X. C., and Shchekin, A. K. (1998). Validity of Tolman's equation: How large should a droplet be? *J. Chem. Phys.*, 109(10), 4063–4070. doi:10.1063/1.477006.

Körner, U. and Sonnemann, G. R. (2001). Global three-dimensional modeling of the water vapor concentration of the mesosphere-mesopause region and implications with respect to the noctilucent cloud region. *J. Geophys. Res.*, 106, 9639–9651. doi:10.1029/2000JD900744.

Landau, L. D. and Lifshitz, E. M. (1969). *Statistical Physics*. Course of Theoretical Physics. Pergamon Press.

Langer, M. (1995). *Lidarbeobachtungen von leuchtenden Nachtwolken*. PhD thesis, Bonn University.

Lazzati, D. (2008). Non-local thermodynamic equilibrium dust nucleation in subsaturated vapours. *Mon. Not. R. Astron. Soc.*, 384(1), 165–172. doi:10.1111/j.1365-2966.2007.12678.x.

Lee, J. K., Abraham, F. F., and Pound, G. M. (1973). On the validity of the capillarity approximation in the rate theory of homogeneous nucleation. *Surf. Sci.*, 34, 745–758. doi:10.1016/0039-6028(73)90041-1.

Leslie, R. C. (1885). Sky glows. *Nature*, 32(820), 245.

Li, Q. and Rapp, M. (2013). {PMSE} observations with the {EISCAT} vhf- and uhf-radars: Ice particles and their effect on ambient electron densities. *J. Atmos. Sol. Terr. Phy.*, 104, 270 – 276. doi:10.1016/j.jastp.2012.10.015.

Liu, X., Yue, J., Xu, J., Yuan, W., Russell III, J. M., and Hervig, M. E. (2015). Five-day waves in polar stratosphere and mesosphere temperature and mesospheric ice water measured by SOFIE/AIM. *J. Geophys. Res.* doi:10.1002/2015JD023119.

Lothe, J. (1968). Concentration of Clusters in Nucleation and the Classical Phase Integral. *J. Chem. Phys.*, 48(4), 1849. doi:10.1063/1.1668921.

Lothe, J. and Pound, G. M. (1962). Reconsiderations of Nucleation Theory. *J. Chem. Phys.*, 36(8), 2080. doi:10.1063/1.1732832.

Lübken, F.-J. (1997). Seasonal variation of turbulent energy dissipation rates at high latitudes as determined by in situ measurements of neutral density fluctuations. *J. Geophys. Res.*, 102, 13441–13456.

Lübken, F.-J. (1999). Thermal structure of the Arctic summer mesosphere. *J. Geophys. Res.*, 104, 9135 – 9149.

Lübken, F.-J. and Berger, U. (2011). Latitudinal and interhemispheric variation of stratospheric effects on mesospheric ice layer trends. *J. Geophys. Res.*, 116. doi:10.1029/2010jd015258.

Lübken, F.-J., Berger, U., and Baumgarten, G. (2009). Stratospheric and solar cycle effects on long-term variability of mesospheric ice clouds. *J. Geophys. Res.*, 114. doi:10.1029/2009jd012377.

Lübken, F.-J., Berger, U., and Baumgarten, G. (2013). Temperature trends in the midlatitude summer mesosphere. *J. Geophys. Res.*, 118(24), 13,347–13,360.

Lynch, K. A., Gelinas, L. J., Kelley, M. C., Collins, R. L., Widholm, M., Rau, D., MacDonald, E., Liu, Y., Ulwick, J., and Mace, P. (2005). Multiple sounding rocket observations of charged dust in the polar winter mesosphere. *J. Geophys. Res.*, 110(A3). doi:10.1029/2004JA010502.

Määttänen, A., Vehkamäki, H., Lauri, A., Merikallio, S., Kauhanen, J., Savijärvi, H., and Kulmala, M. (2005). Nucleation studies in the Martian atmosphere. *J. Geophys. Res.*, 110, E02002. doi:10.1029/2004JE002308.

Megner, L. (2011). Minimal impact of condensation nuclei characteristics on observable Mesospheric ice properties. *J. Atmos. Sol. Terr. Phy.*, 73, 2184 – 2191. doi:10.1016/j.jastp.2010.08.006.

Megner, L. and Gumbel, J. (2009). Charged meteoric particles as ice nuclei in the mesosphere: Part 2: A feasibility study. *J. Atmos. Sol. Terr. Phy.*, 71(12), 1236 – 1244. doi:10.1016/j.jastp.2009.05.002.

Megner, L., Gumbel, J., Rapp, M., and Siskind, D. (2008a). Reduced meteoric smoke particle density at the summer pole - Implications for mesospheric ice particle nucleation. *Adv. Space Res.*, 41, 41–49. doi:10.1016/j.asr.2007.09.006.

Megner, L., Khaplanov, M., Baumgarten, G., Gumbel, J., Stegman, J., Strelnikov, B., and Robertson, S. (2009). Large mesospheric ice particles at exceptionally high altitudes. *Ann. Geophys.*, 27(3), 943–951. doi:10.5194/angeo-27-943-2009.

Megner, L., Siskind, D. E., Rapp, M., and Gumbel, J. (2008b). Global and temporal distribution of meteoric smoke: A two-dimensional simulation study. *J. Geophys. Res.*, 113, D03202. doi:10.1029/2007JD009054.

Meinen, J., Eritt, M., Habig, J. C., and Leisner, T. (2012). Optical properties of free sub-10-nm diameter Fe2O3 nanoparticles studied by broad-band cavity enhanced absorption spectroscopy (BB-CEAS). *App. Phys. B*, 108(3), 641–647. doi:10.1007/s00340-012-5044-3.

Merkel, A. W., Garcia, R. R., Bailey, S. M., and Russell III, J. M. (2008). Observational studies of planetary waves in PMCs and mesospheric temperature measured by SNOE and SABER. *J. Geophys. Res.*, 113, D14202. doi:10.1029/2007JD009396.

Merkel, A. W., Marsh, D. R., Gettelman, A., and Jensen, E. J. (2009). On the relationship of polar mesospheric cloud ice water content, particle radius and mesospheric temperature and its use in multi-dimensional models. *Atmos. Chem. Phys.*, 9, 8889–8901.

Merkel, A. W., Thomas, G. E., Palo, S. E., and Bailey, S. M. (2003). Observations of the 5-day planetary wave in PMC measurements from the Student Nitric Oxide Explorer Satellite. *Geophys. Res. Lett.*, 30, 1196–1199.

Mishchenko, M. I. and Travis, L. D. (1998). Capabilities and limitations of a current FORTRAN implementation of the T-matrix method for randomly oriented, rotationally symmetric scatterers. *J. Quant. Spectrosc. Radiat. Transfer*, 60(3), 309 – 324.

Mitchell, N. J. and Howells, V. S. C. (1998). Vertical velocities associated with gravity waves measured in the mesosphere and lower thermosphere with the EISCAT VHF radar. *Ann. Geophys.*, 16(10), 1367–1379. doi:10.1007/s00585-998-1367-0.

Murray, B. J. and Jensen, E. J. (2010). Homogeneous nucleation of amorphous solid water particles in the upper mesosphere. *J. Atmos. Sol. Terr. Phy.*, 72(1), 51–61.

Murray, B. J., Malkin, T. L., and Salzmann, C. G. (2015). The crystal structure of ice under mesospheric conditions. *J. Atmos. Sol. Terr. Phy.*, 127, 78–82. doi:10.1016/j.jastp.2014.12.005.

Nachbar, M., Duft, D., Mangan, T. P., Martin, J. C. G., Plane, J. M. C., and Leisner, T. (2016). Laboratory measurements of heterogeneous CO2 ice nucleation on nanoparticles under conditions relevant to the Martian mesosphere. *Journal of Geophysical Research: Planets*. doi:10.1002/2015JE004978.

Obeidat, A., Li, J.-S., and Wilemski, G. (2004). Nucleation rates of water and heavy water using equations of state. *J. Chem. Phys.*, 121(19), 9510. doi:10.1063/1.1806400.

Pautet, P.-D., Stegman, J., Wrasse, C. M., Nielsen, K., Takahashi, H., Taylor, M. J., Hoppel, K. W., and Eckermann, S. D. (2011). Analysis of gravity waves structures visible in noctilucent cloud images. *J. Atmos. Sol. Terr. Phy.*, 73(14-15), 2082–2090. doi:10.1016/j.jastp.2010.06.001.

Placke, M., Hoffmann, P., Gerding, M., Becker, E., and Rapp, M. (2013). Testing linear gravity wave theory with simultaneous wind and temperature data from the mesosphere. *J. Atmos. Sol. Terr. Phy.*, 93, 57–69. doi:10.1016/j.jastp.2012.11.012.

Plane, J. M. C. (2000). The role of sodium bicarbonate in the nucleation of noctilucent clouds. *Ann. Geophys.*, 18, 807–814.

Plane, J. M. C., Feng, W., and Dawkins, E. C. M. (2015). The Mesosphere and Metals: Chemistry and Changes. *Chem. Rev.*, 115(10), 4497–4541. doi:10.1021/cr500501m.

Pruppacher, H. R. and Klett, J. D. (1997). *Microphysics of clouds and precipitation*. Dordrecht and Boston: Kluwer Academic Publishers, 2 edition.

Rapp, M., Hedin, J., Strelnikova, I., Friedrich, M., Gumbel, J., and Lübken, F.-J. (2005). Observations of positively charged nanoparticles in the nighttime polar mesosphere. *Geophys. Res. Lett.*, 32. doi:10.1029/2005GL024676.

Rapp, M. and Hoppe, U.-P. (2006). A reconsideration of spectral width measurements in PMSE with EISCAT. *Adv. Space Res.*, 38, 2408–2412. doi:10.1016/j.asr.2004.12.029.

Rapp, M., Lübken, F.-J., Müllemann, A., Thomas, G. E., and Jensen, E. J. (2002). Small-scale temperature variations in the vicinity of NLC: Experimental and model results. *J. Geophys. Res.*, 107(D19), 4392. doi:10.1029/2001JD001241.

Rapp, M., Strelnikova, I., Strelnikov, B., Hoffmann, P., Friedrich, M., Gumbel, J., Megner, L., Hoppe, U.-P., Robertson, S., Knappmiller, S., Wolff, M., and Marsh, D. R. (2010). Rocket-borne in situ measurements of meteor smoke: Charging properties and implications for seasonal variation. *J. Geophys. Res.*, 115.

Rapp, M. and Thomas, G. E. (2006). Modeling the microphysics of mesospheric ice particles: Assessment of current capabilities and basic sensitivities. *J. Atmos. Sol. Terr. Phy.*, 68(7), 715–744. doi:10.1016/j.jastp.2005.10.015.

Rapp, M., Thomas, G. E., and Baumgarten, G. (2007). Spectral properties of mesospheric ice clouds: Evidence for nonspherical particles. *J. Geophys. Res.*, 112, D03211. doi:10.1029/2006JD007322.

Reguera, D., Bowles, R. K., Djikaev, Y., and Reiss, H. (2003). Phase transitions in systems small enough to be clusters. *J. Chem. Phys.*, 118(1), 340. doi:10.1063/1.1524192.

Reguera, D. and Rubí, J. M. (2001). Nonequilibrium translational-rotational effects in nucleation. *J. Chem. Phys.*, 115(15), 7100–7106. doi:10.1063/1.1405122.

Reid, G. C. (1990). Ice particles and electron 'bite-outs' at the summer polar mesopause. *J. Geophys. Res.*, 95(D9), 13891–13896. doi:10.1029/JD095iD09p13891.

Reiss, H. and Katz, J. L. (1967). Resolution of the Translation – Rotation Paradox in the Theory of Irreversible Condensation. *J. Chem. Phys.*, 46, 2496 – 2499. doi:10.1063/1.1841074.

Reiss, H., Katz, J. L., and Cohen, E. R. (1968). Translation–Rotation Paradox in the Theory of Nucleation. *J. Chem. Phys.*, 48(12), 5553 – 5560. doi:10.1063/1.1668256.

Robertson, S., Dickson, S., Horányi, M., Sternovsky, Z., Friedrich, M., Janches, D., Megner, L., and Williams, B. (2014). Detection of meteoric smoke particles in the mesosphere by a rocket-borne mass spectrometer. *J. Atmos. Sol. Terr. Phy.*, 118, Part B, 161 – 179. doi:10.1016/j.jastp.2013.07.007.

Roble, R. G. and Dickinson, R. E. (1989). How will changes in carbon dioxide and methane modify the mean structure of the mesosphere and thermosphere? *Geophys. Res. Lett.*, 16(12), 1331–1444.

Roddy, A. F. (1984). The role of meteoric particles in noctilucent clouds. *Irish Astron. J.*, 16, 194 – 202.

Rong, P. P., Yue, J., Russell III, J. M., Lumpe, J. D., Gong, J., Wu, D. L., and Randall, C. E. (2015). Horizontal winds derived from the polar mesospheric cloud images as observed by the CIPS instrument on the AIM satellite. *J. Geophys. Res.*, 120(11), 5564–5584. doi:10.1002/2014JD022813.

Rosinski, J. and Snow, R. H. (1961). Secondary particulate matter from meteor vapors. *J. Meteorol.*, 18(6), 736–745. doi:10.1175/1520-0469(1961)018<0736:SPMFMV>2.0.CO;2.

Russell III, J. M., Rong, P., Bailey, S. M., Hervig, M. E., and Petelina, S. V. (2010). Relationship between the summer mesopause and polar mesospheric cloud heights. *J. Geophys. Res.*, 115, D16209. doi:10.1029/2010JD013852.

Rüster, R. and Reid, I. M. (1990). VHF Radar Observations of the Dynamics of the Summer Polar Mesopause Region. *J. Geophys. Res.*, 95(D7), 10005–10016. doi:10.1029/JD095iD07p10005.

Saunders, R. W., Möhler, O., Schnaiter, M., Benz, S., Wagner, R., Saathoff, H., Connolly, P. J., Burgess, R., Murray, B. J., Gallagher, M., Wills, R., and Plane, J. M. C. (2010). An aerosol chamber investigation of the heterogeneous ice nucleating potential of refractory nanoparticles. *Atmos. Chem. Phys.*, 10(3), 1227–1247.

Saunders, R. W. and Plane, J. M. C. (2006). A laboratory study of meteor smoke analogues: Composition, optical properties and growth kinetics. *J. Atmos. Sol. Terr. Phy.*, 68, 2182–2202.

Schmidt, H., Brasseur, G. P., Charron, M., Manzini, E., Giorgetta, M. A., Diehl, T., Fomichev, V. I., Kinnison, D., Marsh, D., and Walters, S. (2006). The HAMMONIA Chemistry Climate Model: Sensitivity of the Mesopause Region to the 11-Year Solar Cycle and CO 2 Doubling. *J. Climate*, 19(16), 3903–3931. doi:10.1175/jcli3829.1.

Schulte, P. and Arnold, F. (1992). Detection of upper atmospheric negatively charged microclusters by a rocket-borne mass spectrometer. *Geophys. Res. Lett.*, 19(23), 2297–2300. doi:10.1029/92gl02631.

Seele, C. and Hartogh, P. (1999). Water vapor of the polar middle atmosphere: Annual variation and summer mesosphere Conditions as observed by ground–based microwave spectroscopy. *Geophys. Res. Lett.*, 26(11), 1517.

Seki, J. and Hasegawa, H. (1983). The heterogeneous condensation of interstellar ice grains. *Astrophys. Space Sci.*, 94(1), 177–189.

Sigsbee, R. A. (1969). Vapor to condensed-phase heterogeneous nucleation. In A. C. Zettlemoyer (Ed.), *Nucleation* (pp. 151–224). Marcel Dekker.

Simmons, A. J. and Burridge, D. M. (1981). An Energy and Angular-Momentum Conserving Vertical Finite-Difference Scheme and Hybrid Vertical Coordinates. *Mon. Wea. Rev.*, 109(4), 758–766. doi:10.1175/1520-0493(1981)109<0758:AEAAMC>2.0.CO;2.

Siskind, D. E., Stevens, M. H., Hervig, M., Sassi, F., Hoppel, K., Englert, C. R., and Kochenash, A. J. (2011). Consequences of recent Southern Hemisphere winter variability on polar mesospheric clouds. *J. Atmos. Sol. Terr. Phy.*, 73(13), 2013 – 2021. doi:10.1016/j.jastp.2011.06.014.

Slipher, V. M. (1929). Emissions in the spectrum of the light of the nightsky. *Publ. Astron. Soc. Pacific*, 41, 262–265.

Stevens, M. H., Gumbel, J., Englert, C. R., Grossman, K. U., Rapp, M., and Hartogh, P. (2003). Polar mesospheric clouds formed from space shuttle exhaust. *Geophys. Res. Lett.*, 30(10), 1546. doi:10.1029/2003GL017249.

Stevens, M. H., Lossow, S., Fiedler, J., Baumgarten, G., Lübken, F.-J., Hallgren, K., Hartogh, P., Randall, C. E., Lumpe, J., Bailey, S. M., Niciejewski, R., Meier, R. R., Plane, J. M. C., Kochenash, A. J., Murtagh, D. P., and Englert, C. R. (2012). Bright polar mesospheric clouds formed by main engine exhaust from the space shuttle's final launch. *J. Geophys. Res.*, 117(D19). doi:10.1029/2012jd017638.

Stevens, M. H., Meier, R. R., Chu, X., DeLand, M. T., and Plane, J. M. C. (2005). Antarctic mesospheric clouds formed from space shuttle exhaust. *Geophys. Res. Lett.*, 32(13). doi:10.1029/2005GL023054.

Stevens, M. H., Siskind, D. E., Eckermann, S. D., Coy, L., McCormack, J. P., Englert, C. R., Hoppel, K. W., Nielsen, K., Kochenash, A. J., Hervig, M. E., Randall, C. E., Lumpe, J., Bailey, S. M., Rapp, M., and Hoffmann, P. (2010). Tidally induced variations of polar mesospheric cloud altitudes and ice water content using a data assimilation system. *J. Geophys. Res.*, 115(D18). doi:10.1029/2009JD013225.

Stimpfl, M., Walker, A., Drake, M., de Leeuw, N., and Deymier, P. (2006). An ångström-sized window on the origin of water in the inner solar system: Atomistic simulation of adsorption of water on olivine. *J. Cryst. Growth*, 294(1), 83 – 95. doi:10.1016/j.jcrysgro.2006.05.057.

Stober, G., Sommer, S., Rapp, M., and Latteck, R. (2013). Investigation of gravity waves using horizontally resolved radial velocity measurements. *Atmos. Meas. Tech.*, 6, 2893–2905. doi:10.5194/amt-6-2893-2013.

Stølen, S., Glöckner, R., Grønvold, F., Atake, T., and Izumisawa, S. (1996). Heat capacity and thermodynamic properties of nearly stoichiometric wüstite from 13 to 450 k. *Am. Mineral.*, 81, 973–981.

Strelnikova, I. and Rapp, M. (2011). Majority of PMSE spectral widths at UHF and VHF are compatible with a single scattering mechanism. *J. Atmos. Sol. Terr. Phy.*, 73, 2142–2152. doi:10.1016/j.jastp.2010.11.025.

Strelnikova, I., Rapp, M., Raizada, S., and Sulzer, M. (2007). Meteor smoke particle properties derived from Arecibo incoherent scatter radar observations. *Geophys. Res. Lett.*, 34(15). doi:10.1029/2007GL030635.

Thayer, J. P., Rapp, M., Gerrard, A. J., Gudmundsson, E., and Kane, T. J. (2003). Gravity-wave influences on Arctic mesospheric clouds as determined by a Rayleigh lidar at Sondrestrom, Greenland. *J. Geophys. Res.*, 108(D8), 8449. doi:10.1029/2002JD002363.

Thomas, G. E. (1991). Mesospheric clouds and the physics of the mesopause region. *Rev. Geophys.*, 29(4), 553. doi:10.1029/91RG01604.

Thomas, G. E. (1996). Is the polar mesosphere the miner's canary of global change? *Adv. Space Res.*, 18, (3)–149–(3)158.

Thomas, G. E. and McKay, C. P. (1985). On the mean particle size and water content of polar mesospheric clouds. *Planet. Space Sci.*, 33(10), 1209–1224. doi:10.1016/0032-0633(85)90077-7.

Thomas, G. E., Olivero, J. J., DeLand, M., and Shettle, E. P. (2003). Comment on "Are Noctilucent Clouds Truly a 'Miner's Canary' for Global Change?". *Eos, Transactions, American Geophysical Union*, 84(36), 352–353.

Thomas, G. E., Olivero, J. J., Jensen, E. J., Schroeder, W., and Toon, O. B. (1989). Relation between increasing methane and the presence of ice clouds at the mesopause. *Nature*, 338, 490–492.

Tolman, R. C. (1949). The Effect of Droplet Size on Surface Tension. *J. Chem. Phys.*, 17, 333. doi:10.1063/1.1747247.

Toon, O. B., Turco, R. P., Hamill, P., Kiang, C. S., and Whitten, R. C. (1979). A one-dimensional model describing aerosol formation and evolution in the stratosphere: II. Sensitivity studies and comparison with observations. *J. Atmos. Sci.*, 36(4), 718–736. doi:10.1175/1520-0469(1979)036<0718:AODMDA>2.0.CO;2.

Toon, O. B., Turco, R. P., Westphal, D., Malone, R., and Liu, M. (1988). A multidimensional model for aerosols: Description of computational analogs. *J. Atmos. Sci.*, 45(15), 2123–2143. doi:10.1175/1520-0469(1988)045<2123:AMMFAD>2.0.CO;2.

Trainer, M. G., Toon, O. B., and Tolbert, M. A. (2009). Measurements of Depositional Ice Nucleation on Insoluble Substrates at Low Temperatures: Implications for Earth and Mars. *J. Phys. Chem*, 113, 2036 – 2040. doi:10.1021/jp805140p.

Turco, R. P., Hamill, P., Toon, O. B., Whitten, R. C., and Kiang, C. S. (1979). A one-dimensional model describing aerosol formation and evolution in the stratosphere: I. Physical processes and mathematical analogs. *J. Atmos. Sci.*, 36(4), 699–717. doi:10.1175/1520-0469(1979)036<0699:AODMDA>2.0.CO;2.

Turco, R. P., Toon, O. B., Whitten, R. C., Keesee, R. G., and Hollenbach, D. (1982). Noctilucent clouds: Simulation studies of their genesis, properties and global influences. *Planet. Space Sci.*, 30(11), 1147–1181. doi:10.1016/0032-0633(82)90126-X.

Ulwick, J. C., Baker, K. D., Kelley, M. C., Balsley, B. B., and Ecklund, W. L. (1988). Comparison of simultaneous MST radar and electron density probe measurements during STATE. *J. Geophys. Res.*, 93, 6989–7000. doi:10.1029/JD093iD06p06989.

Vehkamäki, H., Määttänen, A., Lauri, A., Napari, I., and Kulmala, M. (2007). Technical Note: The heterogeneous Zeldovich factor. *Atmos. Chem. Phys.*, 7, 309–313. doi:10.5194/acp-7-309-2007.

Volmer, M. (1939). *Kinetik der Phasenbildung*. Verlag Th. Steinkopff, Dresden.

von Savigny, C., Kokhanovsky, A., Bovensmann, H., Eichmann, K.-U., Kaiser, J., Noël, S., Rozanov, A., Skupin, J., and Burrows, J. (2004). NLC detection and particle size determination: first results from SCIAMACHY on ENVISAT. *Adv. Space Res.*, 34(4), 851–856. doi:10.1016/j.asr.2003.05.050.

von Zahn, U. (2003). Are Noctilucent Clouds Truly a "Miner's Canary" for Global Change? *Eos, Transactions, American Geophysical Union*, 84(28), 261–264.

Vonnegut, B. (1947). The Nucleation of Ice Formation by Silver Iodine. *J. Appl. Phys.*, 18(7), 593 – 595. doi:10.1063/1.1697813.

Widdel, H.-U. (1987). Vertical movements in the middle atmosphere derived from foil cloud experiments. *J. Atmos. Terr. Phys.*, 49(7-8), 723–731. doi:10.1016/0021-9169(87)90015-8.

Wilms, H., Rapp, M., and Kirsch, A. (2016). Nucleation of mesospheric ice particles: Sensitivities and limits. *J. Geophys. Res.*, 121, 2621–2644. doi:10.1002/2015JA021764.

Witt, G. (1962). Height, structure and displacements of noctilucent clouds. *Tellus*, 14(1), 1–18. doi:10.1111/j.2153-3490.1962.tb00115.x.

Witt, G. (1968). Optical characteristics of mesospheric aerosol distributions in relation to noctilucent clouds. *Tellus XX*, 20(1), 98 – 114.

Witt, G. (1969). The Nature of Noctilucent Clouds. *Space Research*, 9, 157–169.

Wood, S. E. (1999). *Nucleation and growth of CO2 ice crystals in the Martian atmosphere*. PhD thesis, Dept. of Earth and Space Sciences, University of California, Los Angeles.

Acknowledgments

First of all, I want to thank Markus Rapp for his supervision in all aspects of this work, for his good ideas and support, giving me the freedom to pursue my own ideas but also bringing me back on track when I got lost in unnecessary details. I am grateful for the opportunities to visit international workshops and conferences during the time of my PhD and for his initiative to combine modeling studies with lab experiments in this project.

This research would not have been as exciting if it hadn't been for Denis Duft, Mario Nachbar and Thomas Leisner at the KIT. Thank you for regularly inviting me so that I could experience first hand how the lab experiments are proceeding. Thank you for patiently listening to all my ideas, no matter how unusual they were, and trying to implement them. The many discussions with Denis about nucleation theory were extremely helpful - each of them brought me a great step forward, and made me realize that nature is much more complicated than classical nucleation theory assumes.

Many thanks to my dear colleagues and co-authors Heiner Asmus and Annekatrin Kirsch. I really enjoyed working with both of you.

Special thanks go to the 'Middle Atmosphere Group' (Bernd, Natalie, Andreas, Carsten, Benedikt, Sonja, Martina, Hella, Johannes, Tanja, Mareike) for all the discussions, good questions and that in your world the atmosphere doesn't end at 20 km altitude.

I received valuable support from Bernd Kärcher, who familiarized me with the basic concepts of the nucleation theory and whom I want to thank very much.

Furthermore, I want to thank my colleagues at IPA for the good working atmosphere and all the chat and cake at various occasions. Special thanks go to department 1, who supported me in all aspects regarding modeling.

I owe a big thank to my office mates Vanessa, Mariano and Matthias - I had a great time sharing the office with you. Thanks for all your support and helping me to think through some arguments. Thanks for all the discussions, fun, and chili sharing.

Last, but not least, I want to thank my friends and family for their continuous support and motivation.